# The environmentally assisted cracking of Ru enriched laser alloyed surface layers on 304L stainless steel

Nick Nonofo Tshilwane

A dissertation submitted to the Faculty of Engineering, University of the Witwatersrand, Johannesburg, in fulfilment of the requirements for the degree of Master of Science in Engineering

Johannesburg,   2018

DECLARATION

I declare that this dissertation is my own unaided work. It is being submitted for the Degree of Master of Science in Engineering in the University of the Witwatersrand, Johannesburg. It has not been submitted before for any degree or examination in any other University.
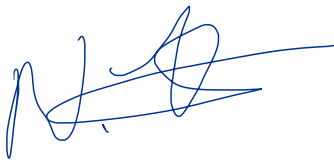
_____
Signature

24ᵗʰ day of _May____ 2018

ABSTRACT

The use of austenitic stainless steels in harsh environments at elevated temperatures has increasingly become a global problem, these alloys can fail unpredictably when subjected to tensile stresses and chlorides. Hence the study was focused on understanding the environmentally assisted cracking of Ru enriched laser alloyed layers on 304L stainless steel in a corrosive environment at elevated temperatures. The Ru composition of laser alloyed samples was 0, 0.96, 1.96, 4.74 and 9.2 wt%.

Microstructural analysis and microhardness measurements were performed in order to understand the grain orientation and resistance to indentation respectively. The bend beam SCC test was conducted by stressing the samples to 350 MPa and exposing them to 50 ppm sodium chloride with 10 ppm dissolved oxygen at 160°C for 172 hours. The results revealed a significant improvement in the SCC resistance. The samples with lower Ru content (0, 0.98 and 1.96 wt%) were less susceptible to SCC when compared to as-received 304L stainless steel. Cracks initiated from pits and propagated transgranularly on the alloyed layer. The crack growth rate decreased as the Ru content was increased. The samples with 4.74 and 9.2 wt% Ru were immune to SCC. Electrochemical test results showed improved corrosion resistance when the Ru level was increased to 1.96 wt%. Thereafter, there was a gradual increase in corrosion rates for samples with 4.74 and 9.2 wt% Ru. However, these corrosion rates were lower when compared to as-received 304L stainless steel. Another SCC test was conducted to investigate fractography of vacuum remelted samples alloyed with Ru. The results showed ductile failure for most of the samples and the maximum stress threshold of 580 MPa was archived on samples with 1.07 wt% Ru. There was a sudden increase in failure time, % elongation and % reduction in area when the Ru content was increased to 1.07 wt%.

In essence, laser surface alloying 304L stainless steel with higher Ru content (more than 2wt%) improves SCC resistance, but does not improve the general corrosion resistance, therefore a careful selection for any application is necessary. However, the cost analysis revealed the laser surface alloying of 304L stainless steel with Ru to be more efficient over other corrosion resistant materials.

DEDICATION

To

my parents Mr Moikgatlo Tshilwane and Mrs Nyatsego Tshilwane

"I'm so grateful to have you in my life, you are my hero and you'll always be"

ACKNOWLEDGEMENTS

TABLE OF CONTENTS

LIST OF FIGURES

LIST OF TABLES

NOMENCLUTURE

List of symbols

Ag	silver
AgCl	silver chloride
C	carbon
Cl^-	chloride ions
Cr	chromium
Cu	copper
E_{corr}	corrosion potential
Fe	iron
Mn	manganese
Mg	magnesium
Mo	molybdenum
NaCl	sodium chloride
Na_2RuO_4	sodium ruthenate
Nb	niobium
Ni	nickel
P	phosphorus
Pt	platinum
Ru	ruthenium
RuO_2	ruthenium oxide
Si	silicon
S	sulphur
Ti	titanium
V	vanadium
WC-Co	tungsten
$(NH_4)_3RuCl_6$	ammonium hexachlororuthenate (III)

Abbreviations

AR	as-received
ASTM	American Society for Testing and Materials
AZ	alloyed zone
CSIR	Council of Scientific and Industrial Research
DAQ	Data acquisition
DO	dissolved oxygen
EAC	environmentally assisted cracking
EBSD	Electron back scatter diffraction
EDS	energy dispersive x-ray spectroscopy
EIS	electrochemical impedance spectroscopy
FEA	finite element analysis
HAZ	heat affected zone
IGSCC	Intergranular stress corrosion cracking
LAZ	laser alloyed zone
LSA	laser surface alloying
OCP	open circuit potential
Nd: YAG	neodymium yttrium aluminium garnet
NI	National instruments
SCC	stress corrosion cracking
SS	stainless steel
SEM	scanning electron microscope
SSRT	slow strain rate testing
TGSCC	Transgranular stress corrosion cracking
VAR	vacuum arc remelting
XRD	X-ray diffraction
XRF	X-ray fluorescence

CHAPTER 1

INTRODUCTION

1.1 Overview

The world today depends heavily on engineering infrastructure and energy industries, but this can be compromised due to harsh corrosive environments. As observed in the 20th century (Lynch, 1988; Beachem, 1972; Copson, 1956), environmentally assisted cracking (EAC) such as stress corrosion cracking (SCC) is often unpredicted and can be catastrophic. The presence of specific aggressive environments will cause the metal under loading to exhibit poor mechanical behaviour and eventually lead to structural failure. This can lead to exorbitant repair costs and most importantly be threatening to loss of life.

Stainless steels are used in many industries because of excellent corrosion resistance. The on-going demands for increased production in various industries result in exposing 304L stainless steel products such as pipes, vessels, and reactors to harsh environments that might not have been anticipated initially during the design phase, and consequently leading to failure. This prompted engineers, researchers and scientists to direct research in understanding SCC and the development of new alloys that are more resistant to SCC. The common practice used to control SCC is to alter at least one of three main factors, namely; the environment, tensile stress and the present susceptible material. The environment will interact with the metal under loading and cause a crack to propagate. The concept of solution specificity remains valid in the sense that some media will promote cracking while others do not. For instance, type 304L stainless steel is more susceptible to SCC in chloride environments than in distilled water. SCC of stainless steels continues to be a significant form of failure. Therefore, alloying metals with highly corrosion resistant elements such Ni and Ru can assist to mitigate SCC (Scenini et al., 2012).

According to the Copson curve, stainless steels with 10 wt% Ni will be more susceptible to SCC hence Ni content should be kept below this value to reduce SCC time to failure (Copson, 1989). Leet and Uhkig (1970) reported that the addition of 45 wt% Ni increased the SCC resistance of stainless steels in chloride containing environment. However, this approach is costly and often not practised by some steel industries. It has been reported that

the use of Ru as an alloying element can be beneficial in improving corrosion resistance of stainless steels. Govender et al. (2012) found that 304 stainless steel with Ru additions was less susceptible to SCC than palladium modified alloys. Liang et al. (2010) reported the weld consumable of Ni-Cu-Ru to exhibit good corrosion resistance on 304L stainless steels. Other studies (Van Der Merwe and Tharandt, 2015; Potgieter and Brookes, 1995) revealed that additions of Ru on stainless steel surface improved hardness and corrosion behaviour.

Although there has been an enormous amount of work on SCC of stainless steels, very little has been done on alloys with Ru. Scenini et al. (2012) reported that 304 stainless steel alloyed with Ru exhibited better SCC resistance but it was not clear on their findings how the crack initiated and what happens at the crack tip. Similarly, Yeh et al. (2013) did not discuss the possible mechanism of SCC in depth. However, the study conducted here will investigate the susceptibility of Ru enriched laser surface alloyed layers on 304L stainless steel to SCC. The initiation and propagation of SCC cracks will be analysed. A proposed SCC mechanism, as well as electrochemical behaviour of laser alloyed samples will be discussed. Furthermore, the SCC effect of alloying 304L stainless steels with Ru by using the vacuum arc remelting technique will be discussed.

1.2 Background and motivation

Austenitic stainless steels have proved to be corrosion resistant in various applications. However, these alloys will corrode when exposed to specific environments most notably in those containing chlorides at elevated temperatures. In 2009, the high pressure vessel of crystal manufacturing company failed due to SCC (Cohen, 2013). Another incident occurred in Flexborough, UK where a pipe carrying cyclohexane exploded, the pipe was installed temporarily to isolate the leaking reactor. The presence of nitrates and residual stresses initiated a crack in the outer layer of the leaking reactor (Kingston, 2013). In another case, a huge Canadian natural gas pipeline ruptured due to the pre-existing stress corrosion cracks (Mandel, 2015). The pipeline failed unexpectedly despite the installed corrosion monitoring systems. In South Africa, the Koeberg nuclear power station is due to replace its steam generators which showed early stages of SCC on steam pipelines (Lewis, 2015). The canisters made of type 304L stainless steel at nuclear power plants are exposed to coastal environments where airborne salts could accumulate on the surface of a vessel and lead to SCC (Mintz, 2013). SCC failures are often attributed to the growth of pre-existing crack-like

flaws, and the difficulty of controlling this phenomenon lies in altering environmental conditions. Hence it is essential to improve the corrosion resistance of metals under loading, especially stainless steel. The following research questions were used as a guide to investigate the SCC:

Research questions:

- What is the basic mechanism by which the environment causes the crack to propagate?
- How does the corrosive environment, microstructure and tensile stresses influence the SCC of laser alloyed 304L stainless steel with Ru?
- What is the effect of alloying 304L stainless steel with corrosion resistance elements such as Ni and Ru, particularly on SCC resistance?

1.3 Hypothesis

Despite the vast amount of work conducted on SCC by previous researchers (Yeh et al., 2013; Scenini et al., 2012; Govender et al., 2012; Lynch, 1988; Beachem, 1972). This study will provide an insight into understanding the SCC behaviour of Ru alloyed and vacuum remelted stainless steels in chloride solutions containing oxygen. The hypothesis is that Ru laser alloyed samples will improve SCC resistance without compromising the mechanical properties, improving the hardness.

1.4 Objectives

The aim of this study was to understand the SCC susceptibility of Ru laser alloyed 304L stainless steel at elevated temperatures in an aqueous environment. The principal objectives were to:

- Analyse the microstructure and microhardness of Ru alloyed surface layers on 304L stainless steel as well as the Ru distribution in the welded zone.
- Investigate the crack morphology and the influence of Ru on the SCC of 304L stainless steel.

- Compare the cracking resistance of laser cladded 304L samples with as-received 304L stainless steel. Determine the maximum stress threshold at which Ru alloyed 304L stainless steel will experience SCC failure in a sodium chloride solution at elevated temperatures.
- Determine the electrochemical characteristics of type 304L stainless steel alloyed with Ru.

1.5 Research outline

EAC is a phenomenon which can occur without warning and can be catastrophic. It is for this reason that the study here is aimed at investigating the use of Ru as an alloying element on 304L stainless steel to mitigate the problem. The work is divided into sections (chapters), where chapter 2 describes the work done related to this topic. In chapter 3, the experimental procedure for achieving the primary tests is explained. The results and discussion chapters gives an in-depth explanation on the effect of Ru on the microstructure, hardness, SCC and electrochemical behaviour.

Moreover, there was additional work performed during the course on this research. The author published and presented his work at conferences and seminars. A summary of the work performed is as follows:

(i) N.N. Tshilwane and J.W. van der Merwe. *Stress corrosion cracking of laser alloyed 304L stainless steel with Ru in hot chloride solution*. Journal of Surface and Coatings Technology. (See appendix A).

(ii) N.N. Tshilwane and J.W. van der Merwe. *Understanding SCC of Ru laser alloyed 304L stainless steels in an oxygenated chloride solution*. Proceedings of the Microscopy Society of Southern Africa (MSSA) Conference, Bella-Bella. 4th - 7th December, 2017.

(iii) N.N. Tshilwane and J.W. van der Merwe. *Fractography of vacuum remelted 304L stainless steel with Ru in chloride environment containing dissolved oxygen*. Poster Presentation. 8th Cross-Faculty Postgraduate Symposium, Education Campus, University of the Witwatersrand, Johannesburg. 25th - 26th October 2017.

(iv) N.N Tshilwane and J.W. van der Merwe. *Effect of Ru on the environmentally assisted cracking of 304L stainless steel in hot chloride solution.* Research presentation. School of Chemical and Metallurgical Engineering, University of the Witwatersrand, Johannesburg. 30th August 2017.

(v) N.N Tshilwane and J.W van der Merwe. *Stress corrosion cracking of Ru enriched laser alloyed surface layer on 304L stainless steel.* Poster presentation. DST-NRF Centre of Excellence in Strong Materials, University of the Witwatersrand, Johannesburg. 17th May 2017.

(vi) N.N Tshilwane and J.W. van der Merwe. *Stress corrosion cracking of 304L stainless steel in various environments.* Proceedings of the AFRICORR Congress, Midrand. 25th - 29th July 2016.

(vii) N.N Tshilwane and J.W. van der Merwe. *SCC of Ru alloyed LDX2101 duplex stainless steel in NaCl solution.* Poster presentation. DST-NRF Centre of Excellence in Strong Materials, University of the Witwatersrand, Johannesburg. 26th May 2016.

CHAPTER 2

LITERATURE REVIEW

2.1 Stainless steels

In 1913, Harry Brearley discovered one of the prestigious corrosion resistant metals used in many industries today. While working on steel which has more wear resistance Brearley found that casting of steel with 12.8 wt% Cr, 0.24 wt% C, 0.44 wt% Mg and 0.20 wt% Si strongly resisted chemical attack (Cobb, 2010); this alloy became well known as stainless steel worldwide. Stainless steels were further characterised by a thin oxide film which prevents chemical attack.

2.1.1 Types of stainless steels

Typical stainless steels can be categorised into five different groups, namely: austenitic, ferritic, martensitic, duplex and precipitation hardening.

2.1.1.1 Austenitic stainless steels

Austenitic stainless steels are the largest produced and consumed group of stainless steels. They exhibit considerably better corrosion resistance than martensitic or ferritic stainless steels and show acceptable oxidation resistance at elevated temperatures (Sedriks, 1979). These steels are classified depending on compositional modifications to improve corrosion resistance, high temperature oxidation resistance and strength. The three main groups are Cr-Ni (300 series), Mn-Cr-Ni-N (200 series) and specialty alloys (Brinkman and Gavin, 1979). Type 304 stainless steel belong to Cr-Ni group and consists of 0.08 wt% C, 0.03 wt% S, 0.045 wt% P, 0.1 wt% N, 0.75 wt% Si, 2 wt% Mn, 18 wt% Cr, 8 wt% Ni and 71 wt% Fe (Outokumbu, 2015). Type 304 is well known for its corrosion resistance and ease of machining into any shape of interest. They are available in rolls or sheets for different industrial applications. The Cr and Ni contents give the type 304 stainless steel resistance to corrosion and the L-grade with low carbon content improves weldability (Nielsen, 2006). Type 304L has an advantage over 304 on stress corrosion resistance at high temperatures, the low carbon content help reduce the carbide precipitation which usually occurs at the

grain boundaries of the heat affected zone closer to the weld. This type of steel can be stress relieved at temperatures between 1050 and 1120°C (BSSA, 2017). Other elements such as titanium and carbon may be added to 304L to prevent it from intergranular corrosion. Type 304L has a face-centered cubic (FCC) crystal structure. It has yield and tensile strength of 241 MPa and 586 MPa respectively (AK Steel, 2015).

Austenitic stainless steels such as type 304, 304L, 316 and 308L are commonly used in manufacturing and petrochemical industries. The application of these alloys in nuclear power plants has increased over years, finding its use in most critical components of the plant such as pipelines which transport water and steam. However, previous studies (Raman and Siew, 2014; Prosek et al., 2014; Juang and Altstetter, 2012; Basson and Wicker, 2002; Speidel, 1981) have reported these alloys to suffer from SCC when exposed to chloride containing environments.

2.1.1.2 Ferritic stainless steels

Ferritic stainless steels have high levels of chromium which promotes body centred cubic (BCC) crystal structure. They are generally classified as the 400 series and consist of Cr, Ni, Mn, Si, S, C, P, Mo, N and Nb (Klar and Samal, 2007). Unlike austenitic stainless steels, ferritic stainless steels are less corrosion resistant and their strength is lower at elevated temperatures. They suffer from high temperature embrittlement which could lead to severe intergranular corrosion cracking (Tabolt and Tabolt, 1998). Ferritic stainless steels are ductile and formable but can perform poorly when subjected to high temperatures. Lowering the carbon content to 0.03 wt% does not prevent corrosion attack as it does in austenitic stainless steels (Sedriks, 1979). Ferritic stainless steels are mostly used in low temperature appliances such as kitchen counters and sinks. They also have good thermal conductivity which makes them best suitable to heat transfer appliances. To their disadvantage they cannot be hardened by heat treatment.

2.1.1.3 Duplex stainless steels

The microstructure of duplex stainless steels consists of a dual phase structure with both austenite and ferrite. As defined by Schaeffler diagram (Tabolt and Tabolt, 1998) , duplex

stainless steel contains 28 wt% Cr and 6 wt% Ni to produce structures with equal proportions of austenite and ferrite. Duplex stainless steels are more resistant to SCC than austenitic stainless steels, the cracks advancing through austenite encounter a more resistant ferrite (Bhattacharya, 2008). The presence of Cr, Ni and Mo in these alloys help improve the corrosion resistant than 304L austenitic stainless steel. Type 2205 and 2507 duplex stainless steels are the commonly used alloys because of their good resistance to pitting and SCC. These alloys have tensile strength ranging from 650 to 800 MPa. Typical applications of duplex stainless steels are structural components in bridges, flanges, valves, tubes and pipes in oil and gas, pulp and paper industries.

2.1.1.4 Martensitic stainless steels

Martensitic grades are the Fe-Cr stainless steels which consists 11.5-18 wt% Cr. They exhibit high strength and wear resistance. The higher carbon (0.15-1.2 wt%) content of this grade allows then to harden in air and oil during cooling (Outokumbu, 2015). Martensitic stainless steels has a body centred tetragonal (BCT) crystal structure and they can be machined and cold formed in the annealed condition. The addition of Ni to martensitic grade plays a significant role as it gives a good resistance to localised corrosion in corrosive environments such as sulphuric acids (Truman, 1981). Typical applications include press plates, cutlery, pump parts, ball bearings, surgical and dental instruments.

2.1.1.5 Precipitation hardening grades

Precipitation hardening stainless steels are special alloys with Cr-Ni containing additions such as Al, Cu and Ti that allow them to be hardened by the solution and heat treatment (Cunat, 2004). These alloys are formulated in order to assure strength and hardness as well as corrosion resistance. The hardening can also be obtained by other elements such as Nb and Mo. Precipitation hardening grades are the most expensive type of stainless steel and they are difficult to weld and form. They have high strength and better toughness than austenitic stainless steels. Common uses are in less aggressive environments and lower temperatures, such in aircraft parts, pressure vessels, chains, pumps, shafts, valves and gears knives and scalpels.

2.1.2 Effect of alloying elements

In general, the alloying elements of stainless steels are: Cr, Ni, Mo, Cu, Mg, Si, C, N, Ti and V. More than one element can be added to improve corrosion resistance, formability, machinability and wear resistance. The commonly used alloying elements for austenitic stainless steels are described as follows:

2.1.2.1 Nickel

Nickel was first discovered in 1751 by Axel Fredrick (Cunat, 2004). The element does not play a major role in the passivation of austenitic stainless steel, but has beneficial effects in sulphuric acid environments. Nickel increases mechanical properties such as ductility, toughness and hardness. It is also used in martensitic stainless steels to improve weldability. At elevated temperatures nickel can develop oxide and precipitation hardening phases which are essential for high temperature alloys (Tabolt and Tabolt, 1998). The other benefit of Ni as an alloying element is that it does not form carbides. Nickel is primarily good for mechanical properties than corrosion resistance, it stabilises the ductile austenitic phase. According to Copson's curve (Figure 2.1), the alloys with higher Ni content are not susceptible to cracking.
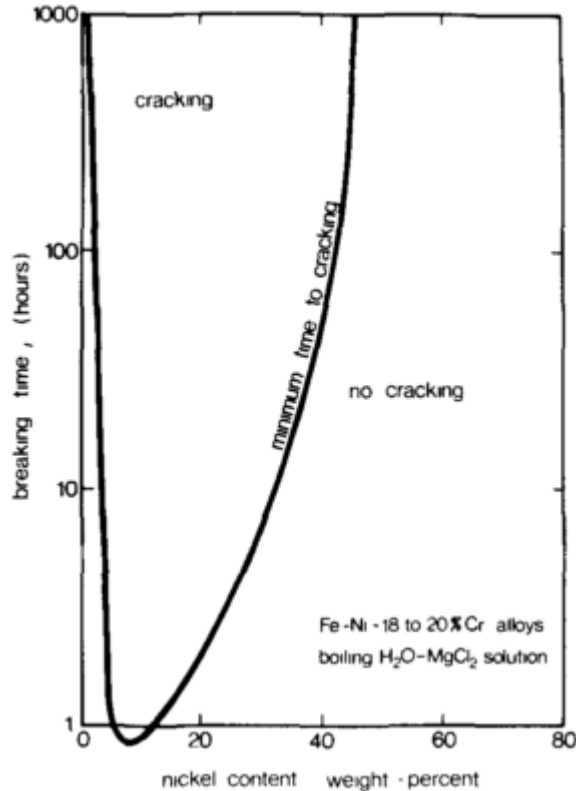
Figure 2.1: Copson's curve showing the effect of Ni on the SCC susceptibility stainless steels in boiling 45% magnesium chloride solution (Speidel, 1981).

The tests showed no cracking after the samples were exposed to 45% magnesium chloride for 30 days (Lancaster, 1980). Moreover, the alloys with lower Ni content (approximately less than 5%) or free from Ni were also immune to SCC. According to Copson's curve, type 304L stainless steel averaging to 10 wt% Ni is among the most susceptible alloys to cracking (Kaneko, 2007). Increasing the Ni content can be costly therefore a practical approach is to use low Ni with chromium content ranging from 18 to 22 wt%. This can vary from steel producers depending on the application of which the alloy is designed for.

2.1.2.2 Chromium

Stainless steels are corrosion resistant and forms a passivation layer because of chromium added to these alloys. Chromium is a silver grey transition metal which becomes shiny mirror-like when polished. It has a BCC crystal structure. The addition of more than 14 wt% of chromium to stainless steel will improve corrosion and staining resistance. Chromium can also be added to stainless steel to improve hardness, wear and shiny appearance to meet the

desired application. The disadvantage of using chromium is that is brittle hence it has to be used with other alloying elements such as Ni (Cunat, 2004).

2.1.2.3 Molybdenum

The reason for adding molybdenum to stainless steel is to improve resistance to pitting corrosion in chloride environments. Molybdenum is added to reduce temper embrittlement and enhance creep resistance of low alloy steels at elevated temperatures. It is added to stainless steels to promote a ferritic microstructure, increase high temperature strength and creep resistance. Molybdenum is normally added in small quantities less than 8 wt% to meet the desired mechanical properties. It has a BCC crystal structure and is a ferrite former.

2.1.2.4 Manganese

Austenitic stainless steels are made by adding higher content of manganese. This is used to enhance hardenability and reduce the brittleness by forming manganese sulphide (Bramfitt and Benscoter, 2002). The 200 series austenitic stainless steels are alloyed with manganese to stabilise the austenite. Moreover, manganese has the ability to deoxidise steel and prevent the iron sulphate from forming. Although large amount of manganese can be added to stainless steels, Degerbeck and Wold (2004) reported that reducing content manganese to 0.2 wt% for 18Cr-9Ni stainless improved the corrosion resistance without compromising weldability. It was further proved that the ferrite was not present and this was in contrast to Schaeffler diagrams.

2.1.2.5 Copper

Copper is used as an alloying element to improve corrosion resistance in specific acids such as sulphuric acid. Most of the common stainless steels such as 304L, 304, 316L and 316 have a copper content in the range of 0.4-0.5 wt% (John, 2014). Copper is added to decrease precipitation hardening and improve formability. It is also used to improve atmospheric corrosion resistance (Schweitzer, 2013).

2.1.2.6 Silicon

This element is mainly used as a deoxidiser in the steel making process. Generally it is used for applications which require electrical and magnetic properties such as transformers. Silicon is an alloying element for both ferrous and non-ferrous metals. It acts as a ferrite stabilizer and it can be added with other elements to improve corrosion resistance and toughness steels. The higher silicon content (greater that 2 wt%) in type 304L stainless steel will improve the corrosion resistance.

2.1.2.7 Carbon

The carbon content in type 304L stainless steels is usually 0.005 to 0.03 wt%. It can defuse rapidly through the structure and concentrate on the grain boundaries (Tverberg, 2003). However, corrosion resistance can be impaired by the formation of chromium carbide which depletes the grain boundaries and promote intergranular corrosion. The formation of chromium carbide can be prevented or reduced by the use of stabilized stainless steels which contain Ti or Nb. Low carbon content will increase corrosion resistance whereas an increase in carbon content will result in high tensile strength and hardness, but ductility will be reduced. Hence a greater balance of carbon and other elements is important. According to Wang et al. (2013) carbon promoted intergranular SCC propagation rate.

2.1.2.8 Ruthenium

Ruthenium (Ru) is part of the Platinum Group Metals (PGMs): iridium, osmium, palladium, platinum, rhodium and ruthenium. Ru is the least expensive of the PGMs and it is produced mostly in South Africa, then China and followed by Russia (Gilchrist, 1943). The PGMs are the rarest and there are extracted from by-product of nickel and platinum ore refining. Following the traditional solvent extraction process, the oxidation of bisulphate produce an insoluble residue containing Ru which is further stabilised as Na_2RuO_4 by fusion method (Cotton, 1997). The reduced RuO_2 is converted into $(NH_4)_3RuCl_6$ which is then reduced with hydrogen at 100ºC to form Ru powder (Gilchrist, 1943). It is this powder that is used for different applications. For example, it is mostly used in electronics industries because of the resistance to tarnish by oxidation or sulfication and has resistance to spark erosion and high melting temperatures of 2310ºC (James and McBreen, 1954). It is not oxidised by air at

room temperature and readily reacts on heating to give RuO_2, but is insoluble in hot or cold mineral acids (Seddon, 1984). Other than Ru being used in electrical appliances such as voltage regulators and thermostats, it is also used as hardening alloy. Previous works (Tjong et al., 1996; Kwok, 2010; Lekala et al., 2012) has shown improved hardness when Ru was added.

The other benefit of Ru is by using it as an alloying ingredient to improve corrosion resistance of alloys. Potgieter et al. (2014) found that small addition of Ru on austenitic 304 stainless steel improved corrosion resistance as compared to as-received in acetic acid. Van der Merwe and Tharandt (2015) observed different corrosion behaviour on Ru laser cladded 304L stainless steel and it was found that higher Ru content did not improve the corrosion resistance. The other study conducted by Liang et al. (2010) reported improved corrosion resistance of welded 304L stainless steel with Ni-Cu-Ru consumables (Ru content was less than 1wt%). It is evident from the previous studies (Van der Merwe and Tharandt, 2015; J H Potgieter et al., 2014; D Liang et al., 2010) that the addition of Ru depend on the content and the corrosion media to improve corrosion resistance. The addition of 1 wt% Ru on 304L stainless steel improved SCC resistance in oxygenated high purity water (Govender et al., 2012).

2.2 Environmentally assisted cracking

Generally, environmentally assisted cracking (EAC) is defined as the form of corrosion which occurs when the material cracks and fails due to tensile stresses when exposed to certain corrosive environments. The major types of EAC are stress corrosion cracking (SCC), corrosion fatigue cracking (CFC), hydrogen embrittlement (HE), and liquid metal embrittlement (LME). The present study will primarily focus on SCC.

2.2.1   Stress corrosion cracking

Stress corrosion cracking occurs when a metallic material is exposed to a corrosive environment under stresses. The main factors which constitute SCC are a susceptible material, applied stresses and a corrosive environment. Eliminating one of these factors will result in eliminating SCC. The problem associated with SCC can be catastrophic when a crack will grow without detection and lead to failure. In general, SCC crack morphology

usually occurs in three-stages; firstly the breakdown of the surface film followed by the initiation of microcracks, and eventually propagation which results in failure. SCC mechanisms at the crack tip are often attributed to one or more processes. The cracks start to propagate as a result of absorption of environmental species, surface film reactions at the surface and in the metal ahead of crack tip.

Moreover, numerous studies have been reported that applied stresses play a detrimental role in promoting SCC. Two forms in which stresses can be introduced is internally through residual stresses or mechanically by the application of a force (tensile). Stresses induce plastic deformation at the crack tip which enhances localised electrochemical processes. It also provides a local concentration of elastic energy which enables a crack to propagate in a brittle manner (Mudali and Pujar, 2002). As shown in Figure 2.2 and Figure 2.3, the cracks can propagate in a transgranular or intergranular manner when stresses are applied to an alloy in a corrosive environment.
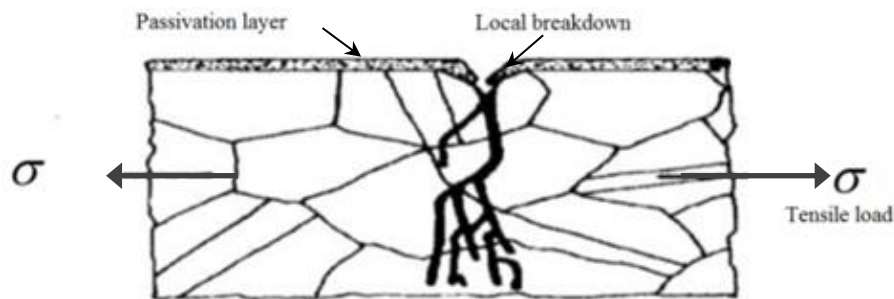
Figure 2.2: Schematic representation of transgranular stress corrosion cracking (Hilti, 2014).
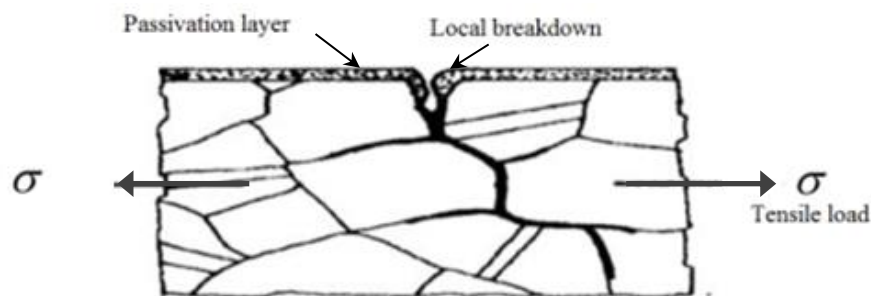
Figure 2.3: Schematic representation of intergranular stress corrosion cracking (Hilti, 2014).

The SCC cracks which grow through the grains as shown in Figure 2.2 will continue to propagate if the propagation rate is sufficient to maintain the crack tip strain rate above the minimum rate for cracking. This mode of cracking can be switched to intergranular stress

corrosion cracking (IGSCC) for sensitised steels (Nishimura, 2007). IGSCC usually occurs when there is a local breakdown of the passivation layer along the grain boundaries and the crack propagates more or less at right angle to tensile stresses. The crack sides re-passivate and the material at the crack tip is attacked by the corrosive solution.

Various works (Yeh et al., 2013; Gangloff, 2003; Lynch, 1989) have been conducted to investigate the crack tip mechanisms and process damage zone. It was found that SCC mechanisms are classified into two groups, the dissolution and cleavage based. The dissolution mechanism simply occurs when there is active dissolution due to corrosion that initiates a crack and cause growth in the process. It is categorised by three models: the pre-existing active path, the strain generated active path and corrosion tunnel. On the other hand, the cleavage mechanism corrosion leads to embrittlement, hydrogen evolution, absorption and diffusion which initiate a crack. This mechanism is categorised by film induced cleavage, turnish rupture and atomic surface mobility.

(i)   **Pre-existing active path:** The active path along the grain boundaries already exists in metals. This path can initiate an SCC crack. In the study conducted by (Bruemmer and Thomas, 2008), it was found that the crack initiated and propagated along the grain boundaries at different crack tip modes. The selective dissolution of Cr at the crack tip produces an unstable corrosion interface. In sensitised austenitic stainless steel there is Cr precipitation along the grain boundaries, which lead to a Cr depleted zone resulting in an active path for dissolution. Nishimura (2007) observed that an increase in sensitisation changes the mode of SCC fracture from transgranular to intergranular.

(ii) **Strain generated active path:** This mechanism occurs either by film rupture through slip step dissolution. Film rupture is a continuous process that involves the rupture of the passive film due to applied stresses. The material will repassivate and the stress will rupture the passive film; this process is repeated until final fracture occurs. The crack varies due to the rate of dissolution and the rate of repassivation. If the rate of dissolution is greater than the rate of repassivation, the crack will propagate faster. The propagation rate can be reduced by the addition of Ni in stainless steels. An increase in Ni content will enhance the stacking fault energy, which in turn promotes cross-slip and makes the slip process less planar. Moreover, Ni can reduce the stress concentration at the tip of blocked slip bands and mitigate the possibility of the rupture

model. The slip step dissolution model is often observed on planes intersecting crack fronts(Van Gelder et al., 1987).

(iii) **Absorption induced cleavage:** This mechanism is associated with hydrogen embrittlement where hydrogen atoms diffuse to the crack tip and embrittle the metal. It is the chemical species that absorb onto the crack surface and reduce fracture stress. It is unlikely for different mechanisms to produce the same crystallographic fracture plane. The dimple tear ridges and slip lines are usually observed on the fractured surface (Lynch, 1989).

(iv) **Film induced cleavage:** The film is formed at the crack tip and the crack propagates into metal where it is arrested by the grains. This can cause the crack arrest marks which are cleavage like and discontinuous. During corrosion, a brittle film is formed and ruptures, leading to the repassivation and formation of the protective layer; and the arrest mark is observed, this process occur repetitively (Barnes et al., 2008).

2.2.2 Liquid metal embrittlement

Liquid metal embrittlement (LME) is a phenomenon which brings a challenge when a liquid metal comes into contact with solid metal either during galvanising, brazing or heat exchanging operations. LME can occur in the presence of tensile stresses, pre-existing crack or some measure of plastic deformation (Westwood, 1970). The presence of a stable obstacle to dislocation motion in the lattice such as grain boundary or precipitate particle can also contribute to LME. Malkin et al. (2008) concluded that LME on superplastic alloys occurred at plastic deformation when the temperature was increased to 183°C. The initiation of a crack due to this phenomenon is still unclear. Westwood (1970) reported a double layer mechanism for complex ion embrittlement where the crack initiated due to the hardened surface. The crack was arrested as it enters softer space charge region. Alyousif and Nishimura (2006) observed intergranular SCC on 304 stainless steel in NaCl at temperature below 140°C which was attributed to the formation of martensite at grain boundaries.

2.2.3 Environmental effects of EAC

Environmental effects such as chloride ions concentration play a role in promoting EAC. As shown in Table 2.1, different alloys will be susceptible to EAC in specific environments.

Table 2.1: EAC environments for various alloys (Safiuddin and Ahammad, 2016; Fontana, 2005; Lancaster, 1980).

ALLOY	ENVIRONMENT
Aluminium alloys	Sea water, moist air, nitric acid, water vapour, mercury, oils and alcohol.
Austenitic stainless steels	Hot chloride solutions, acid chloride solutions, (e.g $MgCl_2$, $BaCl_2$), contaminated steam, hydrogen sulphite, sulphurous and polythionic acids.
Carbon steels	Hot nitrate, hydroxide and carbonate solutions, caustic, CO/CO2 solutions and anhydrous ammonia.
Copper alloys	Amines, mercury, ammoniacal solutions, ammonia vapour and water vapour.
High-strength steels	H_2S solutions, sea water.
Magnesium alloys	Dilute salt, aqueous chloride solutions, nitrite acid, hydrofluoric solutions and costal atmospheres.
Nickel alloys	Hot caustic soda, fluoride or hydrogen sulphide, high purity steam and hydrofluoric acid.
Titanium alloys	Sea water, fused salt, red fuming nitrate solution, dilute hydrochloric acid or sulphuric acid and methanol.
Zirconium alloys	Aqueous halide solutions, hot salts and organic liquids with halide.

Stainless steels are susceptible to media containing sulphides, hydrides and chlorides. The major environmental factors which contribute to EAC of austenitic stainless steel are: chloride ions concentration, hydrogen absorption, dissolved oxygen and temperature (Kowaka and Yamanaka, 1981).

2.2.3.1 Chloride ions concentration

The presence of chloride ions in aqueous solutions promotes SCC of austenitic stainless steels. An increase in chloride concentration will require shorter times to initiate SCC cracks (Nishimura and Maeda, 2004). It is evident that the alloys shown in Figure 2.4 will crack at higher chloride concentrations and temperatures.
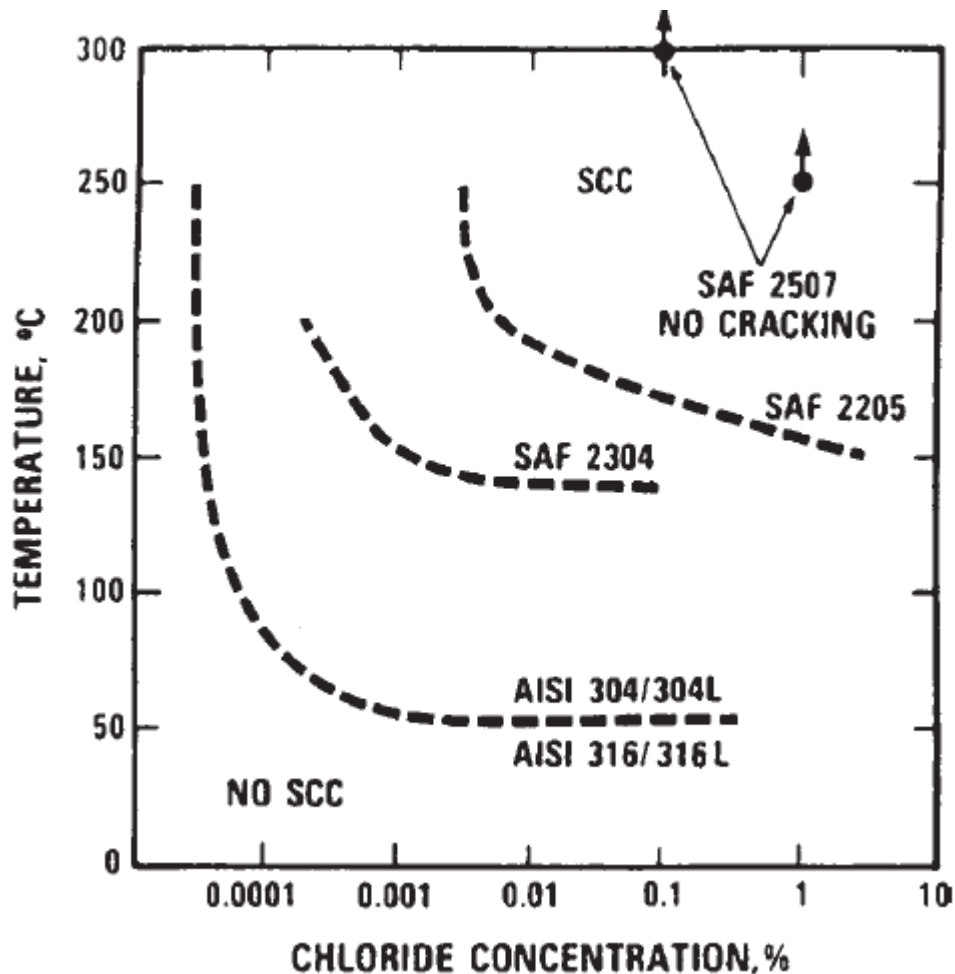
Figure 2.4: The relationship of temperature and chloride ion concentration of austenitic and duplex stainless steels (Kaneko, 2007).

In austenitic stainless steels, the chloride ions will disrupt the passivation layer in the presence of tensile stresses leading to the propagation of SCC cracks. The chloride ions concentrations are often lower than 2M (Torchio and Venezian, 1980). An increase in the chloride concentration will result in a decrease of the passivation rate thus allowing pits to form on the surface of the substrate (Nishimura and Maeda, 2004). However, the lower

chloride concentrations will reduce the acidity of solution. Kim et al. (1998) reported that addition of tungsten improves corrosion resistance in austenitic stainless steels when exposed to lower chloride concentration solutions, but this did not hold when Cl⁻ were increased. The study conducted by Saluja and Moeed (2012) showed electrochemical noise in the passive region of austenitic stainless steel when the chloride concentration was increased.

2.2.3.2 Hydrogen absorption

Hydrogen in steels depends on the stress concentration, chemical composition and the microstructure at a particular region. Hydrogen can be introduced in steels by pickling, corrosion, welding and electroplating. Failures have been reported where hydrogen was generated by corrosion reaction, galvanic couples and cathodic protection (Copson, 1956). The hydrogen is enhanced by corrosion reactions especially when the metal is exposed to sulphide containing environments where the cathodic reaction accelerates cracking. The hydrogen absorption rate is governed by chemical factors which depend on plastic deformation of the metal before or during experiment. Ghosh and Kain (2010) reported that surface machining caused the transformation of austenite to strain induced martensite which allowed hydrogen diffusion. The pressure created by molecular hydrogen in cavities lead to microcracks at grain boundaries (Vlasov and Fedik, 2008).

According to Bueno et al. (2008), the applied potential and strain are detrimental parameters which contribute to SCC and HE of buried pipes. At potentials of 300 mV below corrosion potential, transgranular SCC is usually observed. Barsanti et al. (2008) reported less susceptibility of steels to HE as the potential was increased. The severity of HE in steels can be tested by slowly bending the specimen under cathodic protection by allowing high plastic deformation without necking. The hydrogen absorption level is higher in steels at elevated temperatures as shown in Figure 2.5. This is often achieved during casting or welding processes of steels.
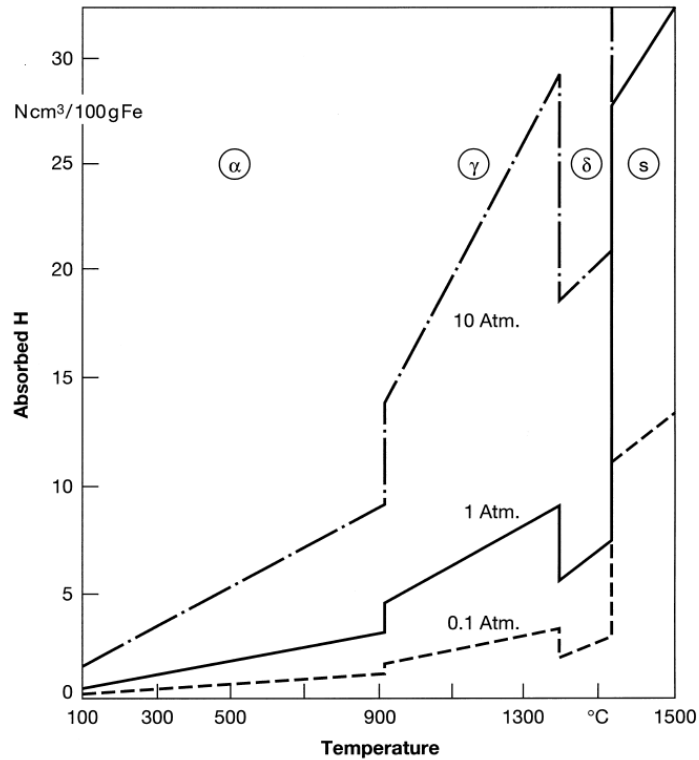
Figure 2.5: Solubility of hydrogen as a function of temperature and pressure (Woodtli and Kieselbach, 2000).

It is important to control hydrogen absorption in metals as it can result in forming cold cracks "fish eyes", which can lead to the development of SCC cracks when the metal is in operation (Schweitzer, 2013; Woodtli and Kieselbach, 2000). The presence of hydrogen in a metal promotes vacancies which can be associated with plastic deformation resulting in a decrease of corrosion crack growth resistance (Shimomura and Nagumo, 2008).

2.2.3.3 Dissolved oxygen

Dissolved oxygen (DO) is another parameter which contributes to accelerated SCC crack growth of austenitic stainless steels in chloride solutions at elevated temperatures (Truman, 1977). Oxygen levels can also enhance localised attack in metals by the concentration cell formed between the electrolyte within the crevice (which is oxygen starved) and the electrolyte outside the crevice where oxygen is more plentiful (Davies, 2000). If there is an oxygen concentration difference, corrosion is enhanced inside the crevices. This can further be enhanced by galvanic corrosion when two dissimilar metals are in contact surrounding the crevice (Scully, 1975). Corrosion resistance of metals is more likely to decrease in the presence of oxygen.

Moreover, the presence of DO produces an oxidising environment favourable to pit initiation (Cabrini et al., 2017). At high temperatures above 150°C the level of DO decreases and this can reduce the propagation of shallow pits. Truhan and Hehemann (1977) reported a shift of rest potentials when oxygen was introduced in chloride solutions. The addition of oxygen to sodium chloride solutions induces SCC susceptibility in austenitic steels, but it will take longer time to fail (Edeleanu, 1953).

2.2.3.4 Temperature

Previously it has been shown that SCC is more likely to occur at temperatures above 25ºC. Zhong et al. (2017) reported increased severity (22.3%) in SCC when the temperature was increased from 40 to 60°C for austenitic stainless steels. Increased temperature also lead to fracture transformation from ductile to brittle (Zhong et al., 2017). This correlated to the study conducted by Huang et al. (2015) where both ductile and brittle fracture was observed. The other effect of temperature on SCC is that it reduces the tensile strength and elongation of the material. However, the study conducted by Alyousif and Nishimura (2006) revealed fracture transformation from TGSCC to IGSCC when temperature was decreased on austenitic stainless steels. This was due to the formation of martensite at grain boundaries. Type 304L stainless steel is susceptible to hydrogen embrittlement at temperatures below 140°C and prone to SCC at temperatures above 140°C (Alyousif and Nishimura, 2006). The crack initiation of stainless steels due to SCC occurs at approximate less than an hour at temperatures above 160°C as shown in Figure 2.6. At lower temperatures, a crack will take longer time to initiate.
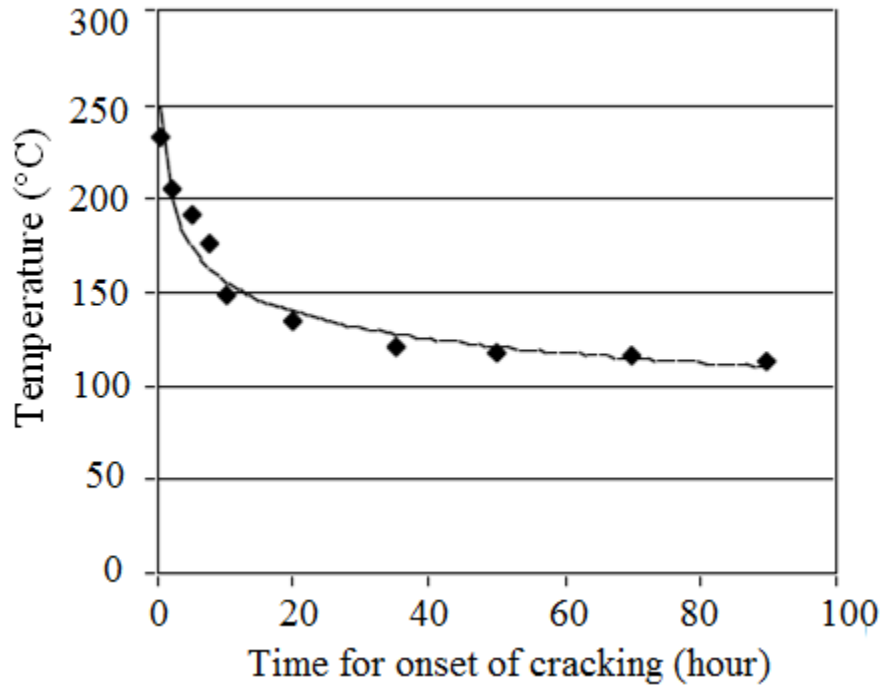
Figure 2.6: Effect of temperature on SCC of stainless steel (Fontana, 2005).

Ma and Ling (2013) found that temperature and time played a significant role in SCC, a crack initiated at elevated temperatures (above 130˚C) and no crack was observed at lower temperatures (below 40˚C) of stainless steels exposed in chloride solutions for over 700 hours. SCC crack initiated by localised corrosion or mechanical defects is often related to pitting intergranular attack.

2.2.4   Effect of applied stresses

The most important stresses which contribute to SCC are tensile and residual stresses. The tensile stresses are introduced by the application of external forces, whereas residual stresses are usually introduced by casting, forging, heat treatment, machining and welding operations.

The role of elastic and plastic deformation due to tensile stresses can contribute to SCC depending on the material and the environment. Gutman et al. (1996) reported a constant active dissolution rate of iron when the plastic deformation increased. The effect of plastic deformation on the active dissolution may be enhanced with increasing heterogeneity of dislocation structures (Lu et al., 2009). The applied tensile stress below yield increases the level of atoms energy in the stress lattice hence increasing the chemical potential of surface

atoms. Gati et al. (2017) investigated the effect of tensile stress on SCC using tension method and it was found that the corrosion rate increased as tensile stresses were increased. The applied stress widened a v-notch and allowed dissolution to occur. On the other hand, the residual stresses promotes SCC by delaying either the metal dissolution of hydrogen entry (Toribio and Kharin, 1997).

The dominance of SCC in the elastic region can be confirmed by the small differences in stress-strain behaviour as shown in Figure 2.7. This was illustrated by slow strain rate tests (SSRT) and the susceptibility of alloys to SCC was reported based on the crack growth rate.
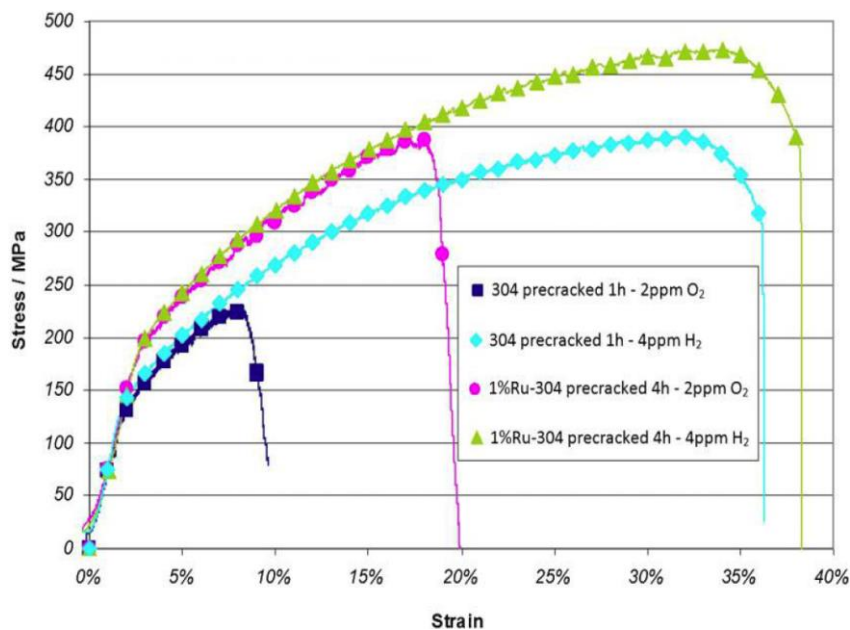
Figure 2.7: SSRT curves of 304 stainless steel in oxygenated water (Scenini et al., 2012).

Terachi et al. (2012) measured the crack growth rate of 304 stainless steel using direct potential method where an increase in crack growth was observed as the stress intensity increased. In contrast, Scully (1975) pointed out the difficulty of measuring the crack propagation rate due to different SCC mechanisms which can be present on the specimen. SCC cracks can propagate as a result of anodic dissolution while others propagate as a result of locally absorbed hydrogen.

The other technique which can be used to measure the crack growth rate is the slip oxidation model. This model is based on the assumption that anodic reactions occur within the crack, and cathodic reactions occur both within the crack and external surface. Zhang and Wang

(2014) performed measurement of crack growth rate by using thick compact tension specimen in a simulated pressurised water reactor environment. Their method was based on linear fracture mechanics for stress intensity. Similarly, Turnbull and Zhou (2008) used fracture mechanics to measure the crack growth rate of stainless steel at elevated temperatures in chloride solution.

2.2.5   Effect of potential on EAC

The susceptibility of alloys to EAC such as SCC and HE depend on the electrochemical potential.   More negative potential will increase the level of hydrogen absorbed and subsequently leading to HE. The positive potentials will also increase hydrogen entry than the free corrosion potentials (Schweitzer, 2013). SCC often occurs between the active and passive regions as shown in Figure 2.8. This correlated with the work performed by Tsai and Chou (2000) where SCC of alloys was above the pitting corrosion potential. It is common that the alloy surface will be in the passive region where its crack tip is in the active or pitting region (NPL, 2016).
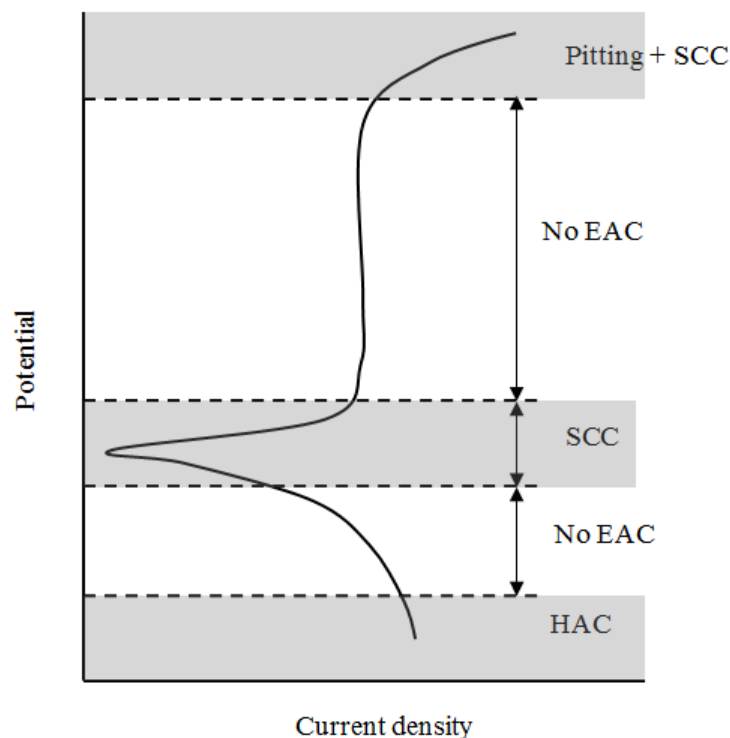
Figure 2.8: The effect of potential on EAC susceptibility of stainless steels (Redrawn from Tsai and Chou, 2000).

Tsai and Chou (2000) reported that SCC of duplex stainless steels occurs at a potential range of -380 to -500 mV in concentrated sodium chloride. They also found that the alloys were immune to SCC in the anodic passive region and at OCP. This was consistent to the work conducted by Lu et al. (2010) on the EAC mechanism of pipeline steel in near neutral pH ground water.

2.2.4.1 Electrochemical measurements

Despite the effect of potential on EAC, it is important to understand the electrochemical measurements when investigating the corrosion characteristics of the metal surface in a corrosive environment. Two methods that are often employed to explore corrosion resistance are the open circuit potential (OCP) and potentiodynamic polarisation.

(i) **Open circuit potential**: The potential is recorded during electrochemical reactions of the solution at the metal-solution interface. During this process the corrosion potential (E_{corr}) can be measured over time. The corrosion potential of stainless steels will gradually increase as the passive film is formed on the surface, thus improving corrosion resistance (Delaunois et al., 2016). A decrease in potential will indicate that corrosion is enhanced and the electrochemical noise is probable during the measurement. The corrosion potential, OCP and corrosion current density are the essential parameters used in understanding the behaviour of the corroding metal.

(ii) **Potentiodynamic polarisation:** Potentiodynamic polarisation can be achieved by varying the electrode potential while measuring current flow. This method is widely used to measure the corrosion resistance of metallic materials. The measured corrosion current can be used to determine the corrosion rate in millimetres per year as indicated in Equation 2.1.

$$corrosion\ rate = \frac{0.00327 \times i_{corr}(EW)}{Ad} \qquad (2.1)$$

Where A is the surface area in cm^2, d is the density of alloy in g/cm^3, i_{corr} is corrosion current in μA and EW is the equivalent weight.

When the metal is freely corroding, the electrons generated at anodic areas will flow through the metal to react at cathodic areas (Tabolt and Tabolt, 1998). Corrosion of metals take place mainly due to reduction-oxidation reactions where the electrons are exchanged explicitly (Ahmad, 2006). The electrochemical reaction is often associated with the chemical transformation that implies the transfer of charges across the interface between the electrode and the electrolyte (Landolt, 2007). Polarisation characteristics can be determined experimentally by using a potentiostat and specialised computer software to acquire data and a polarisation curve as shown in Figure 2.9.
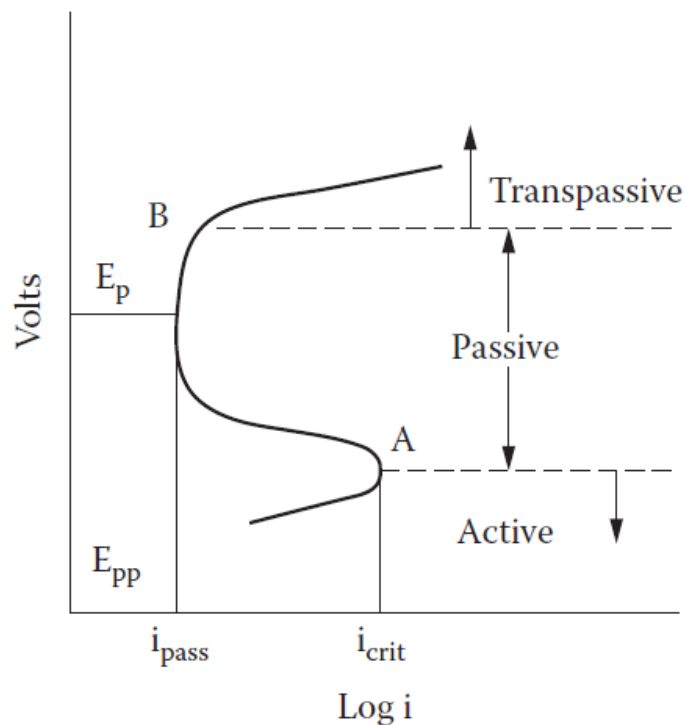
Figure 2.9: Anodic polarization characteristics of stainless steels (Schweitzer, 2013).

The anodic polarisation curve provides important information such that the corrosion rate in the passive region can be measured. The effect of alloy additions can also be understood from these curves. As depicted in Figure 2.9, the metal will corrode in the active region when the applied potential becomes more positive. The current will decrease at the critical current when the passivation film is formed. The breakdown of the passive film of stainless steels occurs at higher potentials in the transpassive region. Moreover, the pitting potential will break the film in small isolated sites over the metal surface creating passive cells (Schweitzer, 2013). The polarisation characteristics differ from electrode to electrode hence designing precise reference electrodes is essential.

2.2.4.2 High temperature electrode design

The electrochemical measurements at high temperatures (above 100°C) have been performed for many years and today there is no specific method which works perfectly without sporadic electrochemical data. There is rebuttal work on electrochemical behaviour of metals at high temperatures. Electrochemical experiments at high temperatures can be achieved either by using internal or external reference electrode method (Wildgoose et al., 2004). The internal reference electrode is placed in the same media as the working and counter electrode at high temperature. This method can produce erratic results at high temperatures. The external reference electrode method can be achieved by using an external pressure bridge reference electrode (EPBRE) where the electrode is connected externally by a salt bridge and set to the same pressure as the corrosion cell.

It is a common practice to use an external electrode to improve the instability of results at high temperatures, but the difficulty lies in balancing the pressure between the thermocell and external reference electrode. The other problem is the isothermal liquid junction which is created when both solutions (salt bridge and electrolyte) come into contact as a result of mass transfer interactions (Ubah and Asselin, 2009). Balancing the pressure is required to avoid the contamination of the solution by the electrolyte bridge (Bosch et al., 2003). Dilution of the electrolyte bridge can lead to a drift of reference electrode potential. Other methods used to maintain the pressure include the heat shrinkable polytetrafluoroethylene and high pressure pump (Lvov et al., 2005). In the study conducted by Macdonald (1979), it was reported that the isothermal liquid junction potential across the boundary of the internal and external solution reduced in higher concentration of potassium chloride. The effective method of heating up an electrolyte is by using an autoclave. Lvov et al. (2005) designed an electrochemical cell out of Hastelloy B in order to measure the potential and corrosion rate at temperatures above 300°C. It was concluded that the better constructed electrode gives better measurable corrosion current values. Similarly, Ubah and Asselin (2009) developed an electrochemical cell based on the EPBRE, and already there were challenges encountered; the uncertainty of results increased as the temperature and pressure was increased.

2.3 Alloying techniques

The corrosion resistance, wear resistance and mechanical properties of alloys can be improved using either one of the commonly practiced alloying techniques such as electroplating, galvanizing, thermal spraying, ion implantation, laser surface alloying, and vacuum arc remelting. In this study, the laser surface alloying and vacuum arc remelting will be explored further.

2.3.1   Laser surface alloying

Laser surface alloying (LSA) is a surface coating technique which improves the surface properties by applying an alloy in the form of a powder to a metal workpiece. The thickness of the treated zone can be 1-2000 µm, and very thin quenched alloy regions can be made using Q-switched Nd-YAG lasers (Steen, 2003).

The alloying powders can be deposited either by pre-deposition or co-deposition method. Pre-deposition is achieved by applying a layer of alloying element on a substrate and melted with laser beam. The major limitations of alloying using this method are (i) the powder can be blow away as the laser beam is struck on the surface (ii) the high energy is required to melt the layer (iii) it is difficult to control process parameters and a uniform bed thickness (Steen, 2003). However, the co-deposition is a single step processing, and it is for this reason that it is often practiced by many industries. The co-deposition involves direct deposition of the alloying element during laser irradiation; the alloying element is deposited mainly in the form of gas and powder (Jianglong et al., 1993). Powder stream is fed on the surface as the laser beam is scanned forming a melt pool of the desired coating as shown in Figure 2.10.
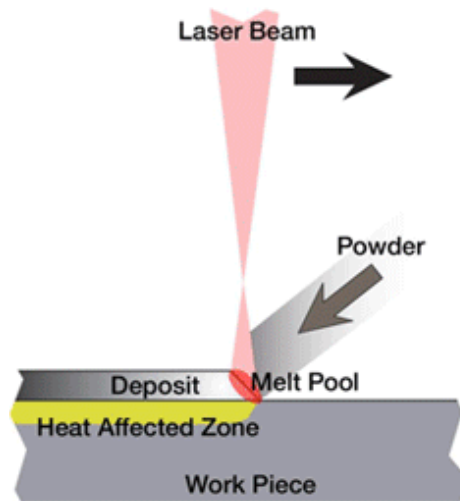
Figure 2.10: The process of laser surface alloying (MetalAM, 2014).

The advantage of using co-deposition over pre-deposition is that, it provides optimum bonding, low distortion and complex substrate geometry which can be laser alloyed. The advantages and disadvantages of using LSA technique are shown in Table 2.2.

Table 2.2: The advantage and disadvantage of LSA (Ion, 2005; Bergman, 1994; Bruck, 1988)

ADVANTAGES	DISAVANTAGES
(i) It is good for improving wear and corrosion resistance of metallic components.	Rapid melting and re-solidification can result in complex and metastable phases.
(ii) There are no external mechanical forces acting on the substrate during LSA process. No wearing of tools.	Residual stress induced during the process can contribute to SCC.
(iii) It is regarded as the quickest and simplest form of alloying since the parameters can be controlled to meet the required weld specifications.	Imbalance of LSA parameters can lead to cracks and porosity of the weld pool, and excessive dilution of the substrate.
(iv) It consumes less power when compared to other alloying techniques such as laser glazing and laser peening.	Trials should be run to adjust the allowing parameters for every different powder and metal used.
(v) Formation of fine microstructure and small region of heat affected zone.	Due to heat treatment of the weld bed, it can be difficult to reveal the microstructure.

In engineering applications, LSA is considered the most effective and cost friendly because a small amount of expensive powder can be used to alloy a low cost substrate which can lead to corrosion resistance and metal enhancement. Laser material processing can be used in a variety of applications depending on whether high energy is required to modify phase transformation or low energy for general applications such as laser cutting and scribing. The most recent applications of LSA are found in wireline cylinder head in petrochemical industries, extruder screw used for plastic machinery, stainless steel gate valve, jet engine turbine blade notch, diesel engine inlet valve, and steam turbine blades (Bergmann, 1994; Amende and Nowak, 1990; Bruck, 1988). These applications have proved the use of LSA to be successful over other alloying techniques which could be costly and time consuming.

2.3.1.1 LSA parameters

The important LSA parameters which can be altered are laser power, beam radius and scan speed (Kwok and Wong, 2010; Ion, 2005; Draper and Poate, 1985; Pawlowski, 1999). LSA diagrams such as the one shown in Figure 2.11 are usually used to select the parameters for the laser alloying procedure. Other parameters which cannot be controlled during laser surface process is the interaction time and cooling rate.
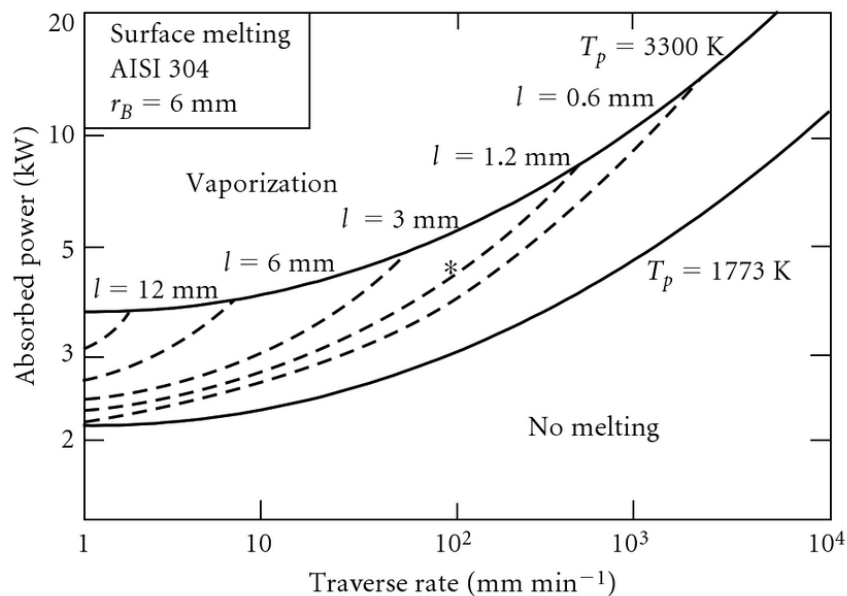
Figure 2.11: Calibrated model based of laser surface melting of AISI 304 using a beam of width 12 mm (Ion, 2005).

The correct parameters are selected to allow bonding of the substrate and provide a defect free layer. The lower laser power will result in a flat weld bead shape and decreasing the scanning speed reduces the quality of the bond and the dilution rate (Bax et al., 2012; Brytan et al., 2010). Mudali et al. (2006) concluded that laser surface alloying austenitic stainless steels with Cr and Ni powders will improve the pitting corrosion resistance at a laser power of 2.5 kW and scanning speed of 1.8 m/min. This correlated with the study conducted Yao et al. (2008), where the corrosion resistance and hardness was improved by laser alloying steel with mixed powders of Cr, Ni, Co, and WC at laser power of 1.5-2 kW and scanning speed 0.3-0.60 m/min. Thawari et al. (2003) also emphasised that the high energy density of low scan speeds lead to severe oxidisation of the substrate and can lead to excessive dilution. In addition, high flow rates will lead to excessive melting of the specimen and formation of small globules on the surface.

2.3.1.2 LSA powders

There are few readily available alloying powders used for LSA process. The selection of alloying powders depends on the material of the specimen; it is not every alloying powder that can be bond on every metal. Nickel-base alloys are used to improve ductility of the substrate whereas the cobalt-base alloys are used to improve the corrosion resistance in severe environments (Davies, 2000). Tungsten carbide has a good bonding in steels; the particles will mix with iron and form a softer layer of iron tungsten carbide. Iron base alloys are used for desirable application at low cost. These coatings are typically used in equipment with exposure to severe wear conditions such as crushing and grinding equipment.

Moreover, PGMs can be used as LSA powders to improve the corrosion resistance and mechanical properties of the substrate. Van der Merwe and Tharandt (2015) reported improved corrosion resistance of laser alloyed stainless steel with lower Ru content. Similarly, Bax et al. (2012) reported improved corrosion resistance of laser alloyed mild steel with mixtures of Al and Ru powder. They also reported completely crack free layers, and the fraction of the alpha-phase in the top layer decreased with every additional layer. In addition, hard and wear-resistant layers can be achieved by laser alloying SiC powder with medium carbon steel.

2.3.1.3 Microstructure and hardness of LSA stainless steels

The microstructure of laser alloyed surface consists of three main regions; laser alloyed zone (LAZ), heat affected zone (HAZ) and base metal (BM) as shown Figure 2.12. Kumar et al.(1993) observed that an area close to the LAZ interface contained a thin band of a planar solid interface, consistent with the highest temperature gradient and lowest solidification rate during the initial stages of solidification. Lekala et al. (2012) reported the LAZ to be free of cracks. In contrast, Yang (2003) observed cracks in the LAZ as a result of thermal stresses introduced by high cooling rates and the difference in thermal expansion coefficients of the alloying powder and the substrate.
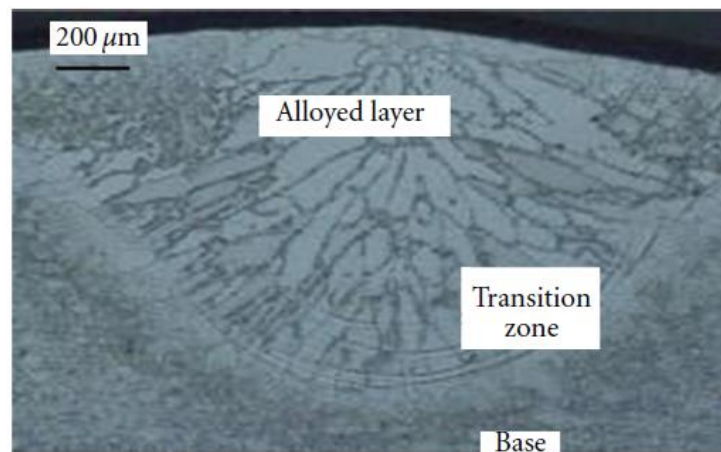
Figure 2.12: Cross-section of laser surface alloyed 316L stainless steel with Ru (Lekala et al., 2012).

The microstructure of laser surface alloyed layer consists of different zones (superficial zone, ferrite and austenite) and alloying powder particles embedded in the surface which increase the surface roughness and affect mechanical properties (Brytan et al., 2010). It was reported by Tjong et al. (1996) that the microstructure of Ru (23.3 wt%) laser alloyed layers consisted mainly of fine cellular dendrites. This was in accordance to the work conducted by Zhang et al. (2014) where the microstructure of laser alloyed layer had planar and columnar dendrites at the core and top surface of the substrate. Kwok and Wong (2010) found that laser alloyed 304 stainless steel with FeCrMoMnWCB possessed improved wear and corrosion resistance. The presence of epitaxial growth of austenite grains in the molten surface occurred due to the planar growth during the initial stages of solidification (Kwok and Wong, 2010). The microstructure of laser alloyed surface can be achieved by high

solidification and cooling rates which will result in improved corrosion resistance and wear. Microstructural features usually depend on the temperature gradient, solidification velocity, cooling rate, and the interface of solidification during LSA process (Yao et al., 2008). However, the solidification process has implications; it increases sensitivity on the clad and HAZ to cracking. These implications are often reduced by altering the alloying parameters such as the laser power and scanning speed(Zhang et al., 2010).

The work (Zhang et al., 2014; Lekala et al., 2012; Brytan et al., 2010; Kwok and Wong, 2010; Tjong et al., 1996) conducted previously has shown a significant improvement of microhardness of laser alloyed layer alloys. Figure 2.13 shows the microhardness of laser alloyed austenitic stainless steel with Cr at different laser alloying conditions of laser power and powder feed rate. The unstable data points can be attributed to various microstructures in different local areas in the alloyed layers (Tjong et al., 1996).
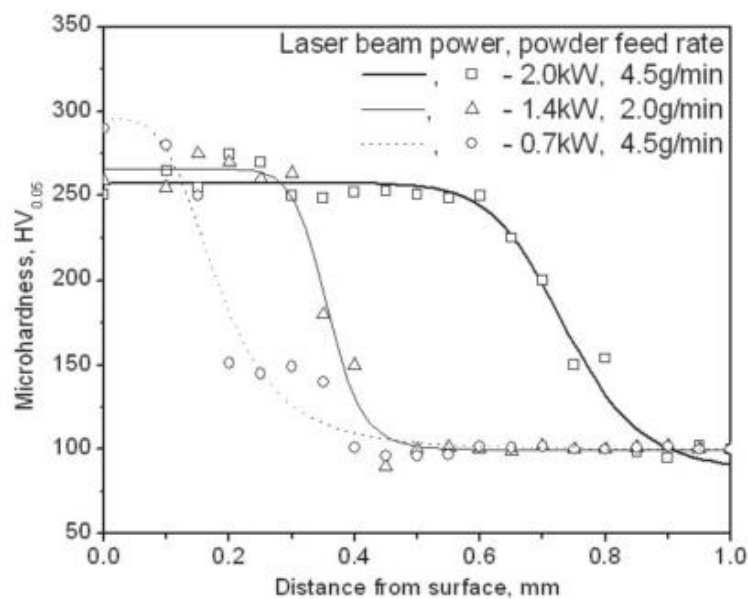
Figure 2.13: Microhardness of Cr laser alloyed 316 stainless steel at various laser beam power and powder feed rate(Brytan et al., 2010).

The study conducted by Yang (2003) showed that laser cladding of a mixture of a nickel base alloy and tungsten carbide powder on a mild steel substrate improved microhardness near the bonding interface. Yao et al. (2008) observed that the hardness decreased from the alloyed layer to the base metal because of the existence of the Fe_6W_6C and W_2C in the alloyed region.

2.3.2 Vacuum arc remelting

Vacuum arc remelting (VAR) is a secondary melting process of solid metal by using an arc under a vacuum. The process is performed by remelting the specimen in a hearth. The electrode metal (sample) can be placed in a vacuum with an alloying element and heated by the intense heat of an arc while the ingot is placed on a hearth. VAR is often a preferred alloying method over other conversional melting techniques because it removes oxides, nitrides and dissolved gases such as hydrogen and nitrogen during the melting process (Chapelle et al., 2001; Zanner et al., 1989). The ingots with reduced macro and micro segregation can be produced on a large scale.

The defects that are associated with VAR are tree ring patterns, freckles and whites found after solidification process (ALD Vacuum technologies, 2016). The effect of freckles on mechanical properties is detrimental. It was reported that the presence of freckles reduce yield strength by approximately 20% (Eiselstein, 1965). According to (Kou et al., 1977), it was observed that an increase in depth of mushy zone and decreasing solidification rate resulted in increasing macro-segregation. The high power input contributed to a deeper metal pool and mushy zone size. However, the defects can be reduced by a stable melt rate, controlling arc gap, and power supply.

The arc behaviour inside the furnace is coupled by pool dynamics and solidification rate. This is achieved by the distribution of current which drives the fluid within the molten pool. The power distribution dictates both the boundary conditions and the magnitude of the boundary buoyancy driven flows in the molten pool (Williamson et al., 1988). The contributing factors of the VAR process such a melt rate, arc voltage, arc configuration, and ingot surface are highly important to the steadiness and levels of the furnace parameters such as electrode gap, ambient gas pressure, and arc current. In addition, computer packages can be used to simulate heat and mass transfer throughout the ingot and melt pool under the influence of the arc. Such simulation models are good at predicting the influence of processing parameters upon the changes in structure (Atwood et al., 2004). Typical applications of VAR is in ball bearing steels, tools steel and super alloys for aerospace.

CHAPTER 3

EXPERIMENTAL PROCEDURES

The description of the experimental procedure gives the methods and equipment used to meet the objectives of this research. The alloys were produced based on two techniques, namely: lasers surface alloying (LSA) and vacuum arc remelting (VAR). The tests performed were the SCC test, slow strain rate test and electrochemical test. These tests were performed according to the material testing standards, as well as complying with health and safety regulations. The methods used to reveal microstructure and hardness are discussed. The experimental workflow in Figure 3.1 shows a summary of the work conducted in this study. In this diagram the main work is linked by arrows and each method or test is briefly described.

Sample preparation
- Measure 304L stainless steel plate.
- Cut and remove dirt from samples

Laser surface alloying
- Alloy 304L stainless steel substrate with powders of 304 + Ni and varying Ru content (0,1,2,5 and 10 wt%)

Vacuum arc remelting
- Alloy 304L stainless steel at varying Ru contents (0, 1, 2, 5 and 10 wt%).

Microstructure and hardness
- Evaluate microstructure and determine grain size with optical microscope
- Determine hardness

Slow strain rate testing
- Test solution (50 ppm NaCl solution at 160°C containing 10 ppm DO)
- Determine SCC failure time and max stress threshold

Electrochemical tests
- Determine corrosion rate
- Analyse the passivation behaviour and pitting of alloyed samples

MICROSCOPY/EDS
- Determine chemical composition
- Analyse microstructure, crack propagation and fractography

Bent beam SCC test
- Test solution (50 ppm NaCl solution at 160°C containing 10 ppm DO for 172 hours)
- Investigate SCC susceptibility

Figure 3.1: Experimental workflow of test program.

3.1 Sample preparation

Type 304L stainless steel was produced and supplied by Outokumpu. The samples were laser alloyed at the CSIR and VAR samples were prepared at Mintek. The preparation procedure is described in the following sections.

3.1.1 Laser surface alloying

Rectangular coupons of approximately 80 x 50 mm were laser cut from 304L stainless steel plate (5 mm thick). The coupons were sand blasted to remove any oxide layer so as to allow easy absorption of the laser on the surface. A coupon was held on a focal plane to defocus the laser by 20 mm. The type of laser used was Rofin Sinar DY044 with Precitec YW50 welding head configured at 200 mm FL collimator and 300 mm FL lens. The laser power was set at 1.75 kW. The two hoppers of 304 and Ni powders were fed with a medium groove disc whereas the Ru powder hopper was fed with a small groove disc. The flow rate on each hopper was set at 2 l/min and the carrier gas (argon) at 6 l/min. A co-axial nozzle tip was positioned 12 mm from the substrate. The cladding process was started at a scanning speed of 1.75 m/min and a cladded layer (30 x 20 mm) was formed on the surface as shown in Figure 3.2. The overlapping was achieved at 60%.
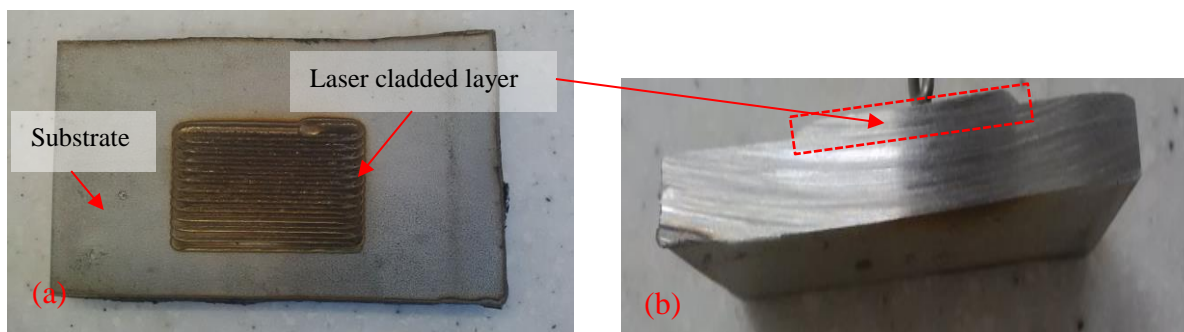
Figure 3.2: Laser cladded 304L SS with Ru (a) top view (b) cross-section after cutting.

A finished coupon had multiple weld beads formed on the surface of the substrate. This was due to a weld bead that was set at a distance (centre to centre) of 0.8 mm. Some of the coupons which were slightly distorted after laser cladding were not used in this study. It is important to note that the samples were laser cladded at varying Ru content of 1, 2, 5 and 10

wt%. A low concentration of Ni (2 wt%) was added to enhance corrosion resistance of 304L stainless steel at higher temperatures.

3.1.2 Vacuum arc remelting

The VAR technique was used to alloy 304L stainless steel with Ru. The dissolved gases were removed by introducing argon gas into the vacuum chamber of the furnace for 30 minutes before melting the sample. Pure titanium was then melted to remove any possible residual oxygen in the atmosphere. A 304L stainless steel coupon weighing 70 g was melted with the compressed Ru powder. A homogenous structure was attained by remelting the samples a few times and cooling them in the furnace for 45 minutes. This process removed dissolved gases such as hydrogen, nitrogen and carbon dioxide. Macro-segregation was eliminated and micro-segregation minimised. The alloyed ingot shown in Figure 3.3 was annealed at 1060°C for 60 minutes, flattened by rolling to a thickness of 8 mm, and cooled in air at room temperature. While reducing the thickness of the samples on a rolling machine, it was important to avoid the formation of cracks by selecting an appropriate force exerted by the rollers. Surface milling was then employed to ensure a flat surface. The process was repeated for five samples at varying Ru contents of 0, 1, 2, 5 and 10 wt%.

Figure 3.3: Type 304L stainless steel ingot alloyed with 1 wt% Ru.

The produced ingots were free from freckles and white spots which could have been formed during the solidification process.

3.1.3   Metallography

The metallography stages employed to prepare samples for microstructure and elemental analysis are; sectioning, mounting, grinding, polishing and etching.

(i)   **Sectioning and mounting**: Only cold cutting was performed in order to avoid altering the microstructure of the sample, which can lead to an incorrect metallographic interpretation. Laser cladded coupons were cut into small strips of 30x5x5 mm by using a Brilliant 200 abrasive cutter. The samples were observed with unaided eye for any surface deformation and cracks. After cleaning the samples with acetone, they were mounted in Bakelite using Opal 410 mounting machine. Vacuum remelted samples of approximately 10x10 mm were cut using a hacksaw and cold mount in Bakelite.

(ii)   **Grinding and polishing:** The samples were progressively ground on a manual Knuth Rotor grinding machine with 500, 800 and 1200 grit silicon carbide papers. At every grinding stage (i.e change of grit paper), the sample was rotated at 90° and the grinding angle was kept constant in order to minimise scratches on the surface of the sample. The first step was critical as the sample was ground with light pressure applied at the centre to remove insufficient metal and flatten the surface. The subsequent grinding steps were performed by wet grinding to reduce the frictional heat which can develop on the surface during the grinding process. At every step the sample was washed in running water to remove abrasive particles that might have embedded on the surface.

Polishing was done based on two steps: preliminary and final polishing. The preliminary polishing was conducted to retain all secondary phases and maintain the microstructural integrity. The samples were polished using 3 micron Struers polish and 2 micron cloth on a rotary wheel. The samples were held against the rotating wheel with minimum-medium pressure applied. After 3 minutes of polishing, the samples were examined and washed with water, rinsed in ethanol and dried with compressed air. A final polish (1 micron Struers) was used to eliminate any surface damage that could have resulted from grinding. The polishing cloth was kept wet at every stage to avoid pits, dragging out of inclusions, comet tails, staining and bluffing which could occur on the surface of the specimen.

(iii) **Etching:** Etching was performed to reveal the microstructural features such as grain boundaries and phase structure. Two etchants, marble's reagent and 10% oxalic acid were used to reveal the microstructure of laser alloyed samples. A small quantity of marble solution was poured into petri dish and the sample was immersed for 5 seconds, cleaned with running water and rinsed in alcohol. The sample was then electrolytically etched at room temperature with 10% oxalic acid for 1 min at 8 V and washed in running water and rinsed in alcohol. Only one etchant was used for VAR samples, there were electrolytically etched with 10% oxalic acid at 8 V for 2 mins.

3.2   Microstructural characterisation

Material characterisation was first done by evaluating the microstructure of alloyed samples. The microstructure was examined by using Leica optical microscope and scanning electron microscopy (SEM). This helped in understanding the alteration of the grain boundaries, identifying inclusions, defects, porosity and bonding evaluations. EDS was used to determine the elemental chemical composition of alloyed samples with Ru.

The grain size of LSA and VAR samples was measured according to ASTM E112-12 using an optical microscope and the procedure was as follows:

- The samples were ground and etched as described in section 3.1.3, and viewed with an optical microscope (Olympus SC50) for grain size measurements.

- The region of analysis (on the sample) was selected at 100X magnification. It was ensured that this region was free from defects or any damage from LSA or VAR process. Atleast three regions were selected in order to improve the accuracy of the calculated grain size number.

- A circular intercept method was used to calculate the grain size number (G) as per ASTM E112-12 where the number of grains per unit length of test line were counted to obtain the mean lineal intercept length.

3.3 Microhardness testing

Microhardness measurements are essential for understanding the material resistance to indention and plastic deformation. The hardness of the investigated alloys was measured by using a Future-Tech FM-700 Vickers tester. The hardness profile was measured on the cross section of the sample from the alloyed zone, to the transition zone, through the heat affected zone to the base metal. The force was applied at 500 gf for 10 seconds dwell time and the measurements were recorded at 100 µm interval cores indentation. The indentation was performed on ground and polished samples. The microhardness of VAR samples was obtained by measuring ten indentations on the surface and averaging the value.

3.4 Corrosion experimentation

Corrosion testing methods used were; bend beam stress corrosion test, slow strain rate testing and electrochemical test. These methods were used to understand the susceptibility of Ru alloyed 304L stainless steel to corrosion.

3.4.1 Bend beam stress corrosion test

Bend beam stress corrosion test was used to determine the stress corrosion behaviour of laser alloyed samples according to ASTM G39. Hand calculations and the calibration of samples (Appendix C) were conducted before starting the experiment. The yield and tensile strength of as-received 304L stainless was determined by using Tinius Olsen tensile testing machine. Three samples were tested and the average yield strength value was used in the calculations. The stress-strain curve shown in Figure 3.4 revealed yield strength of 420 MPa, and it was consistent to the one stated on the supplier's material datasheet (Outokumbu, 2015). The ultimate tensile strength obtained was 695 MPa.
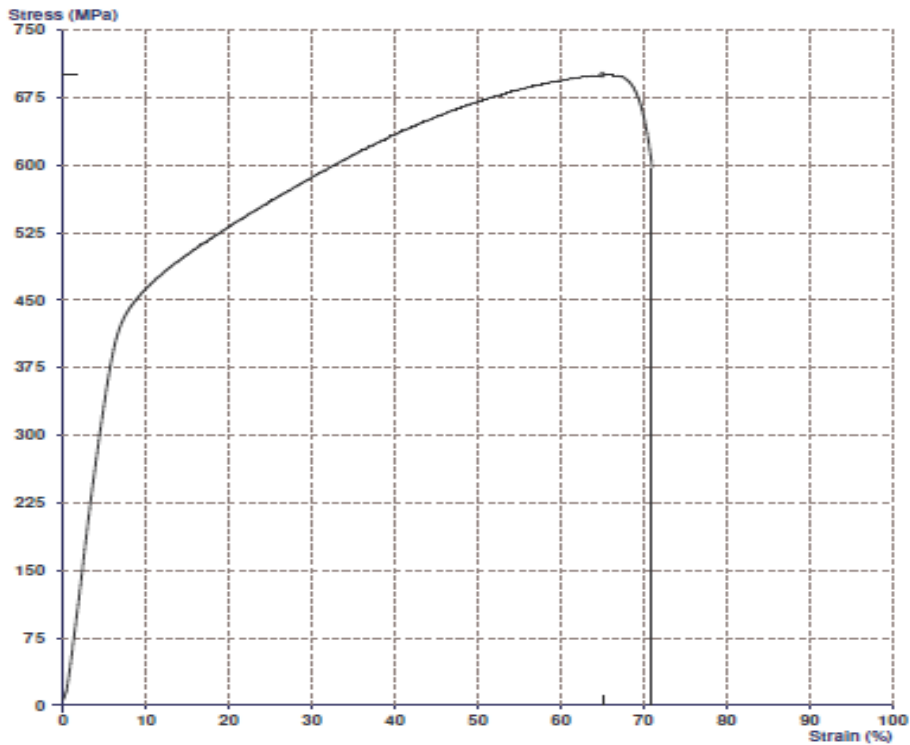
Figure 3.4: Stress- strain curve of as-received 304L stainless steel.

Finite element analysis (FEA) model was used to determine the stress distribution of the sample stressed on a three-point bend rig. The FEA simulation was performed on a rectangular model of 40x5x5 mm with physical and mechanical properties similar to those of 304L stainless steel. The model method gave a good estimation of the region of high tensile stresses. At applied load of 20 KN, the maximum tensile stresses was 473 MPa as shown in Figure 3.5.
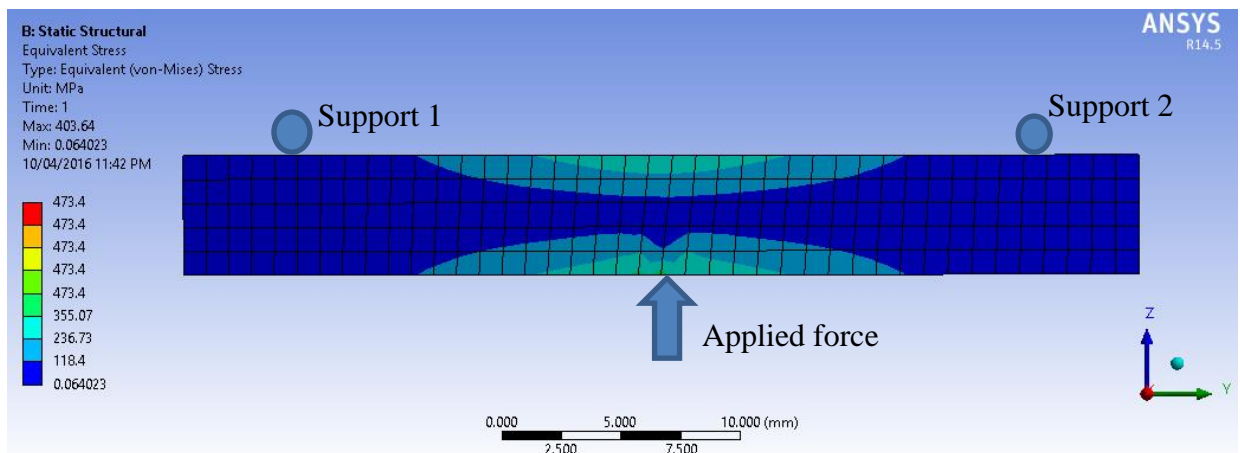
Figure 3.5: Stress distribution of 304L stainless steel stressed on a three point bend rig.

It is evident that equivalent stresses up to 355 MPa can be reached without deforming the sample permanently. FEA gave a good approximation and estimation on how the rig can be designed in order to get appropriate tensile stresses on the region of interest.

After determining the stresses to apply on the sample without permanent deformation, LSA samples were then mounted with stain gauges and calibrated as described in appendix C. The samples were stressed to 350 MPa (approximately 80% of yield strength) on a three-point bend rig as shown in Figure 3.6.
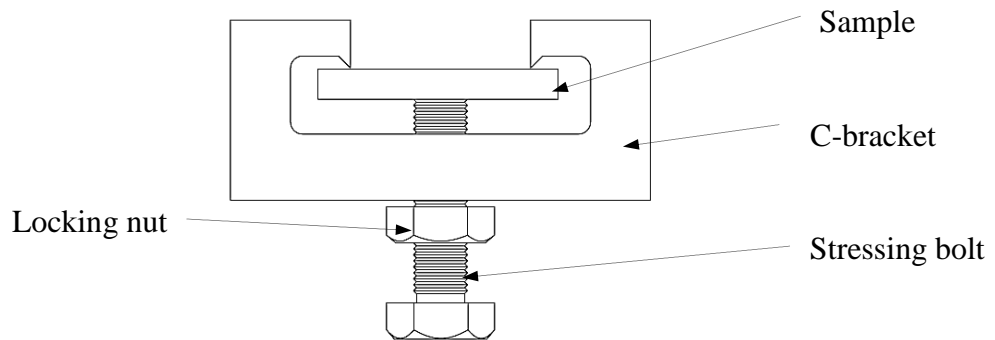
Figure 3.6: Schematic diagram of a three-point bend test rig.

The rig was machined from the same material (304L stainless steel) as the samples to avoid a galvanic corrosion when exposed to corrosive environment in the autoclave. A locking nut was used to hold the sample firmly to the rig and ensure minimal stress relaxation of the sample at high temperatures. The stressed sample was then exposed to a corrosive environment in an autoclave as shown in Figure 3.7.
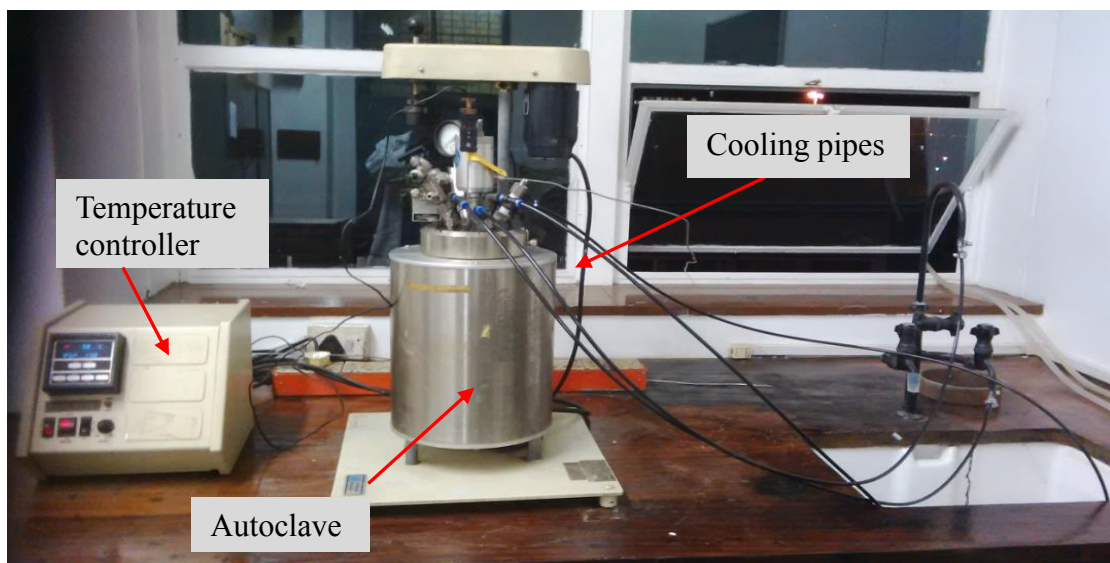
Figure 3.7: SCC Testing setup.

Numerous tests were conducted in different environments to obtain optimum SCC test parameters for this study. As-received 304L stainless steel was used for these tests and an experimental design matrix was drafted as shown in Table 3.1 and Table 3.2. The experimental temperature and time were set at 160°C and 172 hours respectively.

Table 3.1: Effect of chloride concentration on SCC of as-received 304L SS with 10 ppm DO.

Sample	Cl⁻ concentration (ppm)	Crack density (mm⁻¹)	Crack growth rate (x10⁻⁶mm/s)	SCC susceptibility
304L SS Sample 1	10	23	9.1	Low
304L SS Sample 2	50	32	10.2	Medium
304L SS Sample 3	100	41	13.6	Medium
304L SS Sample 4	500	48	14.3	High
304L SS Sample 5	5000	53	19.4	Extreme

At higher chloride concentration, the stress corrosion cracks were wider and propagated faster. The SCC susceptibility was based on the crack growth rate which was compared to that found in literature. However, the second task performed was to look at the effect of DO on the SCC susceptibility of as-received stainless steel. The DO was varied at constant 50 ppm chloride concentration as shown in Table 3.2.

Table 3.2: Effect of DO concentration on SCC of as-received 304L SS.

Sample	DO concentration (ppm)	Crack density (mm⁻¹)	Crack growth rate (x10⁻⁶mm/s)	SCC susceptibility
304L SS Sample 6	0	23	3.45	Low
304L SS Sample 7	2	32	5.31	Medium
304L SS Sample 8	3	41	6.82	Medium
304L SS Sample 9	6	48	9.21	High
304L SS Sample 10	10	53	11.34	Extreme

The selected test parameters were 50 ppm sodium chloride solutions with 10 ppm DO at 160°C and experiment exposure time of 172 hours. This test condition was also used for SSRT and electrochemical tests (section 3.4.2 and 3.4.3).The solution was prepared by dissolving 50 mg of sodium chloride in 1000 ml distilled water and DO content in the autoclave was measured using an M1500K portable dissolved oxygen meter. Thereafter, laser alloyed samples were tested for SCC susceptibility. After running the experiment for 172 hours, the samples were removed and observed under a stereo microscope for pitting and stress corrosion cracks. Further analysis was performed by using an optical microscope and SEM equipped with EDS to identify the mode of cracking, and to determine the chemical composition respectively.

3.4.2 Slow strain rate testing

Understanding SCC using strain rate testing is a vital method to use but certain precautions must be exercised not to set the strain rate too low that the samples fails due to localised cracking or strain rate too high that the samples fail by tensile or brittle failure. Slow strain rate tests (SSRT) were conducted in accordance with ASTM E8 with strain rate at 1×10^{-6} s^{-1}. This test was used to investigate fractography and SCC susceptibility of alloyed (VAR) 304L stainless steel with Ru. The other important feature of using this technique is the possibility to differentiate hydrogen induced cracking and stress corrosion cracking (Kim and Wilde, 1979). The VAR sample shown in Figure 3.8 was machined on a lathe and used for SSRT.
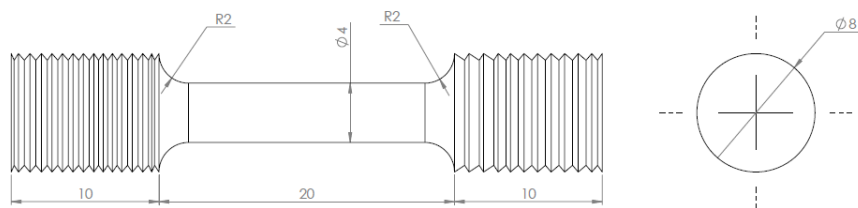
Figure 3.8: SSRT specimen geometry (all dimensions in millimetres).

Figure 3.9 shows the experimental setup where the sample was subjected to tensile stresses in 50 ppm sodium chloride solution and 10 ppm DO at 160°C. An extensometer was attached to the sample to measure the change in length of the sample as it was pulled. The

stress-strain data was acquired using National Instruments DAQ device and recorded using LabView software.
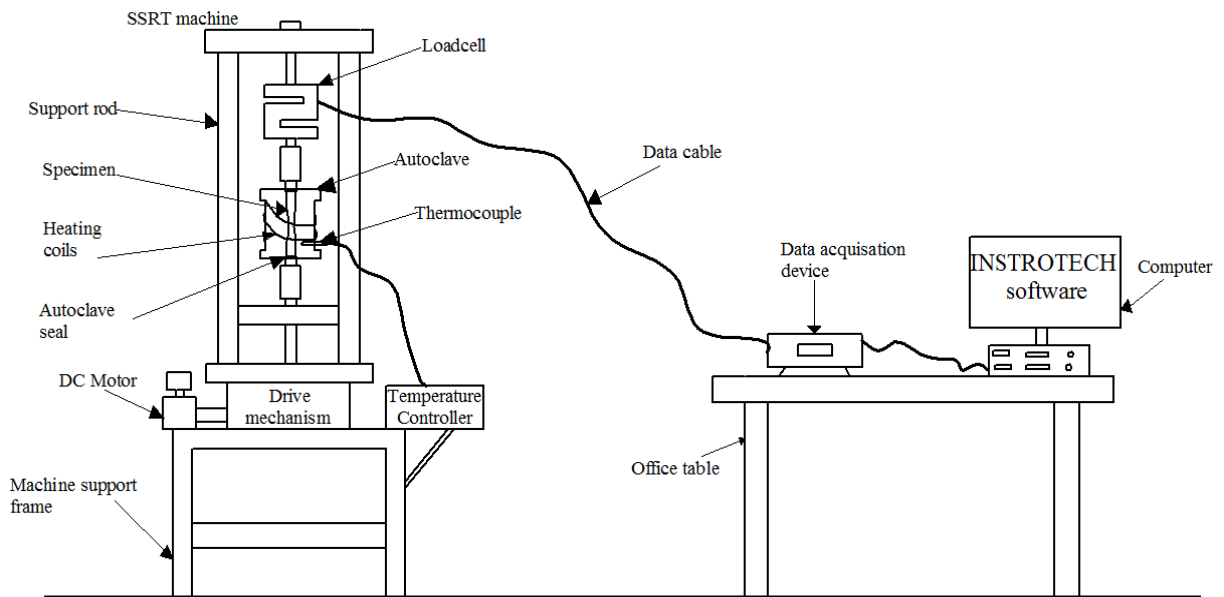
Figure 3.9: SSRT experimental setup.

All galvanic effects were eliminated by ensuring that the specimen had no contact with any metallic components. Fractured samples were examined under SEM. Prior to microscopy examination, the elongation and reduction percentage in area were calculated.

3.4.3 Electrochemical testing

Electrochemical tests were conducted to investigate the corrosion behaviour of laser alloyed layers on 304L stainless steel plate. Samples of approximately 9x4 mm were cut from laser cladded layer and ground up to 1200 grit silicon paper. The sample was then connected to an electrical wire using aluminium tape and insulated with high temperature silicon rubber as shown in Figure 3.10. The sample was inspected for abnormalities and it was ensured that there was no gap between the sample and the silicon rubber. A surface area of approximately 40 mm^2 was exposed to deionised water with 50 ppm sodium chloride solution and 10 ppm DO in an autoclave. Five laser alloyed samples at varying Ru content were tested and compared with as-received 304L stainless steel and VAR samples.
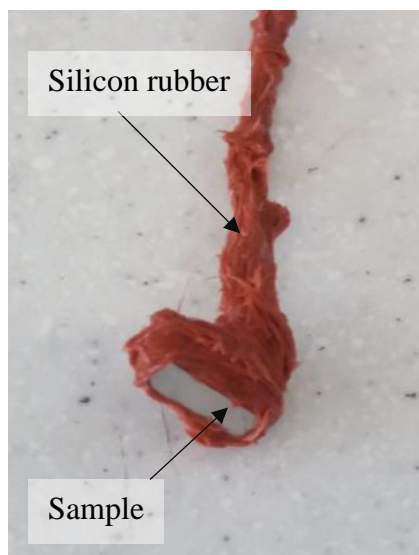
Figure 3.10: High temperature electrochemical test sample.

Since the tests were conducted at high temperatures, 100 and 160°C, it was important to design a reference electrode which would sustain these temperatures. The design of internal reference electrode was achieved by first cleaning a silver wire (0.5 mm diameter) with acetone to remove any grease. The silver wire was then connected to the anode (working electrode) and Pt wire was connected to cathode (counter electrode) and a commercial Ag/AgCl electrode was used as reference electrode. The current was allowed to pass through the working silver electrode at 3 mV over surface area of 45 mm^2 for 45 minutes in 1% NaCl solution. The colour of the silver wire changed to grey-purple, this showed the presence of deposited chloride on the Ag wire. For every new test, the Ag/AgCl electrode was cleaned by reversing the electrolysis process to remove any residual AgCl that might be left by pits. And finally ground with 1200 grit silicon paper and rinsed in ethanol. The deposition of AgCl on the silver wire was repeated.

The electrochemical tests were carried out after chloriding the silver wire and allowing it to stabilise in 1M HCl solutions for 10 hours. The sample was placed in an autoclave for electrochemical measurements. All electrical contacts which could affect the accuracy of the results were insulated with high temperature silicon rubber. A reference and counter electrodes were connected to conax glands on the autoclave lid connecting the chlorided Ag and Pt wires respectively. The working electrode was connected to the sample exposed to an electrolyte as shown in Figure 3.11.
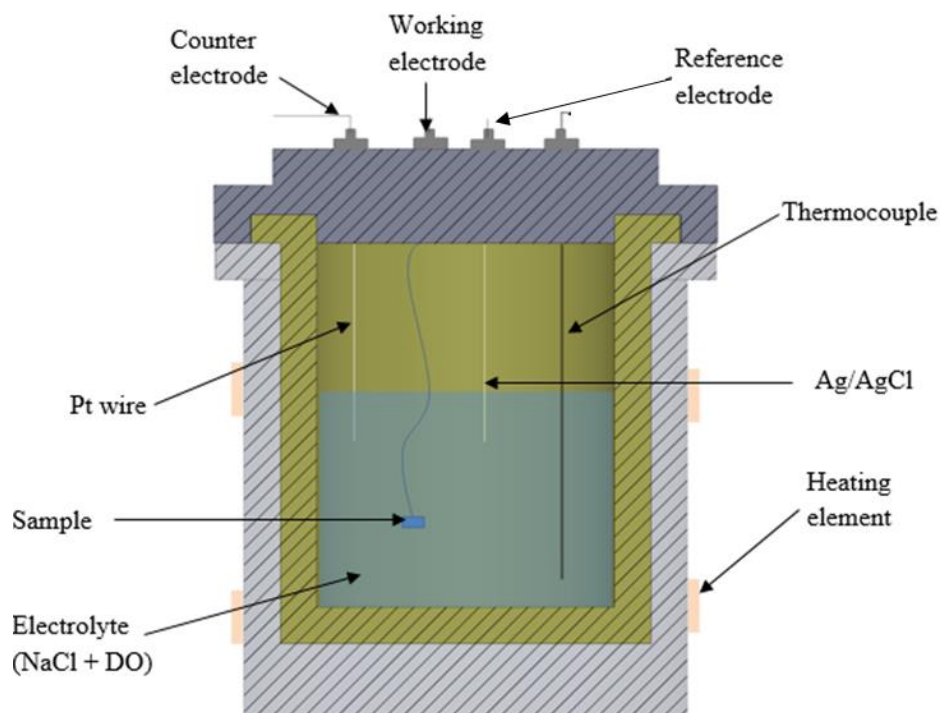
Figure 3.11: Schematic diagram of electrochemical electrodes and the sample in an autoclave.

The overall experimental setup shown in Figure 3.12 was achieved by connecting the Autolab potentiostat (PGSTAT20) incorporated with Electrochemical Software NOVA version 1.11 to the computer and the electrodes. The electrodes were connected to an autoclave.
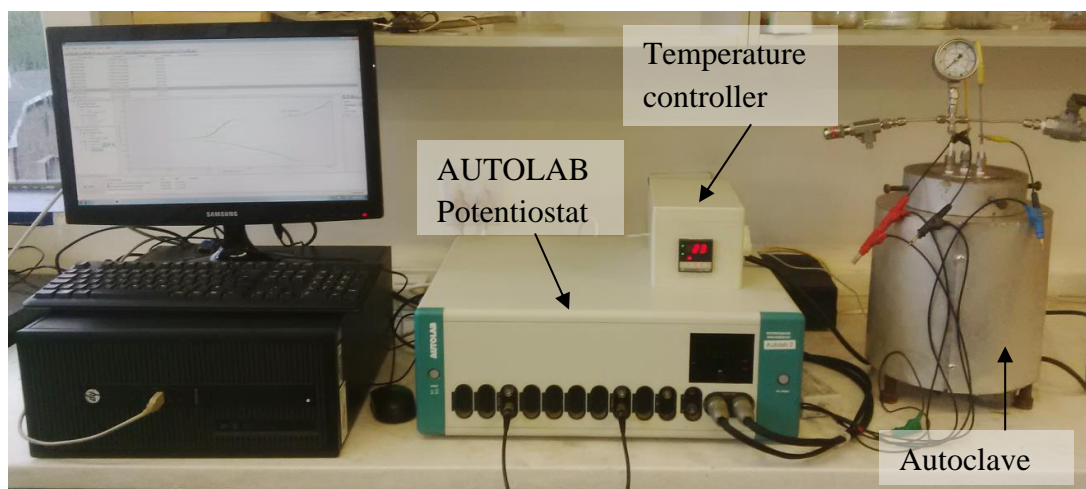
Figure 3.12. Electrochemical test setup.

The Nova software was used to define the test procedure, set experimental parameters and plot potentiodynamic polarisation curves. Each sample was tested separately and a fresh test solution was used. The polarisation procedure to determine OCP was performed at a scan rate of 0.2 mV/s as follows:

- Polarisation at -1 V for 5 minutes followed by a scan from -400 mV to 800 mV
- OCP for 12 hours and thereafter a scan from -600 mV to 800 mV.
- Polarisation at -1V for 5 minutes and a scan from -400 mV to 800 mV.

The procedure was performed at 25°C and 160°C for all of the samples. The potentiodynamic polarisation was performed at scanning rate of 0.2 mV/s. The LSA and VAR samples were then tested at 25°C, 100°C and 160°C and the potentiodynamic polarisation data was recorded.

CHAPTER 4

RESULTS

4.1 Microstructural observations

The alloys investigated in this study were evaluated to determine microstructural features such as crystal structure, size, formation, voids and composition which can have an effect on the hardness, strength and corrosion resistance. The microstructural examination was performed for as-received 304L stainless steel (SS), Ru alloyed 304L stainless steel samples produced using LSA and VAR techniques.

4.1.1   Microstructure of as-received 304L SS

The as-received 304L SS was metallographically prepared as outlined in Section 3.1.3 and characterised by using an optical microscope and SEM. The elemental composition (see Appendix B) correlated with the steel manufacture's specification (Outokumbu, 2015). As shown in Figure 4.1, an equiaxed grain structure was observed on the cross-section of as-received 304L stainless steel.
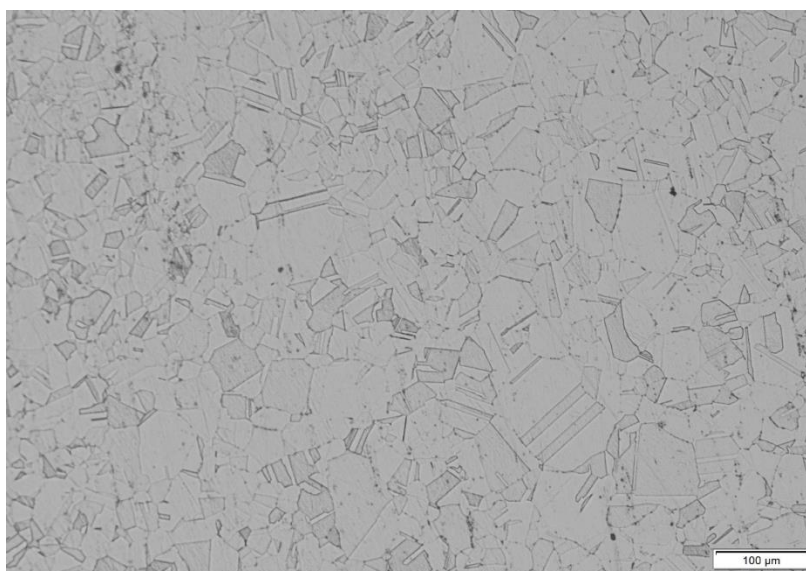
Figure 4.1: Microstructure of the as-received 304L SS etched electrochemically with 10% oxalic acid at 8 V for 60 seconds.

The equiaxial austenite grains with annealed twins were in agreement to those reported in literature (Sun et al., 2014; Young et al., 2009). There was no evidence of defects, inclusions and precipitates. The microstructure was free from chromium carbides which usually form along the austenite grain boundaries.

4.1.2 Microstructure of laser alloyed 304L SS with Ru

It has been reported (Kwok, 2010; Yao et al., 2008; Tjong et al., 1996) that laser surface alloying plays a significant role in altering the microstructure of materials. In this study the microstructure of the cross-section of laser alloyed 304L stainless steel consisted of the alloyed layer, transition zone, HAZ and base metal as shown in Figure 4.2.
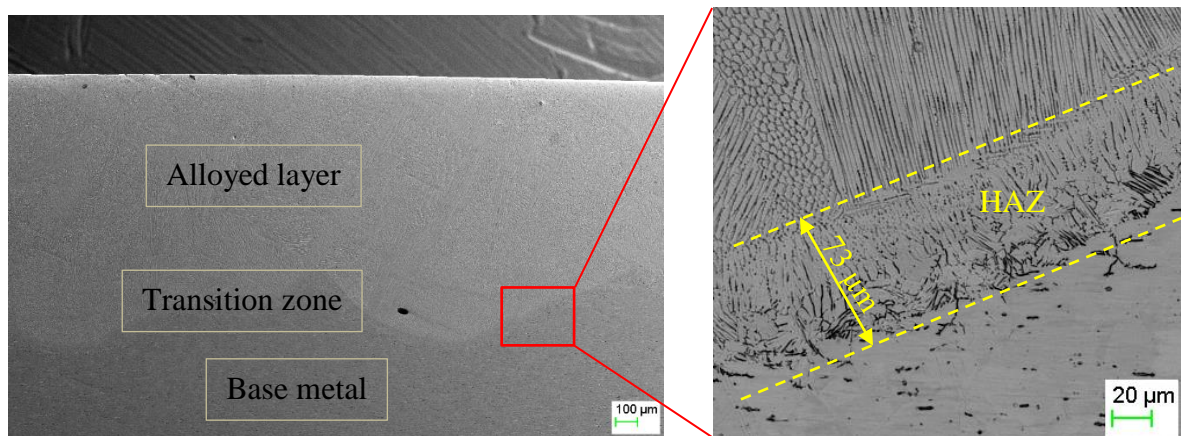
Figure 4.2: Microstructure of laser alloyed 304L stainless steel with 0 wt% Ru etched with marble's reagent and 10% oxalic acid.

The transition of fine grains to coarse was observed on the HAZ. All samples (0, 0.98, 1.96, 4.74 and 9.2 wt% Ru) had refined microstructure of the alloyed zone. The samples were free from flaws and showed a complete metallurgical bond between the alloyed layer and the base material. Even at higher magnification (5000X) no detachment or defects were found. There was no significant increase in thickness of the alloyed layer when the Ru content was increased. The averaged thickness of laser alloyed layer was approximately 850 μm as shown in Figure 4.3.
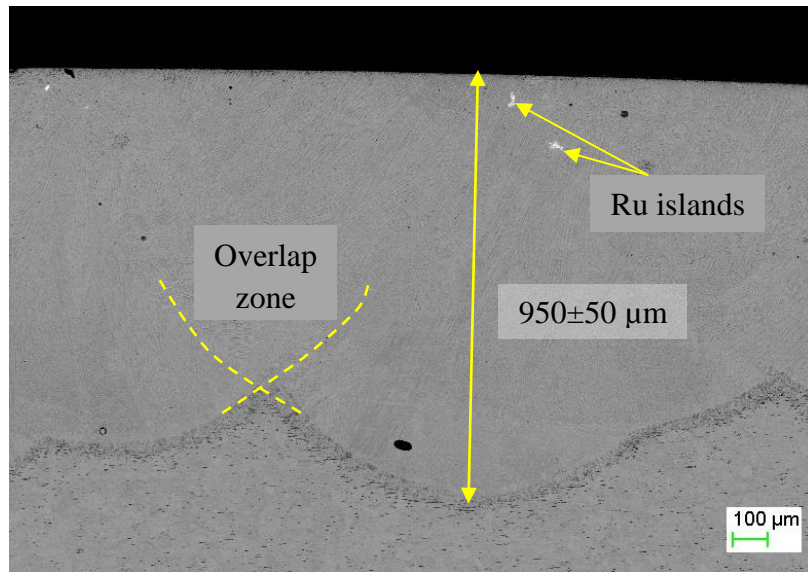
Figure 4.3: Cross-section of laser alloyed 304L stainless steel with 4.74 wt% Ru etched with marble's reagent and 10% oxalic acid.

The overlap zone was formed by successive weld beads which were approximately 0.8 mm centre to centre apart. These zones were free from voids. As shown in Figure 4.4 it can be argued that the microstructure of these zones was coarser when compared to the alloyed layer. The overlap (coarser grains) could be associated with exposure to high temperatures during LSA process.
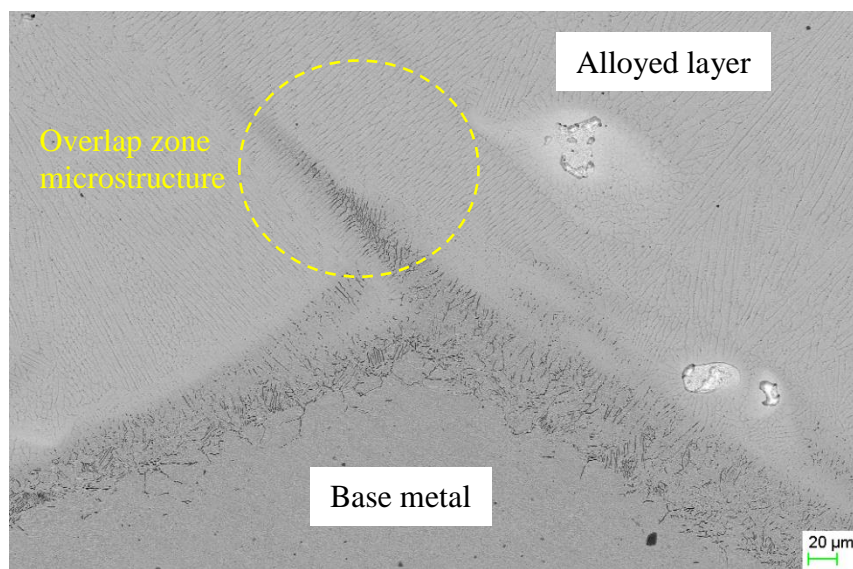
Figure 4.4: Microstructure of overlap zone of laser alloyed 304L stainless steel with 9.2 wt% Ru and etched with marble's reagent and 10% oxalic acid.

It was evident from chemical composition analysis that Ru was homogenously distributed at lower Ru contents (0, 0.98 and 1.96, 4.74). At higher Ru contents (4.74 and 9.2 wt%) there were islands of undissolved Ru as shown in Figure 4.5. Indicating that even at the high cooling rates complete solubility of Ru was not achieved.
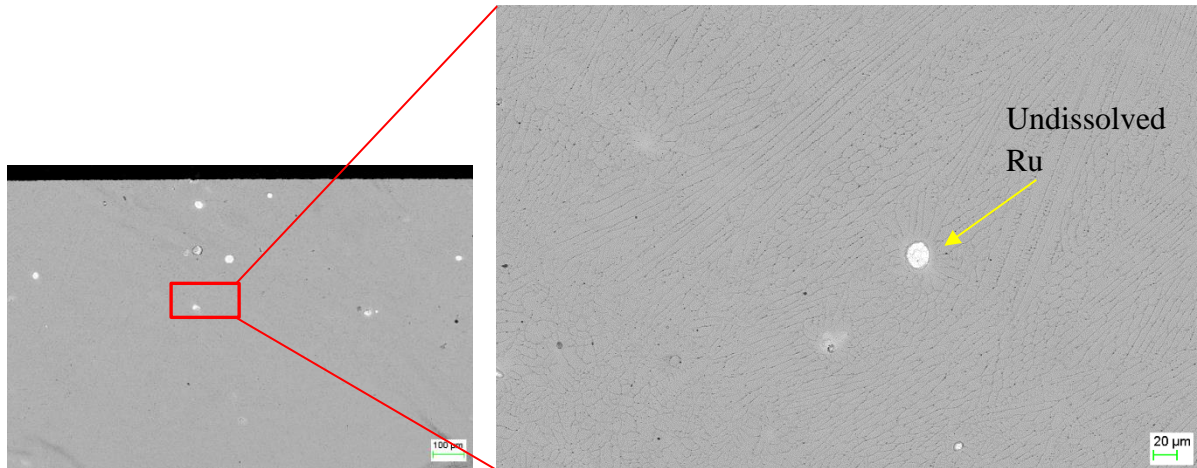
Figure 4.5: Ru islands formed on 304L SS laser alloyed layer with 9.2 wt% Ru.

The undissolved Ru islands were approximately 18 µm in diameter. These islands had a unique microstructure around them. The undissolved Ru could be attributed to laser power and the scanning speed not being enough to melt all of the Ru powder. However, a peculiar microstructural features were also observed on the alloyed layer towards the top surface of the samples as shown in Figure 4.6. These regions showed a very fine grain structure.
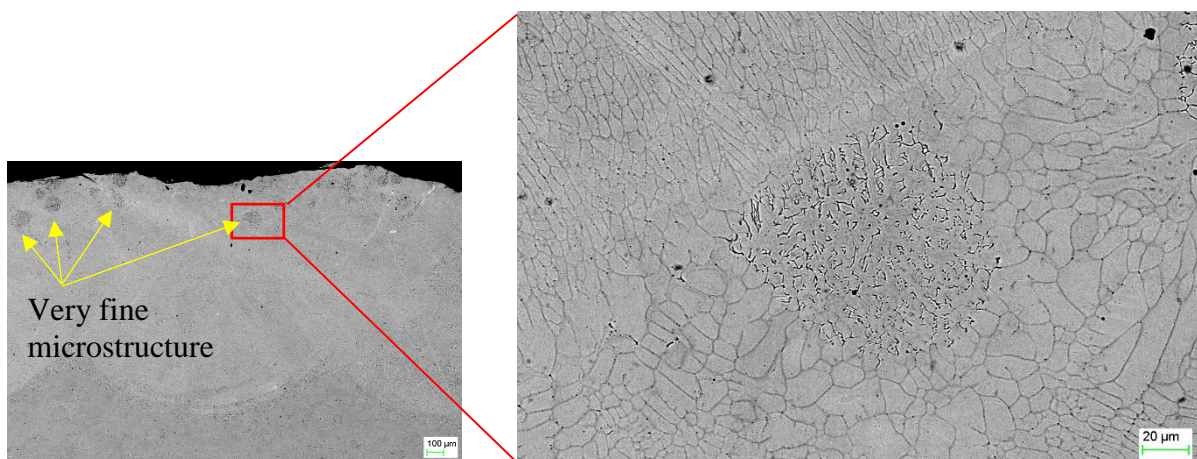
Figure 4.6: A very fine grained regions towards the top surface of laser surface alloyed 304L SS with 0.98 wt% Ru and etched with marble's reagent and 10% oxalic acid.

The elemental composition of this fine grained structure consists of other elements and Ru was not present. It consisted of 0.84% Si, 19.13% Cr, 1.89% Mn, 10.49% Ni and 67.66% Fe as shown in Figure 4.7. These islands of fine grains were observed in all LSA samples.
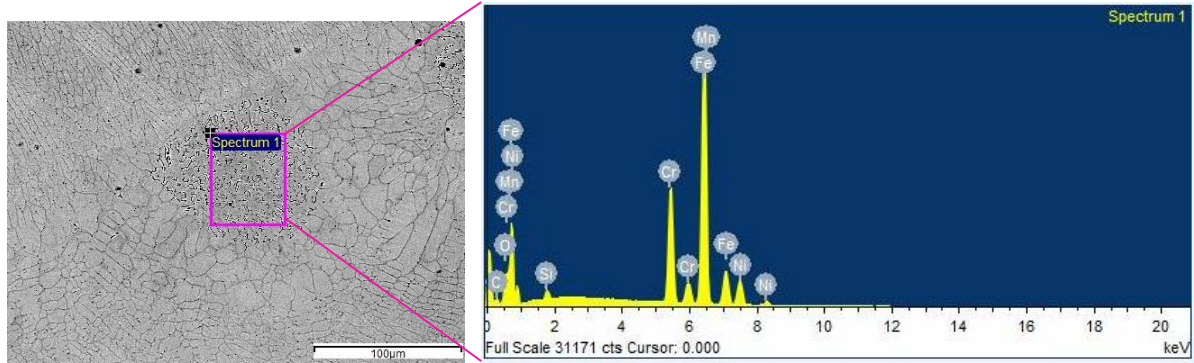
Figure 4.7: EDS analysis of very fine grained structure of laser alloyed 304L SS with 0.98 wt% Ru showing higher content of nickel and chromium.

4.1.3   Microstructure of VAR 304L SS with Ru

The microstructure and elemental composition of vacuum remelted samples was analysed using an optical microscope and EDS respectively. The EDS results (Appendix B) showed higher Ru level than what was expected for all the samples. Figure 4.8 to Figure 4.12 shows cross-sectional microstructures of vacuum remelted samples at varying Ru contents (0, 1.07, 2.05, 6.07 and 12.34 wt%). The microstructural investigation was performed longitudinal to rolling direction on the cross-section.
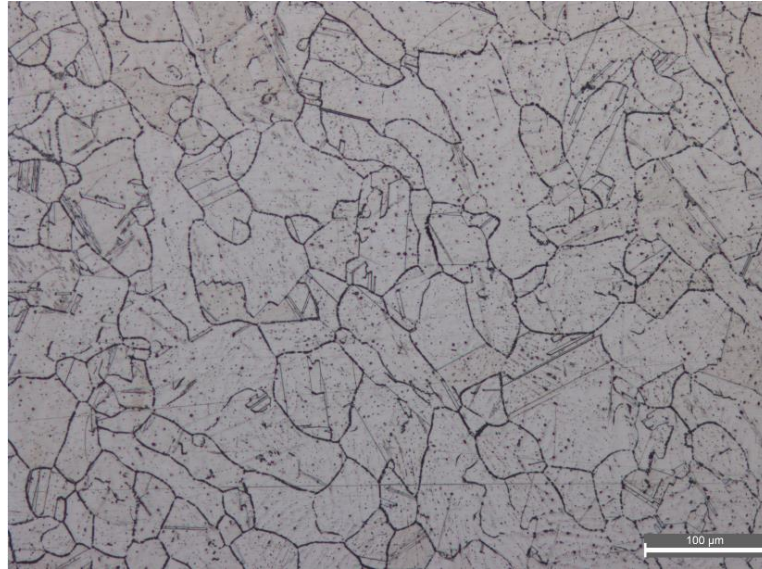
Figure 4.8: Microstructure of VAR 304L SS with 0 wt % Ru and electrochemically etched with 10% oxalic acid at 8 V for 90 seconds.
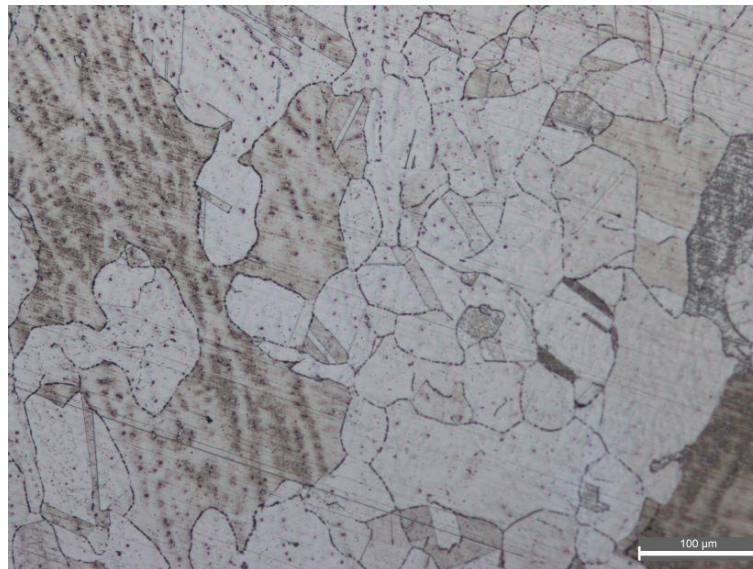
Figure 4.9: Microstructure of VAR 304L SS with 1.07 wt % Ru and electrochemically etched with 10% oxalic acid at 8 V for 90 seconds.
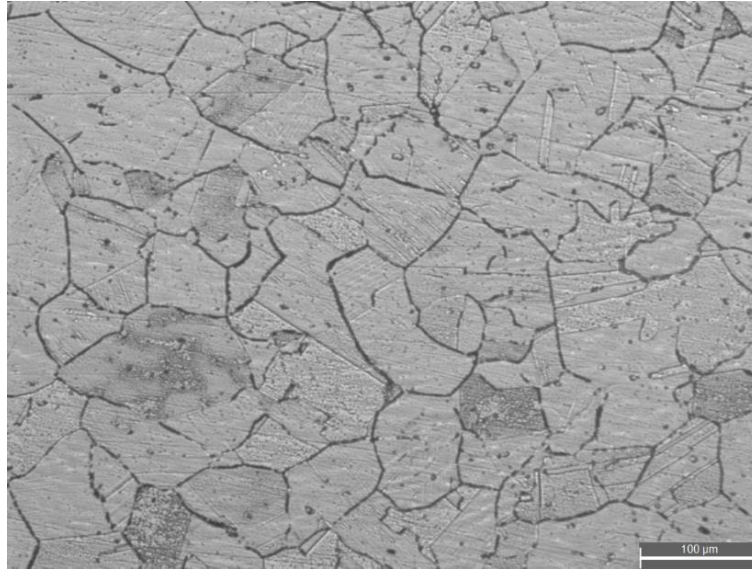
Figure 4.10: Microstructure of VAR 304L SS with 2.05 wt % Ru and electrochemically etched with 10% oxalic acid at 8 V for 90 seconds.
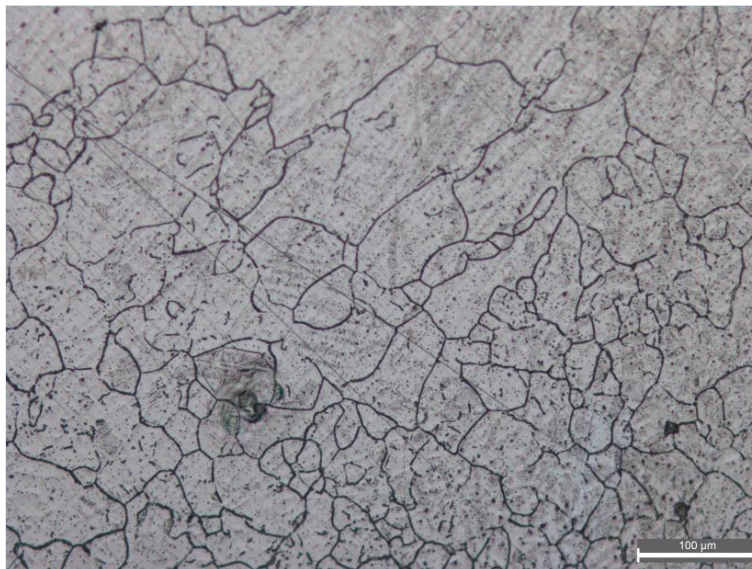
Figure 4.11: Microstructure of VAR 304L SS with 6.07 wt % Ru and electrochemically etched with 10% oxalic acid at 8 V for 90 seconds.
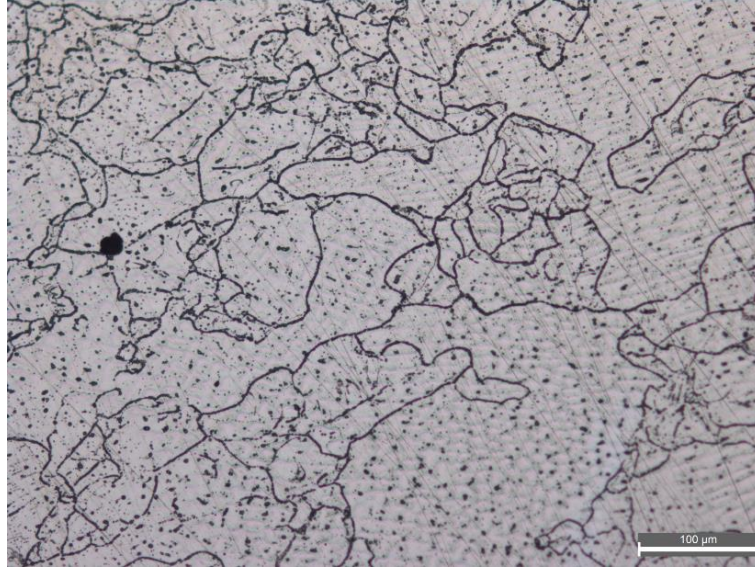
Figure 4.12: Microstructure of VAR 304L SS with 12.34 wt % Ru and electrochemically etched with 10% oxalic acid at 8 V for 90 seconds.

4.1.4 Effect of Ru on the grain size

In general, grain refinement affects mechanical properties such as ductility, yield strength (Hall-Perth equation) and hardness. Grain refinement can be achieved by change in plastic deformation, solidification rate and other thermomechanical processing routes. Previous studies (Calcagnotto et al., 2009; Morris, 2001) has reported improvement of tensile and yield strength of steels when the grains were refined, but the total deformation was hardly affected. In this study the grain size number was determined according to ASTM E112-12 intercept method. The effect of Ru on the grain size of the LSA and VAR samples was evaluated.

The LSA samples consisted of refined grains structure which was geometrically similar and the mean grain size number was approximately 10.5. An increase in grain size number was observed as the Ru content was increased to 4.76 wt% as shown in Figure 4.13. In order to improve the accuracy of the calculated grain size number, three regions of the laser alloyed microstructure was analysed and the average grain size number was obtained (Table B5). The grain size number on the HAZ for all samples was consistent around 10.3.
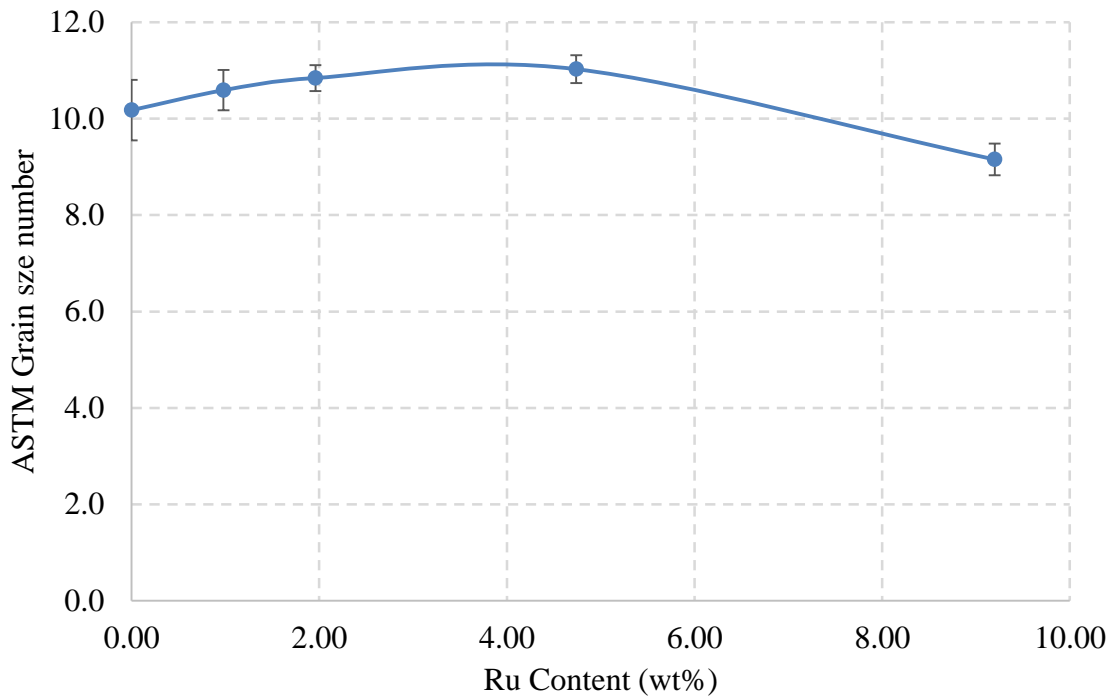
Figure 4.13: Relationship of grain size number and Ru additions on 304L stainless steel samples prepared using LSA technique.

The LSA samples with 9.2 wt % Ru had the lowest grain size number of 9.46. This was not in agreement with the work reported by Hills et al. (1965) where the grain size number reduced when the Ru content was increased on heat treated uranium-ruthenium alloys. They reported the inconsistency of grain size on samples with lower Ru content (0.25 wt%). The inconsistency of grain size could be attributed to the phase transformation before reaching the isothermal temperature (Hills et al., 1965). For a different system Shing et al. (2001) observed an increase in grain size as the Ru content was increased for WC-Co alloys. However, the Ru additions of more than 10 wt% Ru inhibited the growth of fine grains.

Further analysis of the effect of Ru on the grain size was performed on vacuum remelted samples. It was observed that the grain size number increased as Ru addition was increased. The samples with 12.34 wt% Ru behaved differently as there was a substantial fall in grain size number of 3.3 as shown in Figure 4.14, because of the difference in cooling rates.
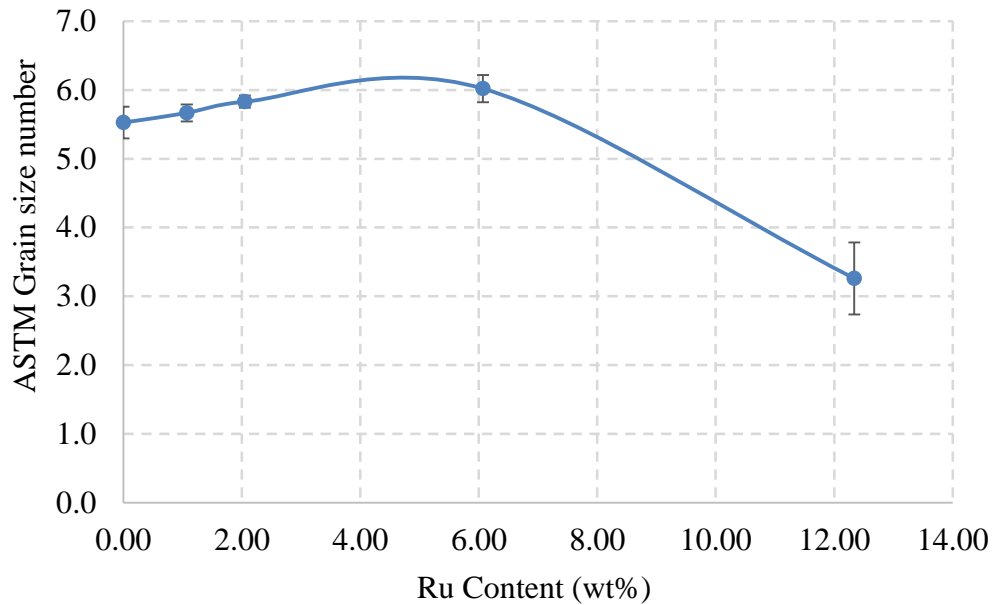
Figure 4.14: Relationship of grain size number and Ru additions on 304L stainless steel samples prepared using VAR technique.

The difference in grain size number of the two techniques (LAA and VAR) could be attributed to the refined microstructure of LSA samples. However, the relationship of the grain size and SCC of laser alloyed 304L SS is discussed in Chapter 5.

4.2 Microhardness measurements

The mechanical properties of materials are often defined by tensile and hardness tests. In this study, only the hardness of LSA and VAR samples could be investigated because of the sample size. The measurements were conducted along the cross-section of the samples using Vickers hardness tester at 500 gf. As shown in Figure 4.15 the alloyed layers had a higher hardness than the substrate. The hardness of the alloyed layer consistently increased with increasing Ru content.
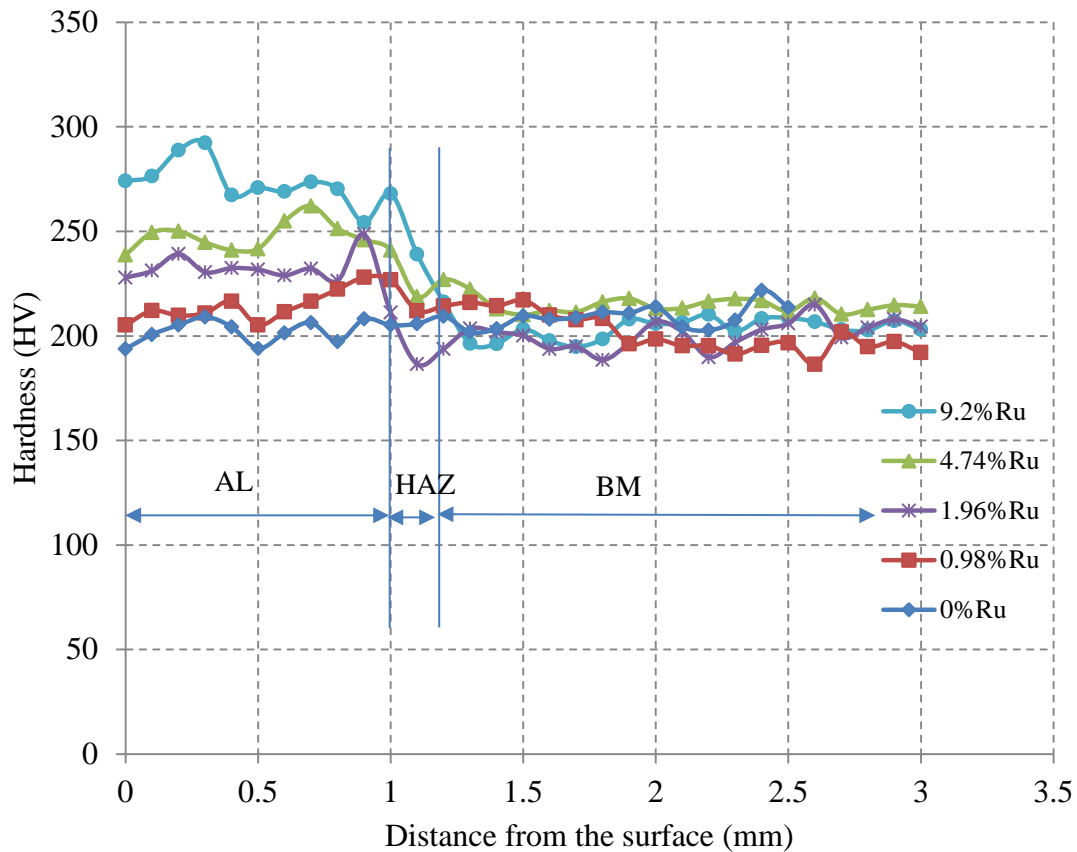
Figure 4.15: Vickers hardness profile of laser surface alloyed 304L stainless steel with Ru.

The higher hardness obtained was at a thickness of 200 μm from the surface. This correlated to the work conducted by Yao et al. (2008) on laser surface alloyed 17-4PH stainless steels. There was a significant peak within this thickness for all treated samples. After this peak, the hardness gradually decreased to approximately 210 HV. In this study, the peaks in the alloyed layer were consistent with literature (Brytan et al., 2010; Yao et al., 2008; Tian et al., 2005; Tjong et al., 1996). These peaks could be attributed to different solidification rate, refined microstructure and the strengthening of the material hall-petch (Dieter, 1961). The hardness of the refined microstructure (alloyed layer) was higher than the coarser microstructure in the overlap zone. The hardness in the overlap zone was approximately 220 ± 10 HV.

The samples with 0.98, 1.96, 4.74 and 9.2 wt% Ru showed a significant increase in hardness (about 40%) when compared to as-received 304L stainless steel. A comparison of LSA samples with VAR samples showed higher hardness values of the laser alloyed layer as

shown in Figure 4.16. It should be noted here that the hardness of LSA samples was calculated by averaging the hardness values of the alloyed layer.
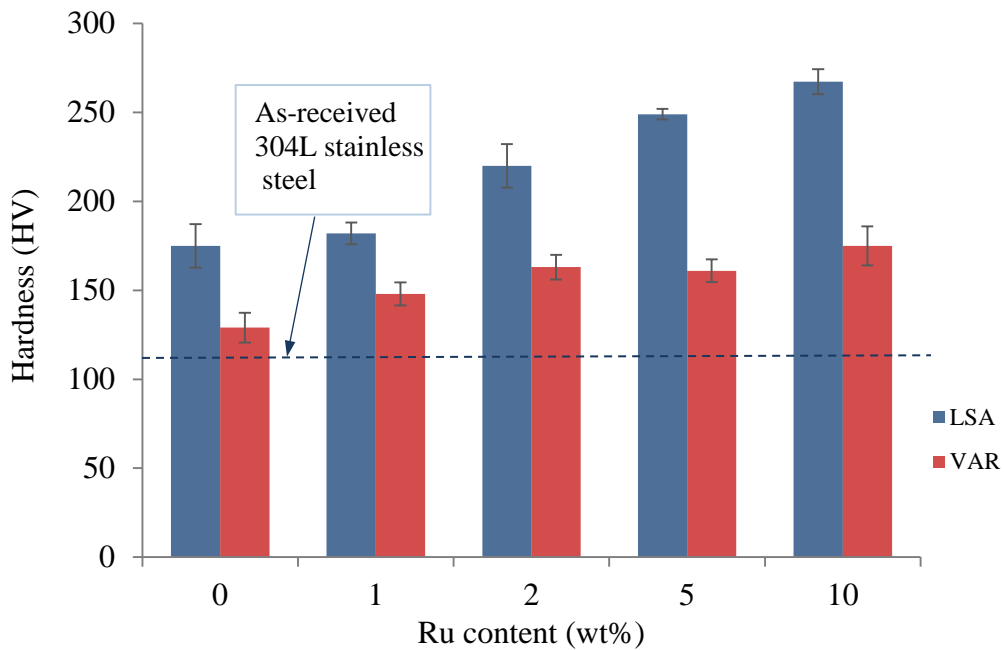
Figure 4.16: Comparison of Vickers microhardness values of alloyed 304L stainless steel with Ru.

It is evident that laser alloyed samples had higher hardness than the VAR sample because of higher cooling rates introduced during the laser alloying process. The higher hardness in LSA samples could also be linked to refined grains of the alloyed laser. The benefit of refined grains in alloys can lead to improved SCC resistance because of phase precipitates which can reduce alloy resistance to pitting, crack initiation and hydrogen absorption (Puiggali et al., 1998). In this study, the grain size number increased as the Ru level was increased up to 2 wt%, which was associated with a more refined microstructure. The refined microstructure played a role in hardness as the hardness. An increase in hardness of laser alloyed layers lead to improved SCC resistance.

4.3 Environmentally assisted cracking of tested alloys

As part of the objectives of this study, the experiments were conducted to investigate the susceptibility of alloys to EAC especially stress corrosion cracking (SCC). A three-point bend and SSRT tests were employed. The samples were exposed to a corrosive environment for seven days and thereafter the crack nucleation and propagation were evaluated.

4.3.1   Effect of environment on SCC

A series of tests was conducted at various environments to evaluate the effect of Cl⁻ concentration, dissolved oxygen and temperature on SCC susceptibility of as-received 304L stainless steel prior to using Ru alloyed samples. The environmental factor which mostly influenced SCC susceptibility of the samples was the chloride concentration. Further analysis of experimental parameters is stated in Appendix D.

The evidence of pitting was evaluated with a stereo microscope immediately after the samples were removed from the autoclave (corrosive environment). At very high chloride concentrations (5000 ppm) and temperature (160°C), the SCC cracks were wider and propagated from a region of high tensile stress (top surface) to a region of low tensile stresses (bottom surface). The cracks initiated from a pit and propagated transgranularly as shown in Figure 4.17. These pits were also observed on the top surface of the sample, but they were covered with corrosion product.
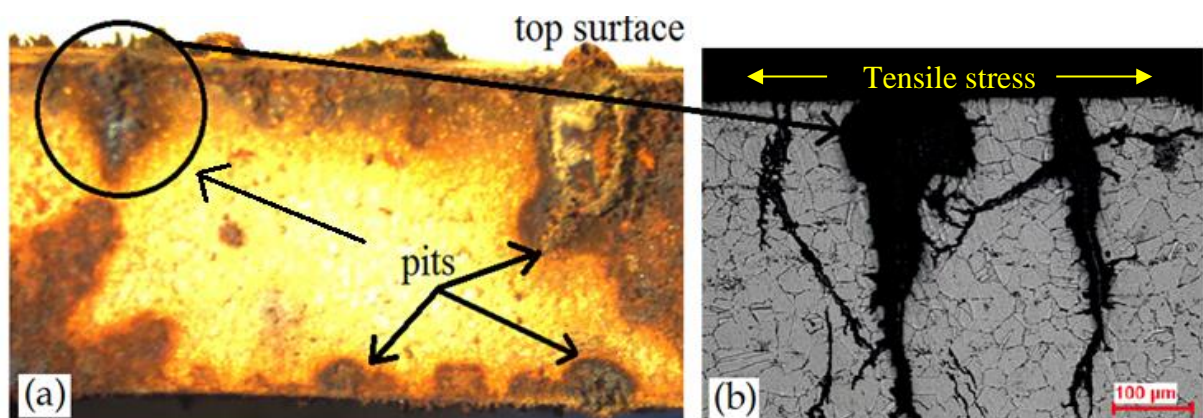
Figure 4.17: SCC cracks initiated from pits of untreated 304L stainless steel exposed in 5000 ppm NaCl solution at 160°C for 172 hours; (a) before etching (b) after etching.

It was difficult to predict the time at which the cracks initiated, but it was evident that the cracks initiated from various corrosion pits. At the tip of the crack, dissolution took place with the combination of tensile stress to break the passivation layer leading to chloride ions attacking the freshly exposed metal. This argument can be related to slip step crack mechanism which was explained by Juang and Altstetter (2012). But some cracks investigated in this study did not follow this type of mechanism. The cracks were wider (50 μm) and propagated at an acute angle (approximately 45˚) to tensile stresses direction in a transgranular manner.

An increase in chloride concentration showed an increase in the number of cracks on the cross-section of the samples as shown in Figure 4.18. This was expected since the chloride concentration influenced the initiation of pits which acted as stress raisers to initiate a crack.
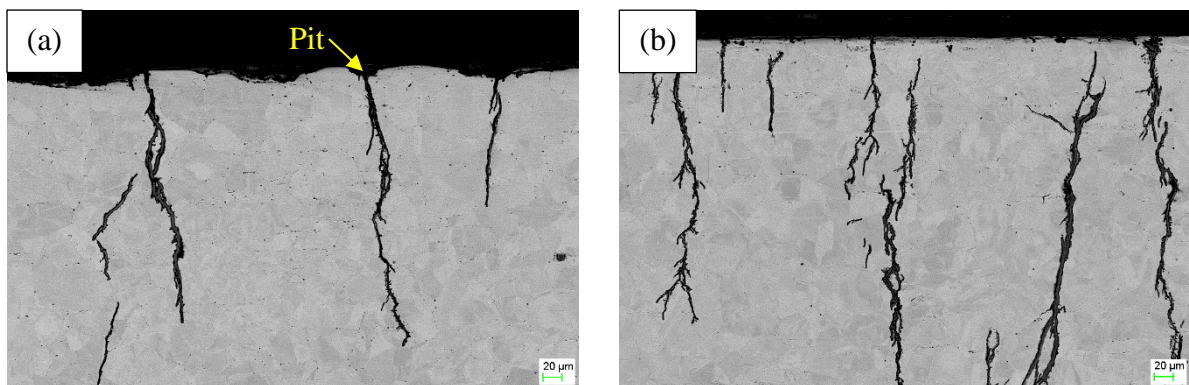
Figure 4.18: Transgranular SCC of as-received 304L stainless steel exposed to NaCl solution containing 3 ppm DO at 160°C for 172 hours; (a) 100 ppm Cl⁻ concentration (b) 500 ppm Cl⁻ concentration.

Although the quantitative analysis of pit formation was not performed, it was evident that the number of pits on the surface increased with increasing chloride concentration. The addition of DO contributed to the severity of SCC. The as-received 304L stainless steel was less susceptible to SCC in oxygen free solution (i.e purged with nitrogen) as shown in Figure 4.19. The cracks were faint and initiated in a region of high tensile stresses. But as the DO was increased from 0 to 10 ppm, the cracks coalesced and propagated across the grains in a transgranular manner (Figure 4.19).
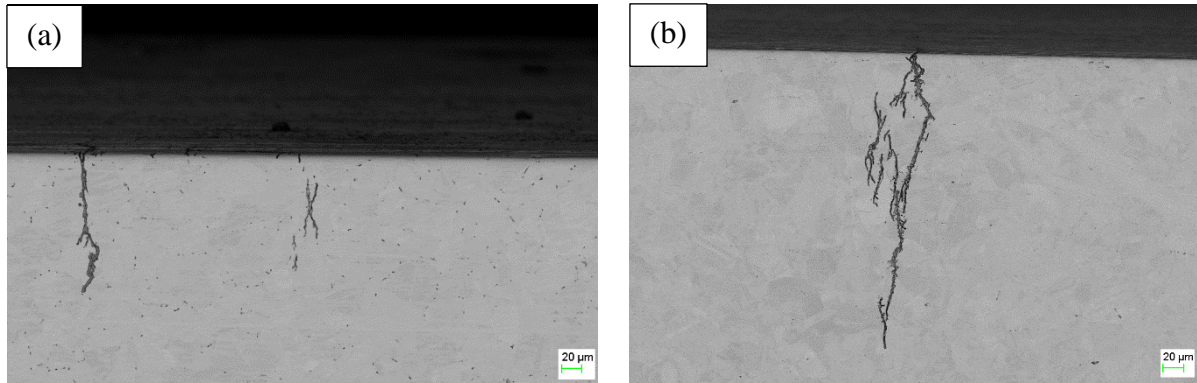
Figure 4.19:Transgranular SCC of as-received 304L SS after exposure to 10 ppm NaCl solution at 200˚C for 172 hours (a) 0 ppm DO (b) 10 ppm DO.

Another parameter which was optimised was the temperature. The effect of temperature on the SCC susceptibility of as-received 304L stainless steel in 50 ppm NaCl solution containing 10 ppm DO was evaluated. As shown in Figure 4.20 the cracks grew faster and longer when the temperature was increased from 80°C to 160°C.
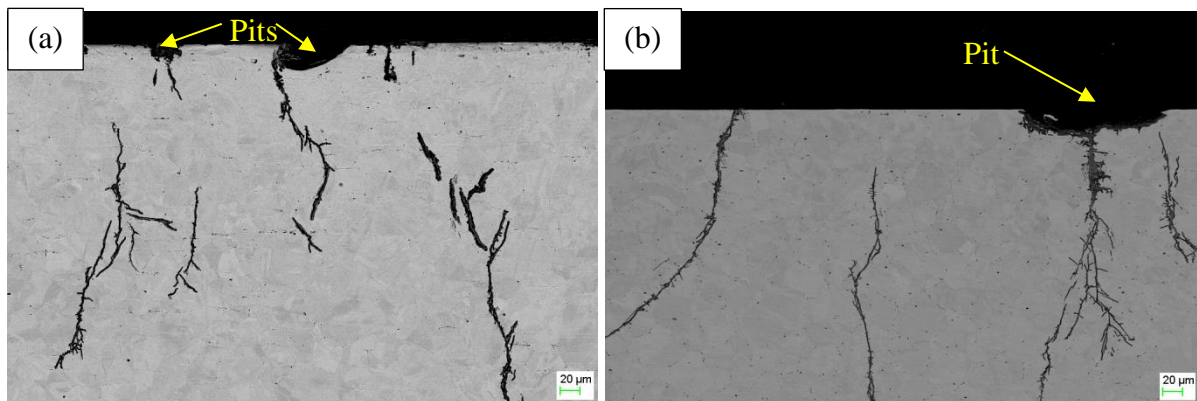
Figure 4.20: Transgranular SCC of as-received 304L SS after exposure to 50 ppm NaCl solution and 10 ppm DO for 172 hours (a) 80˚C (b) 160˚C.

As the pits became larger, the nucleation of a crack was formed at the base of the pit where the presence of tensile stresses allowed the crack to propagate. It was found that the main contributor to SCC initiation was a pit on the surface which broke the oxide film and exposing fresh layer to solution attack. The formation of a pit on the surface will occur due to chemical reaction at interface of the solution and the metal. A complete circuit is completed when the electrons are released from the anode to cathode to form brown rust (corrosion product) as shown in Figure 4.17. The oxygen content reduces as the pit becomes deeper.

4.3.2 SCC of laser alloyed 304L SS

The SCC tests revealed some of the samples to have cracks on the top surface of laser alloyed layer as well as on the cross-section as show in Figure 4.21.
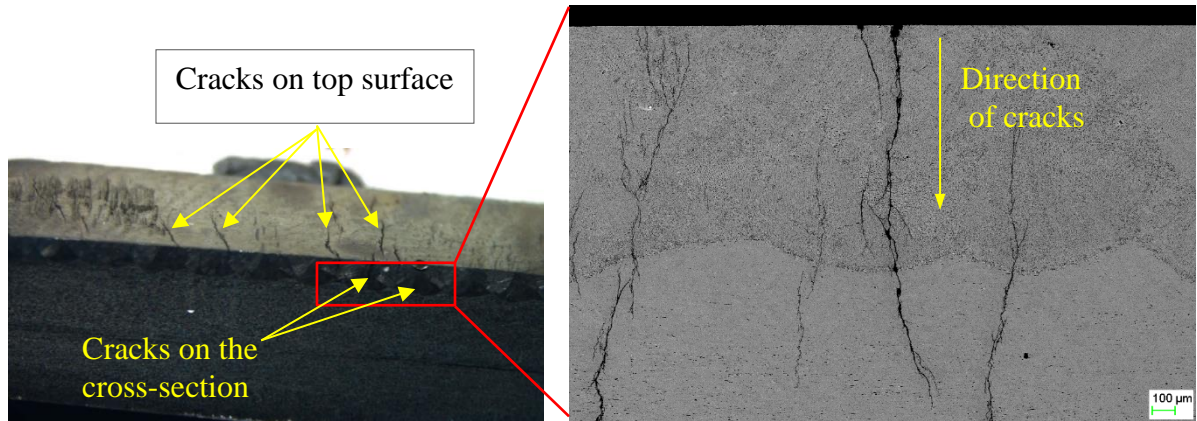
Figure 4.21: SCC cracks on the cross-section of laser alloyed 304L SS with 0 wt% Ru after exposure to 50 ppm NaCl containing 10 ppm DO at 160˚C for 172 hours.

The cracks (Figure 4.21) initiated from a region of high tensile stresses and propagated through the alloyed layer to the base metal. Most of the cracks did not branch as expected but rather coalesced and propagated at right angle to tensile stress in a transgranular manner. However, as the Ru content was increased the SCC cracks on the cross-section of the laser alloyed layer propagated at approximately 45˚ to the tensile stress as shown in Figure 4.22 and Figure 4.23.
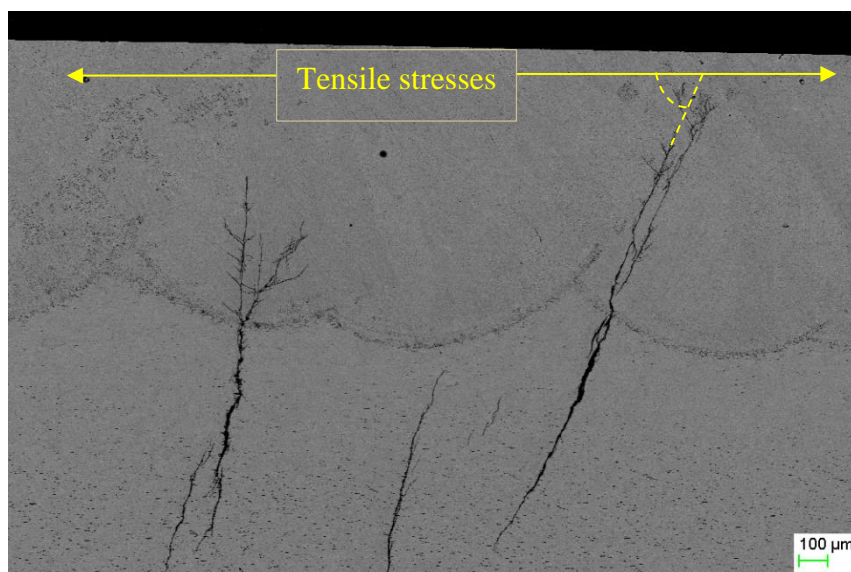
Figure 4.22: Transgranular SCC of laser alloyed 304L SS with 0.98 wt% Ru after exposure to 50 ppm NaCl containing 10 ppm DO at 160˚C for 172 hours.
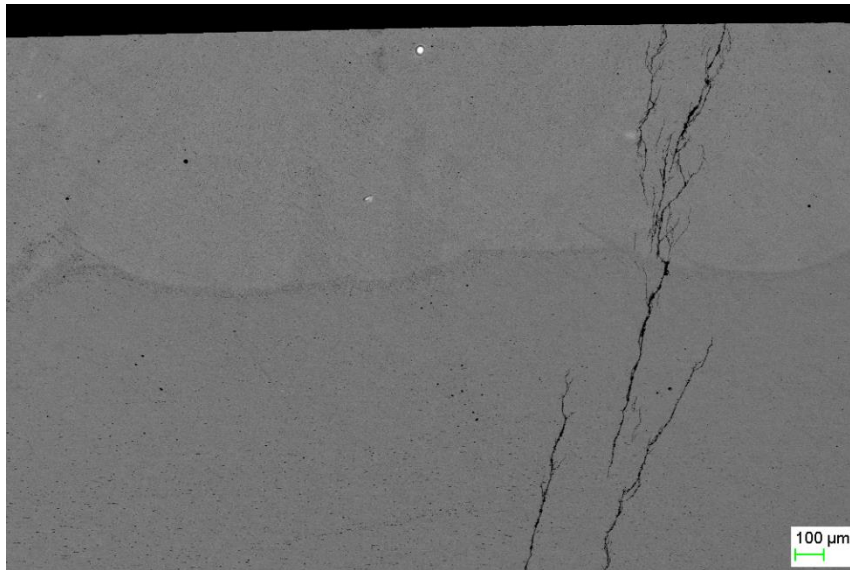
Figure 4.23: Transgranular SCC of laser alloyed 304L SS with 1.96 wt% Ru after exposure to 50 ppm NaCl containing 10 ppm DO at 160˚C for 172 hours.

At high Ru levels (4.74 and 9.2 wt%) there was no evidence of SCC cracks after exposure to 50 ppm NaCl containing 10 ppm DO at 160˚C for 172 hours. The repeatability of results was conducted and the samples were not susceptible to SCC as shown in Figure 4.24 and Figure 4.25.
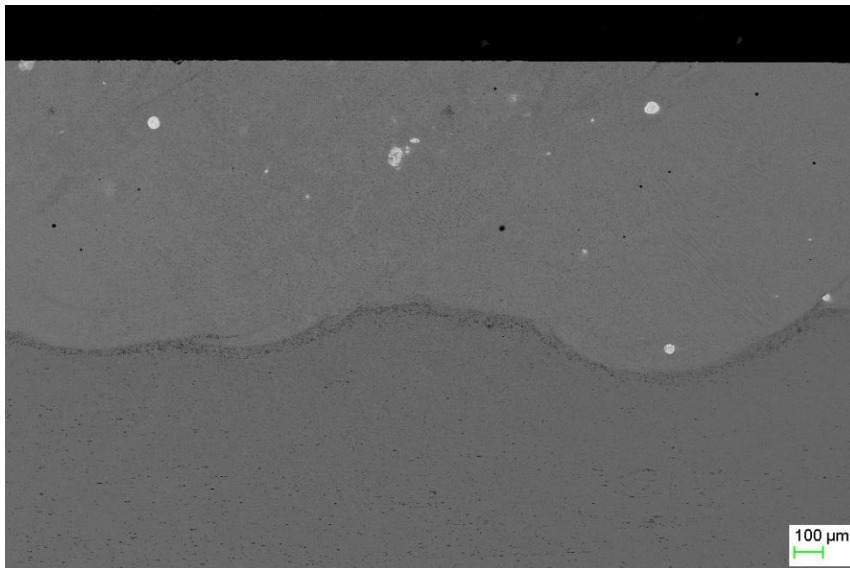
Figure 4.24: Cross-section of laser alloyed 304L SS with 4.74 wt% Ru after exposure to 50 ppm NaCl containing 10 ppm DO at 160˚C for 172 hours.
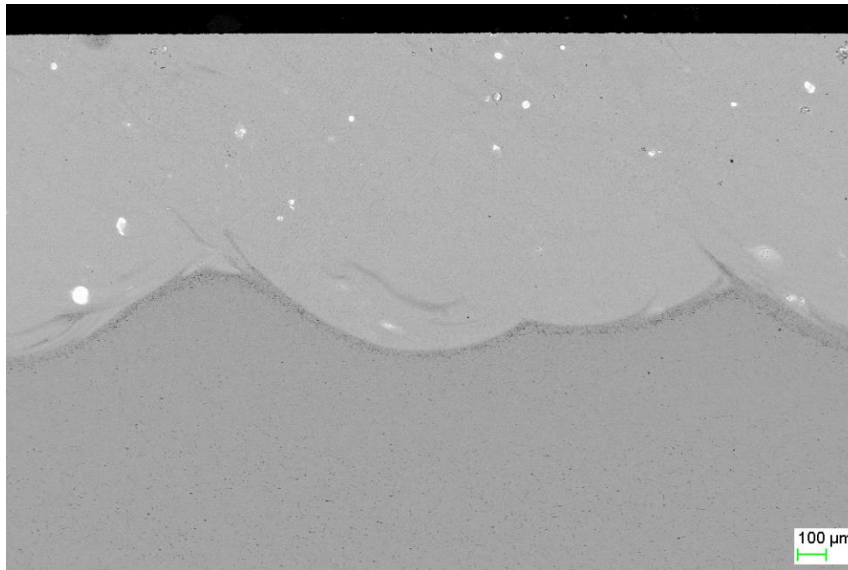
Figure 4.25: Cross-section of laser alloyed 304L SS with 9.2wt% Ru after exposure to 50 ppm NaCl containing 10 ppm DO at 160˚C for 172 hours.

4.3.3 Crack density and growth rate

The micrographs of the deepest cracks were mapped and the crack total length and depth were measured as shown in Figure 4.26. The total length of the longest crack was obtained by adding small lengths ($l_1, l_2, l_3....$). Although some the cracks were only visible from the centre of the substrate, it was assumed that these cracks actually initiated from the top surface where maximum tensile stresses were found.
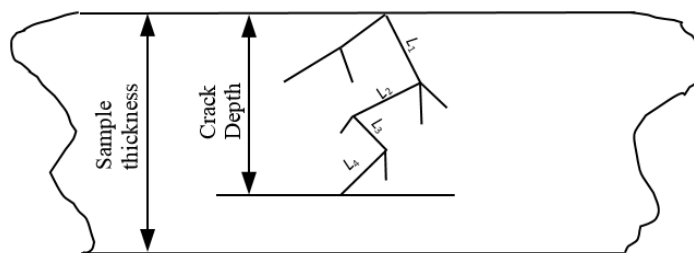
Figure 4.26: Schematic diagram of SCC crack measurements on the cross-section of the 304L SS substrate.

The crack density and crack growth rate were calculated based on Equations 4.1 and 4.2 respectively. Some cracks were shallow and others deeper.

$$\text{Crack density} = \frac{\text{Total no. of cracks}}{\text{substrate thickness (mm)}} \qquad (4.1)$$

$$\text{Crack growth rate} = \frac{\text{Longest crack length (mm)}}{\text{Experiment exposure time (s)}} \qquad (4.2)$$

These cracks were classified into groups as shown in Figure 4.27 to Figure 4.31. The cracks were counted on polished samples using an optical microscope at 100X magnification.
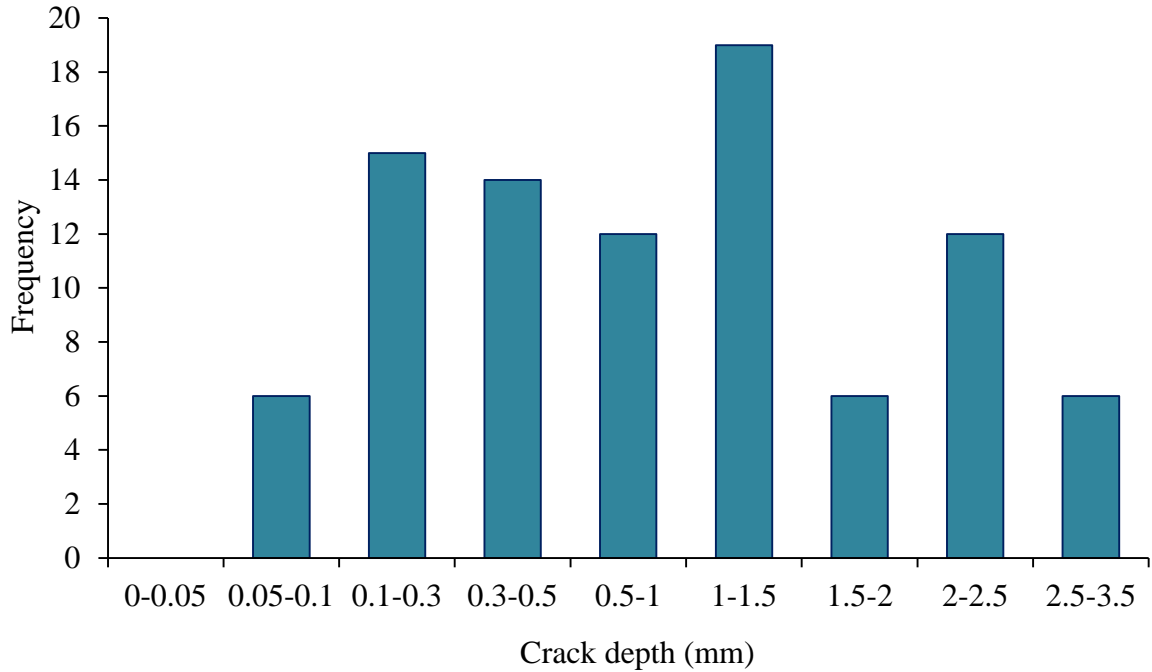
Figure 4.27: Distribution of crack lengths of polished as-received 304L stainless steel after exposure to 50 ppm NaCl containing 10 ppm DO at 160˚C for 172 hours.
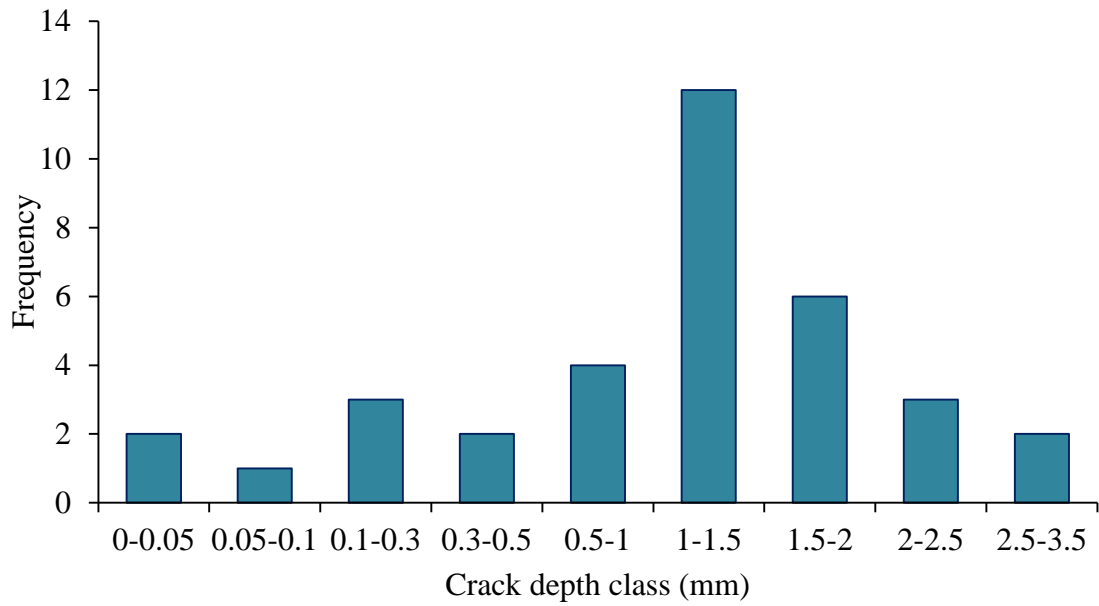
Figure 4.28: Distribution of crack lengths of polished laser alloyed 304L SS with 0 wt% Ru after exposure to 50 ppm NaCl containing 10 ppm DO at 160˚C for 172 hours.
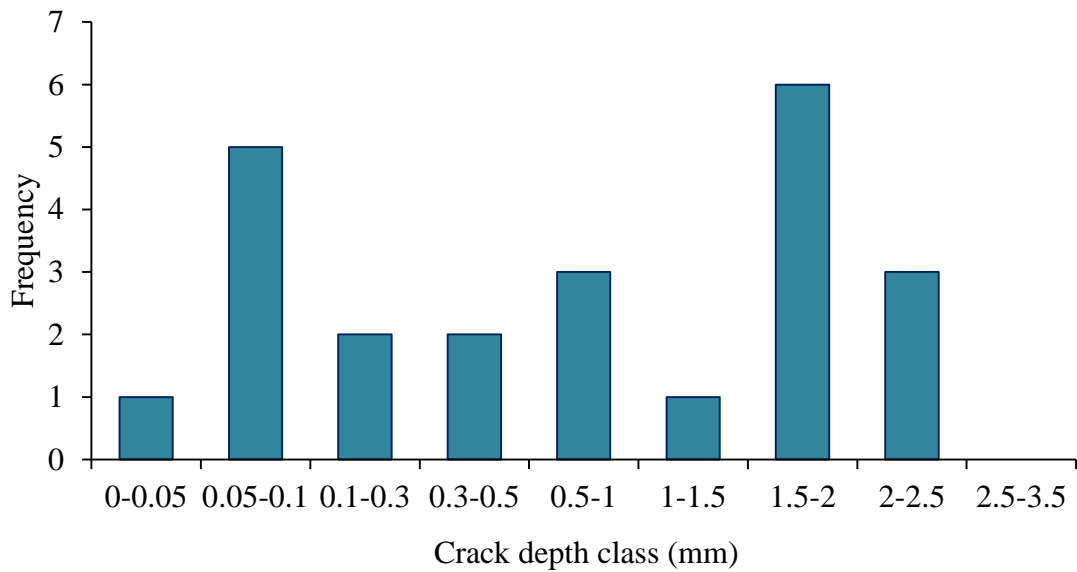
Figure 4.29: Distribution of crack lengths of polished laser alloyed 304L SS with 0.98 wt% Ru after exposure to 50 ppm NaCl containing 10 ppm DO at 160˚C for 172 hours.
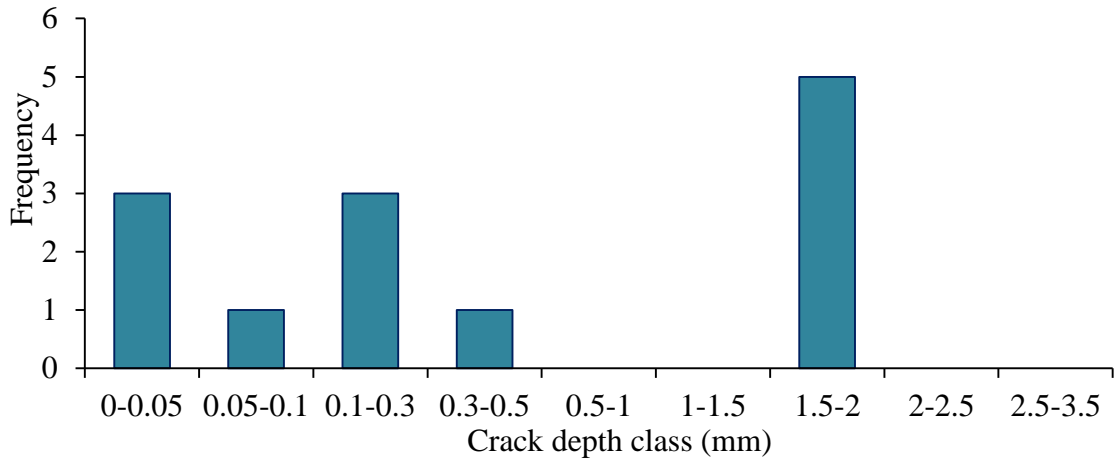
Figure 4.30: Distribution of crack lengths of polished laser alloyed 304L SS with 1.96 wt% Ru after exposure to 50 ppm NaCl containing 10 ppm DO at 160˚C for 172 hours.

The crack length and depth reduced as the Ru content was increased. The longest crack length measured was approximately 4.5 mm and this was for samples with 0 wt% Ru and as-received 304L SS as shown in Figure 4.31. The shortest crack measured was found on samples with 1.96 wt% Ru. The crack depth decreased substantially with increasing Ru content.
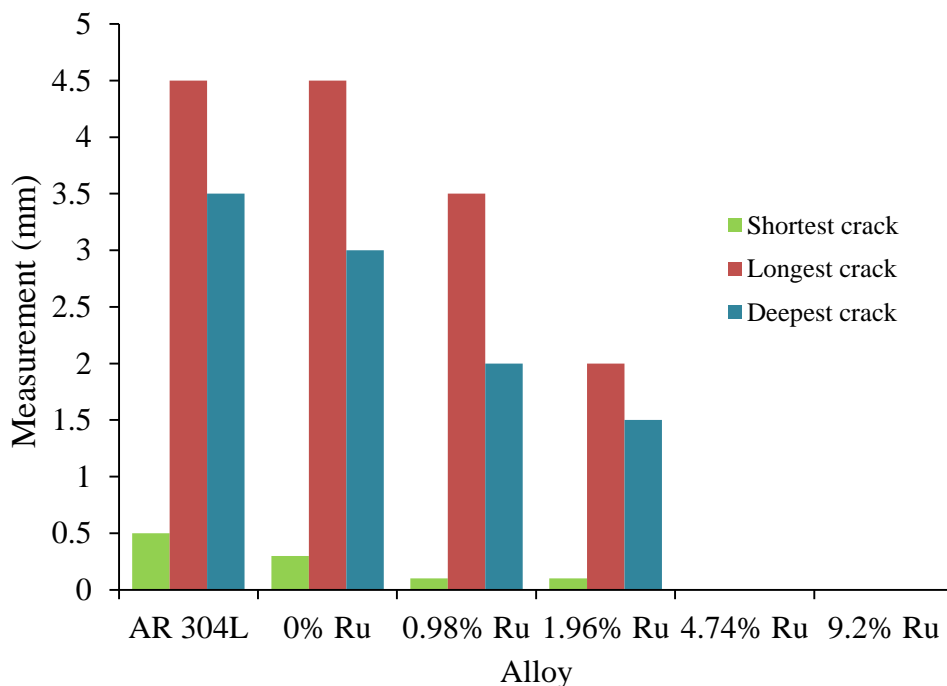
Figure 4.31: Comparison of crack depth and length of polished samples after exposure to 50 ppm NaCl solution with 10 ppm DO at 160˚C for 172 hours.

The crack density and crack growth rate were obtained based on Equations 4.1 and 4.2 respectively. As expected, the crack propagation rate reduced with increasing Ru content (Table 4.1).

Table 4.1: Crack growth rate of Ru laser alloyed 304L SS in 50 ppm NaCl with 10 ppm DO at 160˚C for 172 hours.

Sample	Crack length [mm]	Crack density [mm^{-1}]	Crack growth rate [x10^{-6}mm /s]	SCC susceptibility
Untreated 304L	4.5	18	7.27	Present
304L + 0% Ru	4.3	7	6.95	Present
304L + 0.98% Ru	3.5	4	5.65	Present
304L + 1.96% Ru	2	2	3.23	Present
304L + 4.74% Ru	-	-	-	No SCC
304L+ 9.2% Ru	-	-	-	No SCC

4.3.4   Stress corrosion cracking of VAR samples

The SSRT was performed to investigate the SCC susceptibility of vacuum remelted samples with Ru. It should be noted here that laser alloyed samples were not tested using this technique (SSRT) because of the sample size and clad orientation. However, the fractography analysis by SEM was used to investigate SCC susceptibility of vacuum remelted samples, the samples experienced ductile failure as shown in Figure 4.32 to Figure 4.37. There was no evidence of SCC cracks on the necking region of the samples. The study of VAR samples was performed to understand further the effect of Ru on SCC.
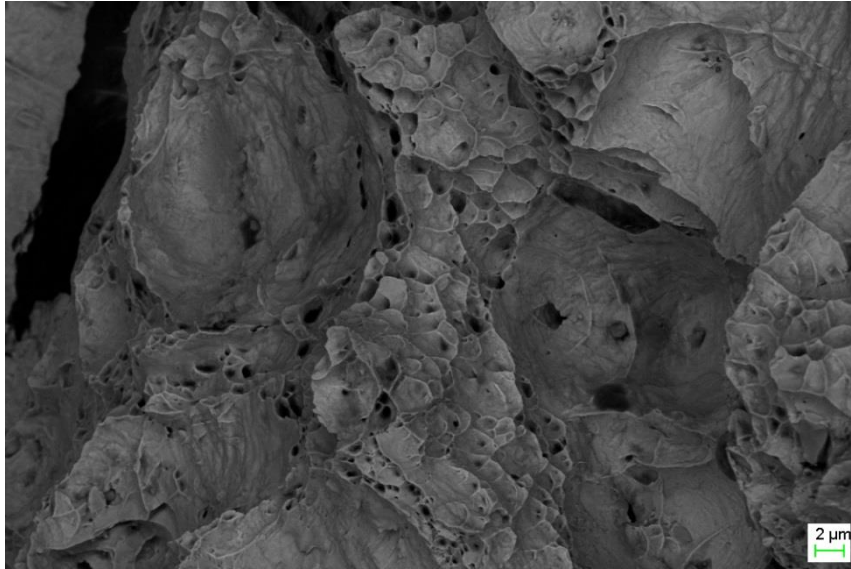
Figure 4.32: Fractured surface of as-received 304L SS in 50 ppm NaCl solution containing
10 ppm DO at 160˚C.
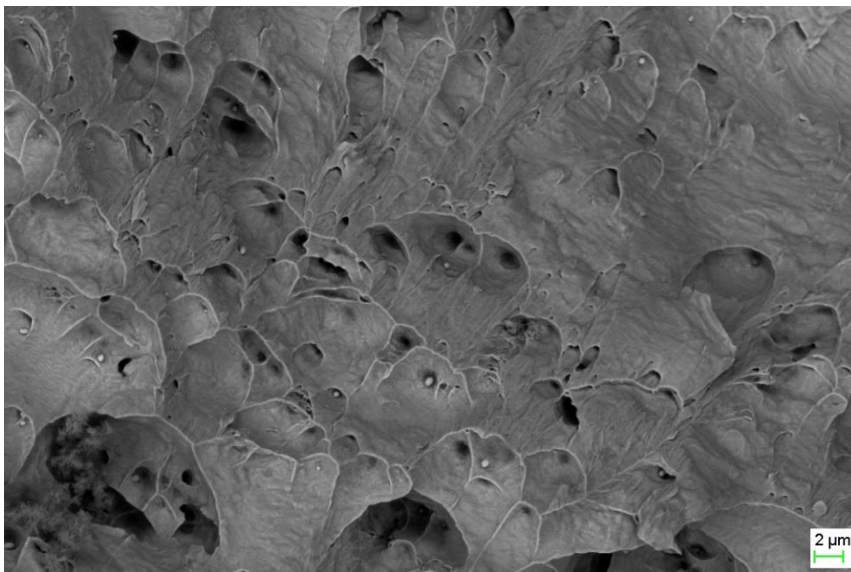
Figure 4.33: Fractured surface of vacuum remelted 304L SS with 0 wt% Ru in 50 ppm NaCl
solution containing 10 ppm DO at 160˚C.
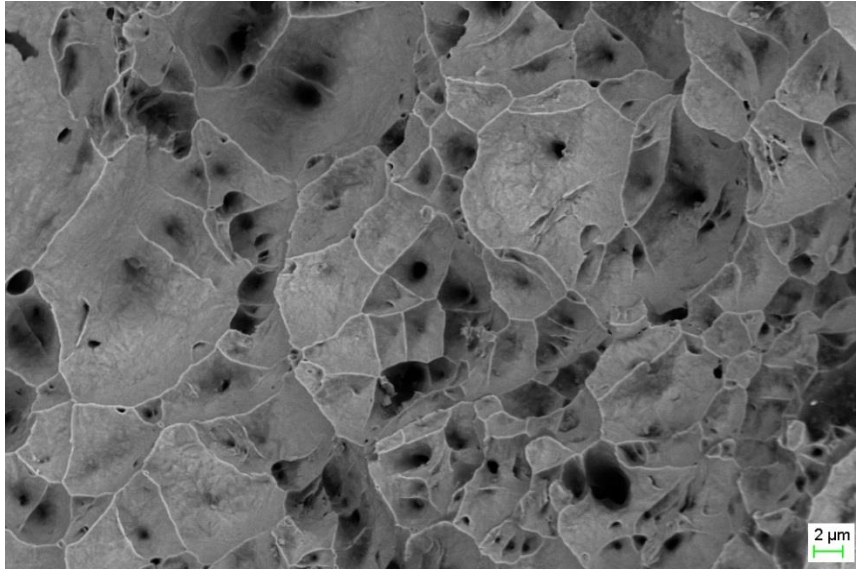
Figure 4.34: Fractured surface of vacuum remelted 304L SS with 1.07 wt% Ru in 50 ppm
NaCl solution containing 10 ppm DO at 160˚C.
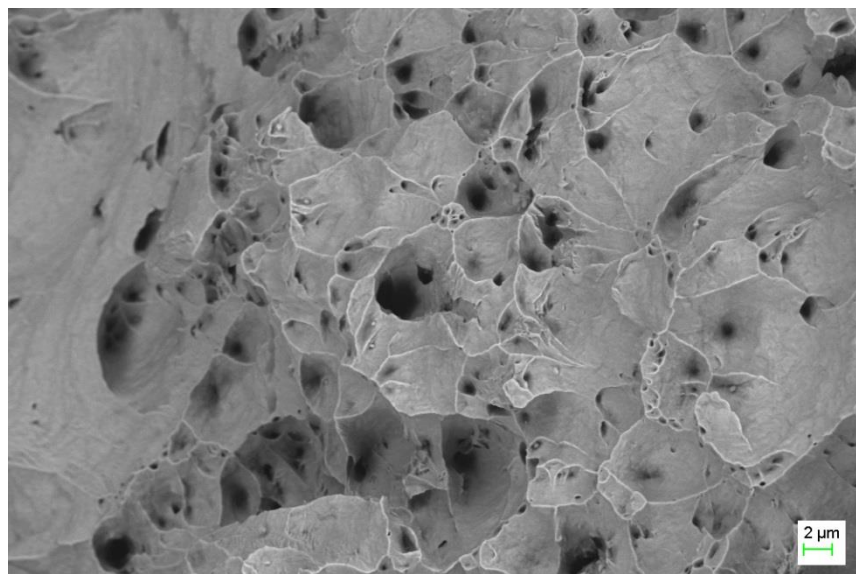
Figure 4.35: Fractured surface of vacuum remelted 304L SS with 2.05 wt% Ru in 50 ppm
NaCl solution containing 10 ppm DO at 160˚C.
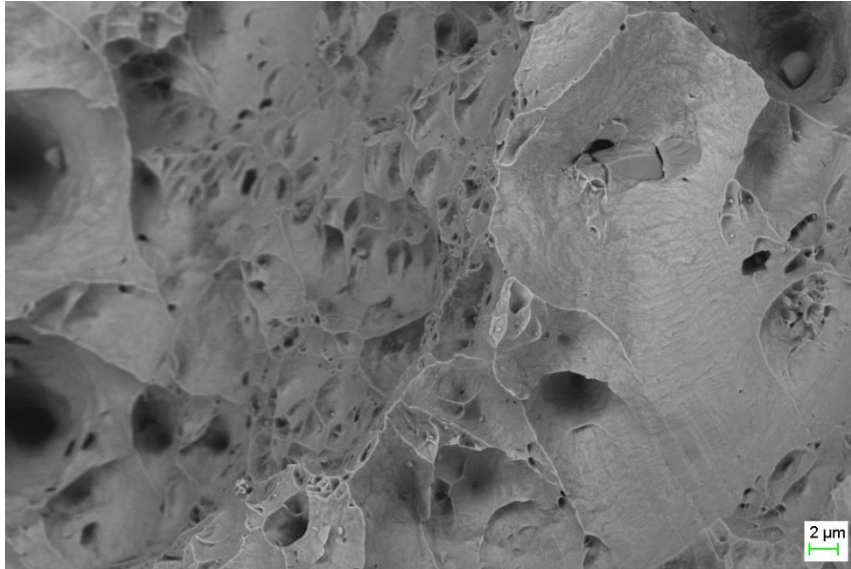
Figure 4.36: Fractured surface of vacuum remelted 304L SS with 6.07 wt% Ru in 50 ppm NaCl solution containing 10 ppm DO at 160˚C.
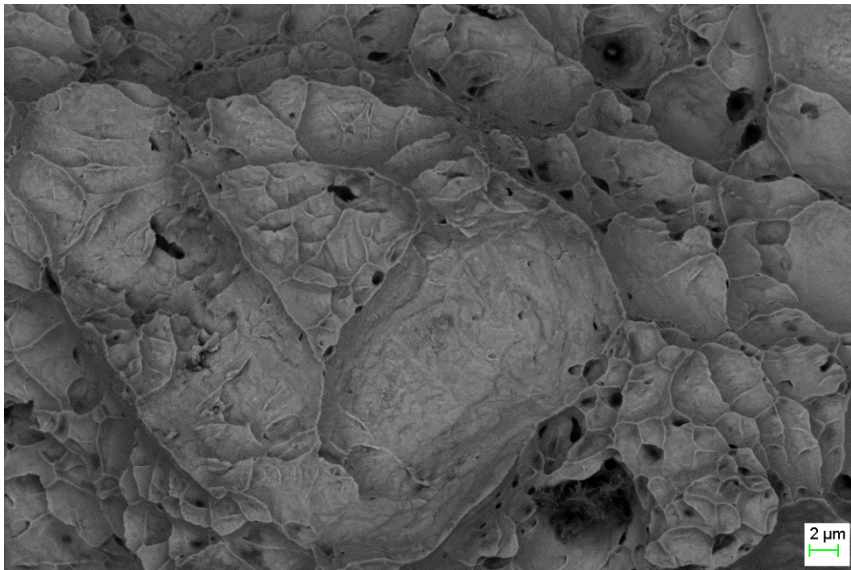
Figure 4.37: Fractured surface of vacuum remelted 304L SS with 12.34 wt% Ru in 50 ppm NaCl solution containing 10 ppm DO at 160˚C.

The elongation and reduction in area of the Ru VAR samples was calculated according to Equations 4.3.and 4.4 respectively.

$$Elongation = \left(\frac{l_f - l_o}{l_o}\right) \times 100 \qquad (4.3)$$

$$Reduction\ in\ area = \left(\frac{d_o^2 - d_f^2}{d_o^2}\right) \times 100 \qquad (4.4)$$

Where l_f is the final length (mm), l_o is the original length (mm), d_f and d_o is the final and original diameter in mm. The data was tabulated in Table 4.2.

Table 4.2: SSRT results of vacuum remelted 304L stainless steel with Ru.

Ru addition (wt%)	Elongation (%)	Reduction in area (%)	Maximum stress threshold (MPa)	Time to failure (hrs)
As-received 304L SS	8.2	32.4	325	13.2
304L SS + 0% Ru	10.5	36.1	349	14.6
304L SS+ 1.07% Ru	41	72.4	580	38.2
304L SS+ 2.05% Ru	25	66.9	564	29.4
304L SS+ 6.07% Ru	19.5	60.9	476	22.3
304LSS + 12.3% Ru	18	31.9	448	19.6

The effect of Ru at high levels (more than 1.07 wt%) showed a decrease in failure time. It was evident from Figure 4.38 that the elongation decreased as the Ru content was increased.
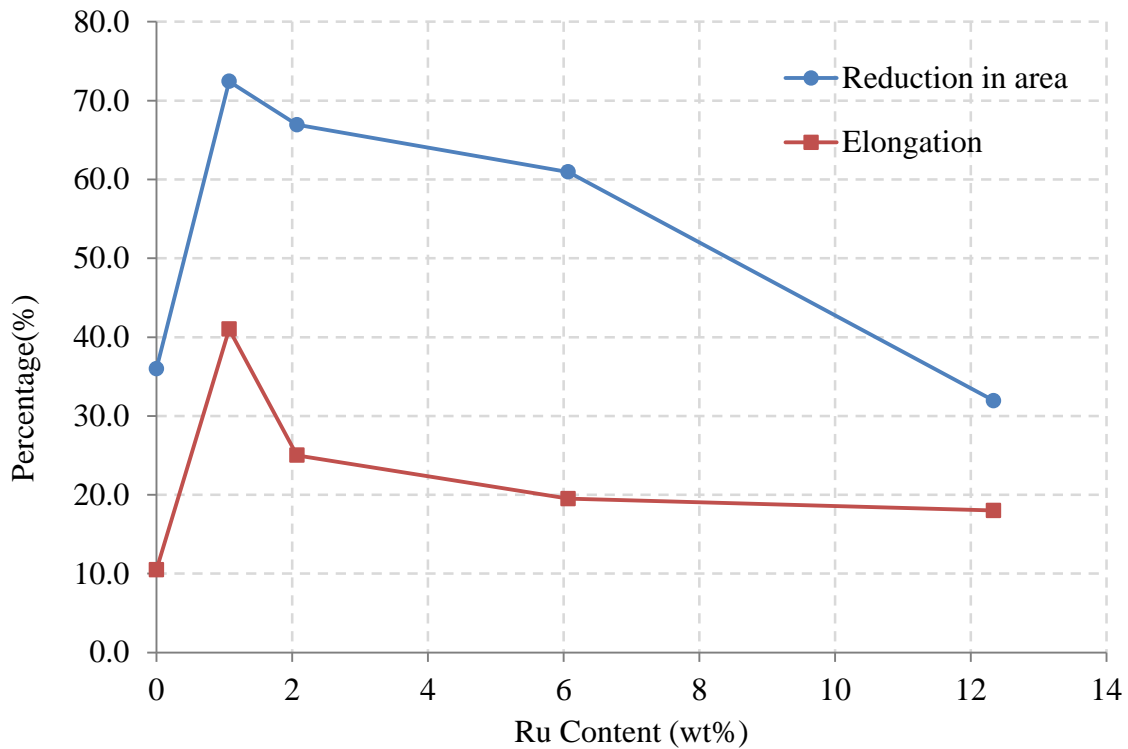
Figure 4.38: Elongation and reduction in area of vacuum remelted 304L stainless steel with Ru after exposure to 50 ppm NaCl solution and 10 ppm DO at 160˚C.

4.4 High temperature electrochemical corrosion

In most engineering applications, it is common to use corrosion resistant metals to prevent structural failure (NPL, 2016). In this study, the corrosion behaviour of the LSA and VAR samples was examined at 25°C, 100°C and 160°C in sodium chloride purged with oxygen. The untreated 304L stainless steel was used as a control alloy. The study was focused at evaluating the corrosion potential (E_{corr}), passive potential (E_{pass}), critical current (i_{crit}), passive current (i_{pass}), corrosion current (i_{corr}), and corrosion rates at high temperatures.

4.4.1   Electrochemical evaluation of LSA samples

The OCP was run for 12 hours on as-received 304L stainless steel samples. As shown in Figure 4.39, the film was active as the data showed stable points at room temperature (25°C). The data was sporadic between -300 mV and -200 mV at high temperature (160°C). The instability of data at the high temperature could be related to the surface activity changes between the passive film and the solution.
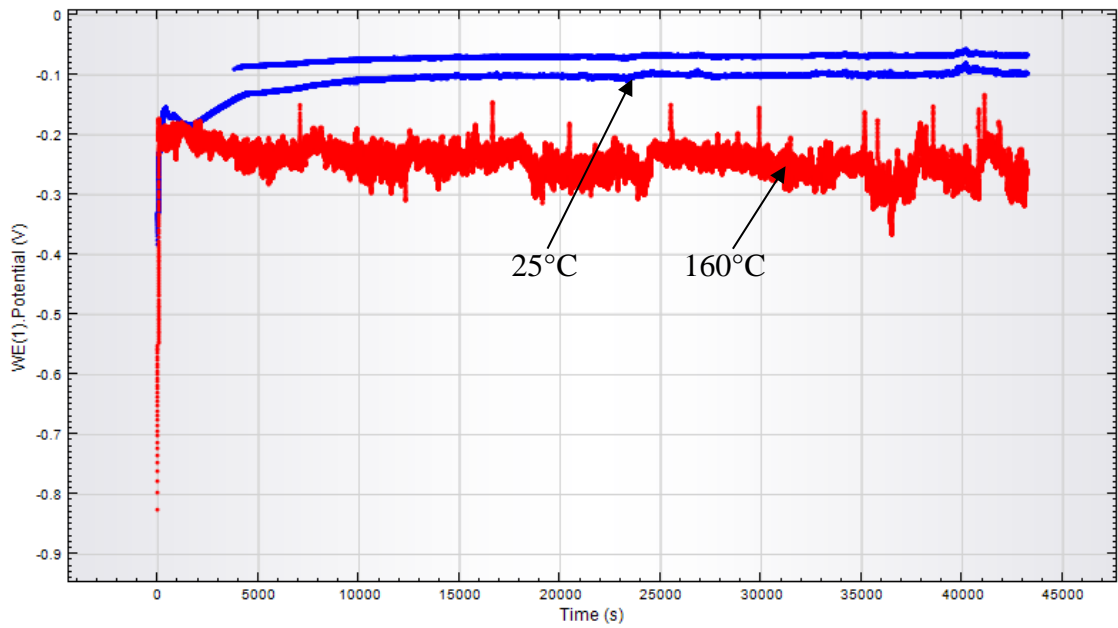
Figure 4.39: The OCP of as-received 304L SS in 50 ppm NaCl solution containing 10 ppm DO at 25°C and 160°C.

The as-received 304L stainless steel showed an increase in current density as the temperature increased (Figure 4.40). At room temperature there was pitting behaviour observed at approximately 0.4 V. However, the i_{crit} was at 2.33 x 10^{-6} A/cm.
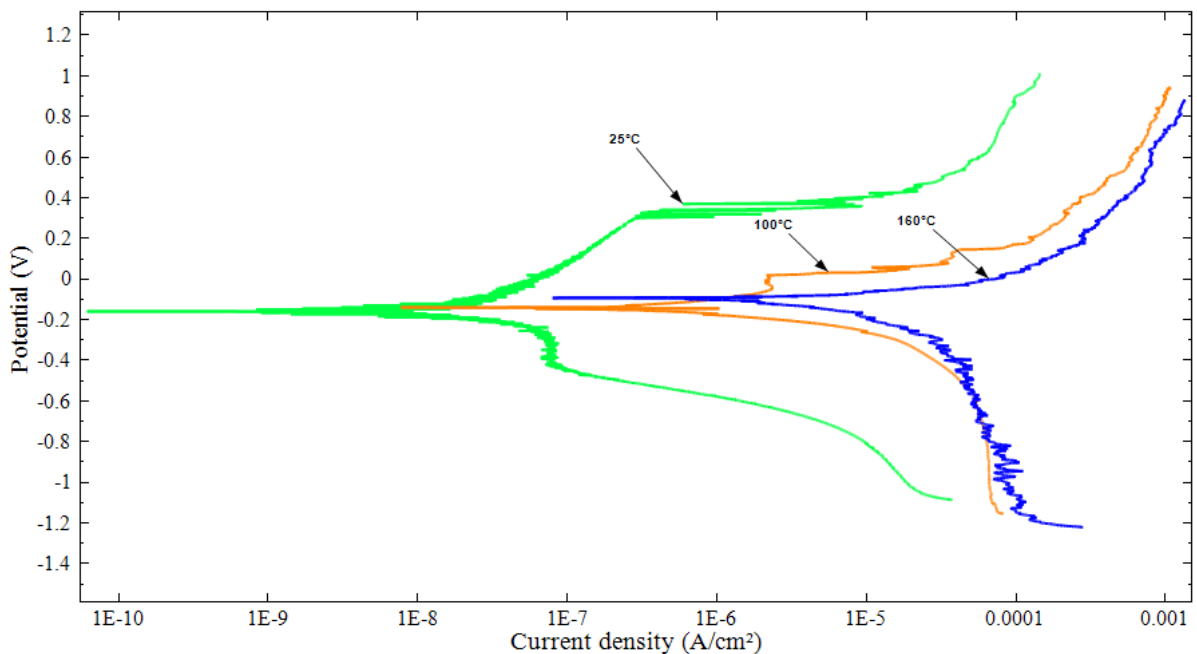
Figure 4.40: Potensiodynamic polarisation curve of as-received 304L SS in 50 ppm NaCl containing 10 ppm DO.

The samples with 0% Ru (i.e laser surface alloyed with powders of 304 stainless steel and 2%Ni) had lower E_{corr} when compared to as-received 304L stainless steel. As shown in Figure 4.41 the i_{crit} and E_{crit} was recorded at 0.11 x 10^{-6} A/cm^2 and -0.15 V at 25˚C. There was no evidence of passivity at elevated temperatures.
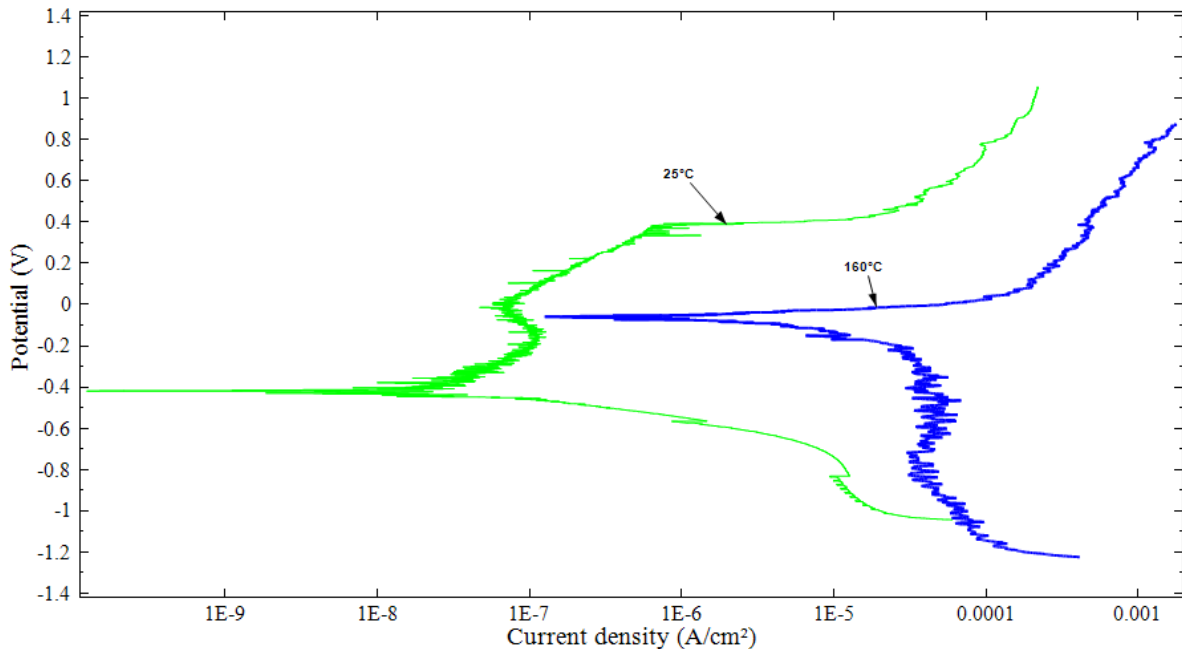
Figure 4.41: Potentiodynamic polarisation curve of laser alloyed 304L SS with 0 wt% Ru in 50 ppm NaCl containing 10 ppm DO.

An improvement in corrosion resistance was observed as the Ru content was increased from 0 to 1.96 wt% Ru as shown in Figure 4.42 and Figure 4.43. The current densities were lower than those obtained for as-received 304L stainless steel. At high temperature (160°C) the sample with 0.98 wt% Ru achieved the i_{crit} and E_{crit} of 23.4 x 10^{-6} A/cm^2 and 0.05 V respectively. A passivation potential, E_{pass} of 0.22 V was obtained at a relatively constant current density of 2.1 x 10^{-5} A/cm^2 at high 160°C, as shown in Figure 4.42.
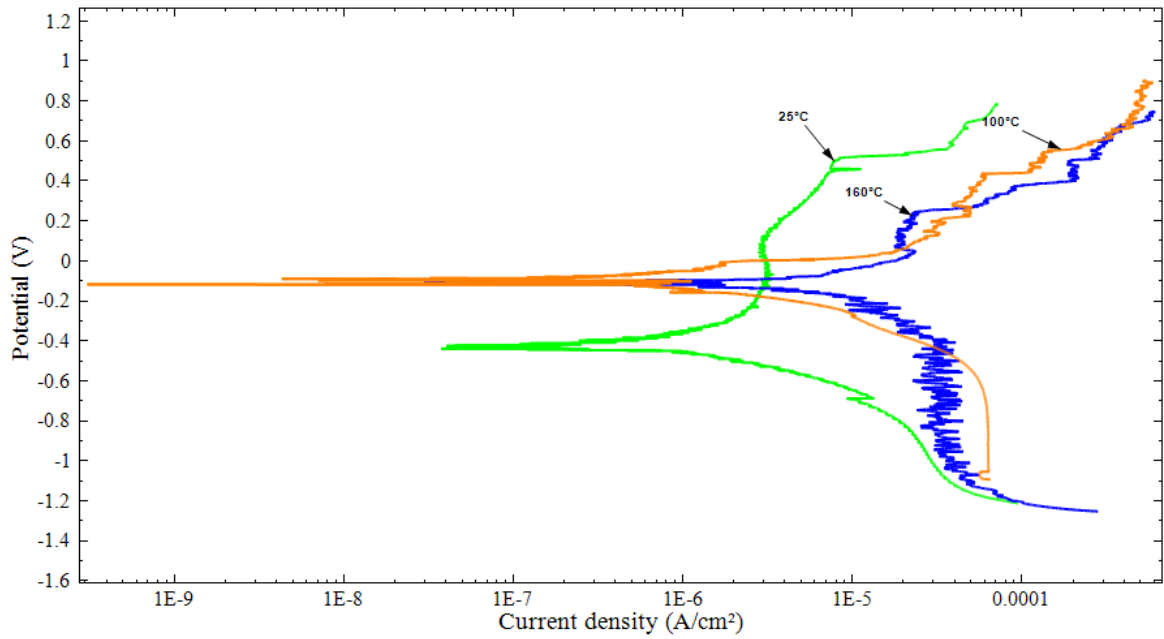
Figure 4.42: Potentiodynamic polarisation curve of laser alloyed 304L SS with 0.98 wt% Ru in 50 ppm NaCl containing 10 ppm DO.
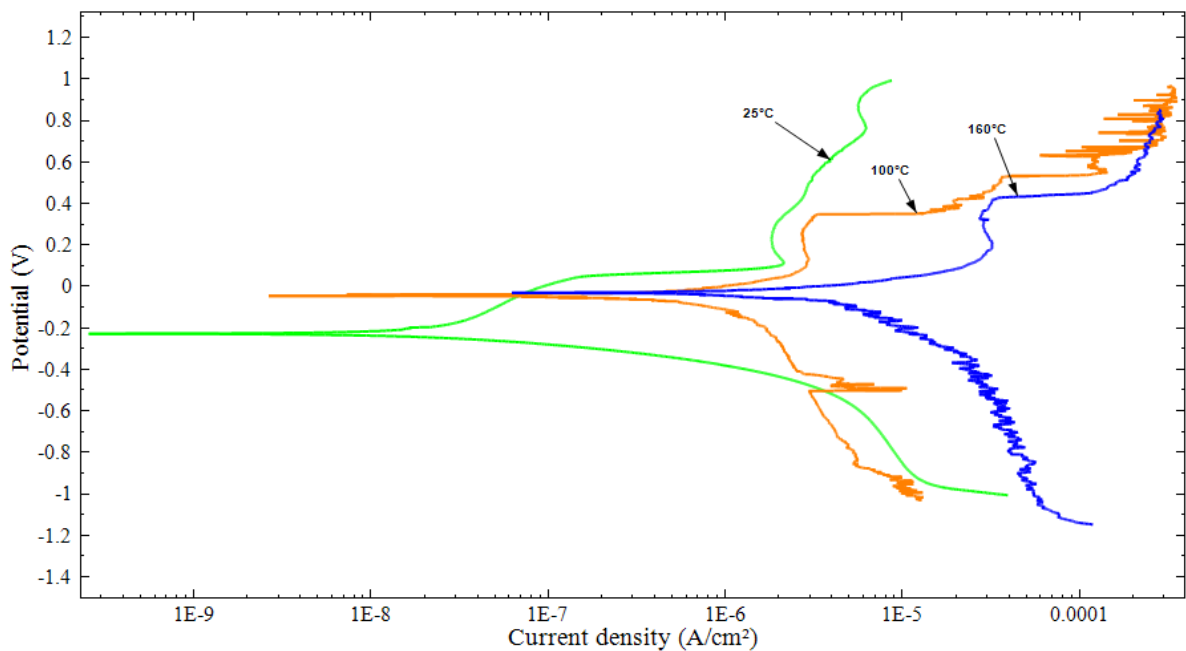
Figure 4.43: Potentiodynamic polarisation curve of laser alloyed 304L SS with 1.96 wt% Ru in 50 ppm NaCl containing 10 ppm DO.

The current density of LSA samples with 4.74 wt % Ru was higher when compared to those with low Ru content (0, 0.98 and 1.96 wt%). The i_{crit} and E_{crit} at 160°C was 4.63 x10^{-6} A/cm^2 and 0.12 V as shown in Figure 4.44 respectively. However, there was a sudden decrease and

78

increase in current density in the passive region at 160°C. This could be related to the breaking of the film as the pits were formed. The measured pitting potential, E_p, was 0.27 V and was higher than E_{corr}.
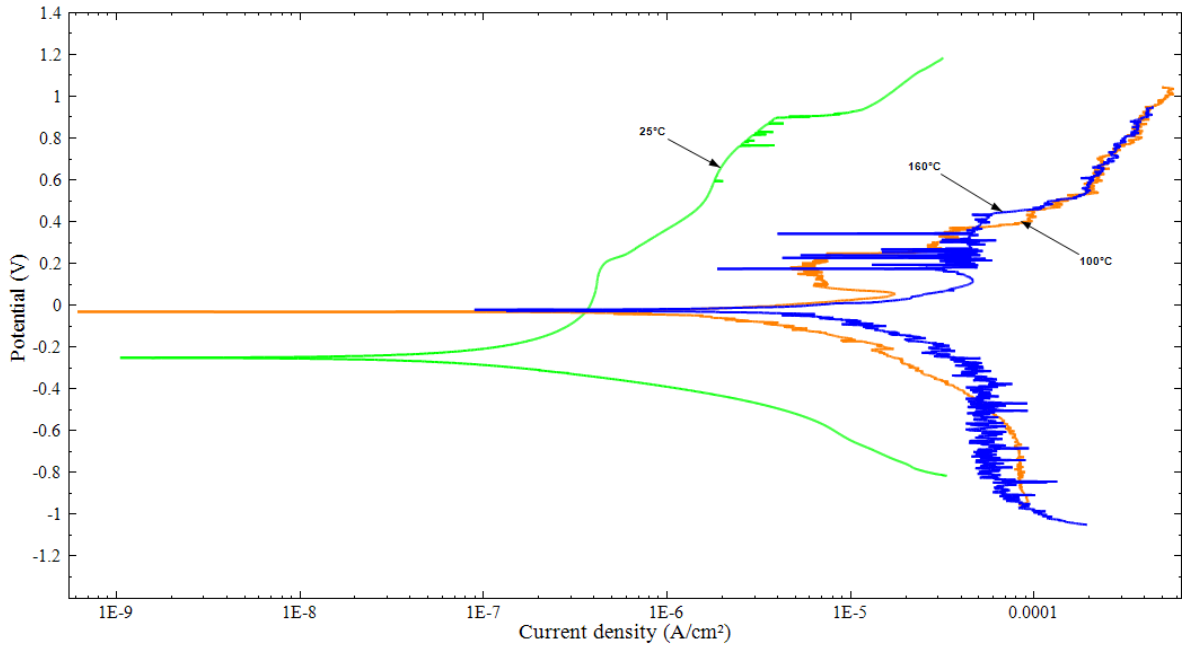
Figure 4.44: Potentiodynamic polarisation curve of laser alloyed 304L SS with 4.74 wt% Ru in 50 ppm NaCl containing 10 ppm DO.

Observing the potentials at higher level of Ru (9.2 wt%) revealed passivation of the oxide layer at 100°C and 160°C as shown in Figure 4.45. The primary passivation potential and critical current density at 160°C was 0.15 V and 6.79 x 10^{-5} A/cm^2 respectively. Although there was passivation in these samples, the current density was still high when compared to samples with lower Ru content (0, 0.98, 1.96 and 4.74 wt%).
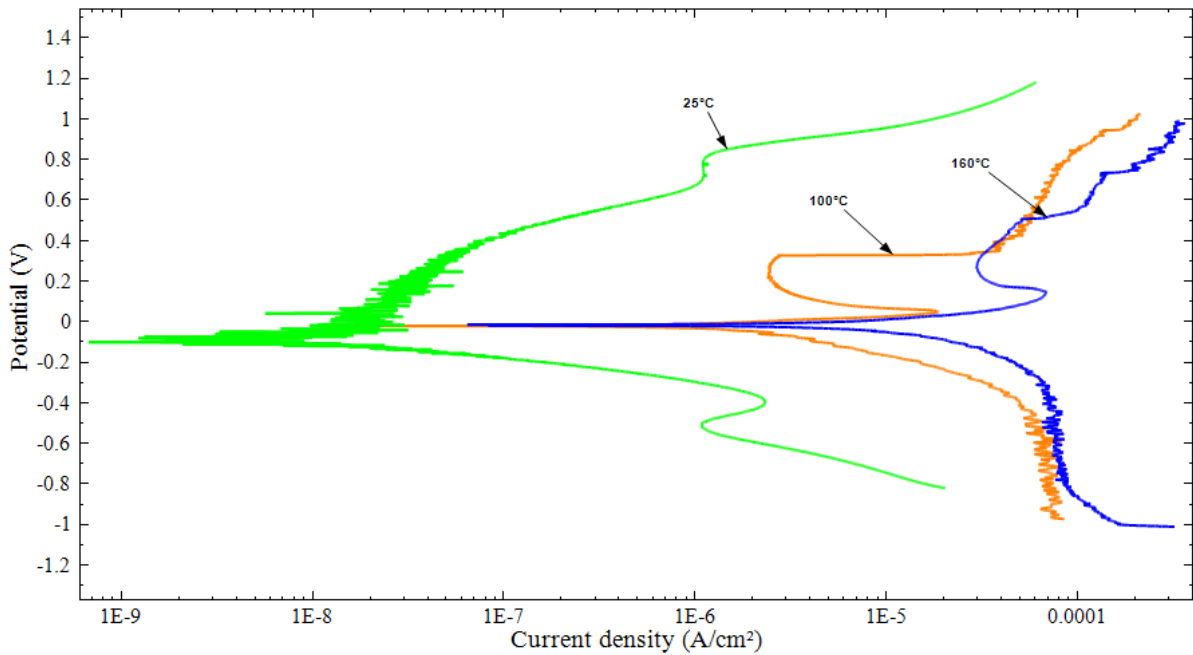
Figure 4.45: Potentiodynamic polarisation curve of laser alloyed 304L SS with 9.2 wt% Ru in 50 ppm NaCl containing 10 ppm DO.

It should be noted that the experimental factors (electrical connectivity of wires, contacts through the autoclave, reference electrode and thermal conductivity) were eliminated and the data from polarisation curves was used to calculate the corrosion rates as shown in Table 4.3.

Table 4.3: Polarisation data of laser alloyed samples with Ru after exposure to 50 ppm and 10 ppm DO at 160°C.

SAMPLE	E_{corr} [mV]	R_p [ohms]	i_{corr} [µA/cm^2]	Corrosion rate [mm/year]
AR 304L SS	-94.4	3522	18.1	0.20
304L + 0 %Ru	-58.9	6240	10.2	0.11
304L + 0.98 %Ru	-105	9235	6.92	0.07
304L + 1.96 %Ru	-125	16144	3.96	0.04
304L + 4.74 %Ru	-357	11000	5.83	0.06
304L + 9.2 %Ru	-13.9	3172	20.1	0.22

There was a decrease in corrosion rates as the Ru content was increased to 1.96 wt%. The results obtained for alloys with 9.2 wt% Ru showed higher corrosion rate when compared to as-received 304L stainless steel as shown in Figure 4.46.
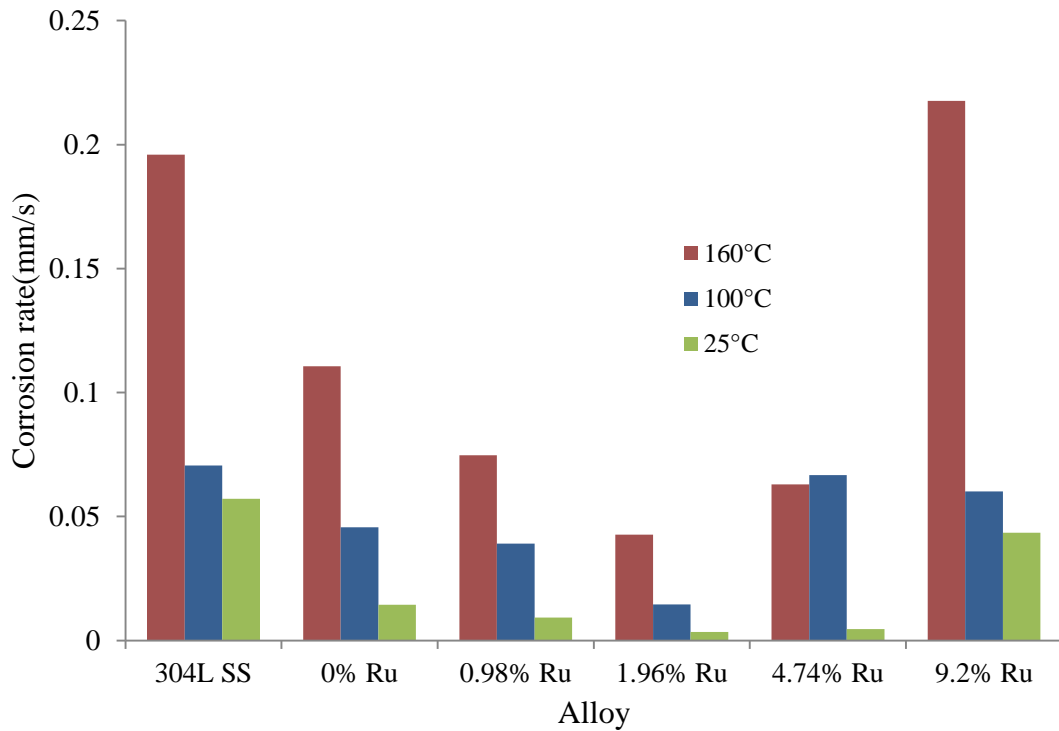
Figure 4.46: Corrosion rate of samples in an oxygenated (10 ppm DO) sodium chloride solution (50 ppm) at different temperatures.

4.4.2   Electrochemical evaluation of VAR samples

The corrosion behaviour of vacuum remelted 304L stainless steel with Ru was evaluated by polarisation curve analysis. It was evident from these curves (Figure 4.47 to Figure 4.51) that the current density increased as the temperature was increased. At room temperature (25˚C) the samples with 0 wt% Ru (i.e free ruthenium) behaved as expected, the E_{corr} and I_{corr} values were relatively similar to those of as-received 304L stainless steel. However, this was not the case at high temperatures. Passivity occurred and the corrosion potential was higher as shown in Figure 4.47.
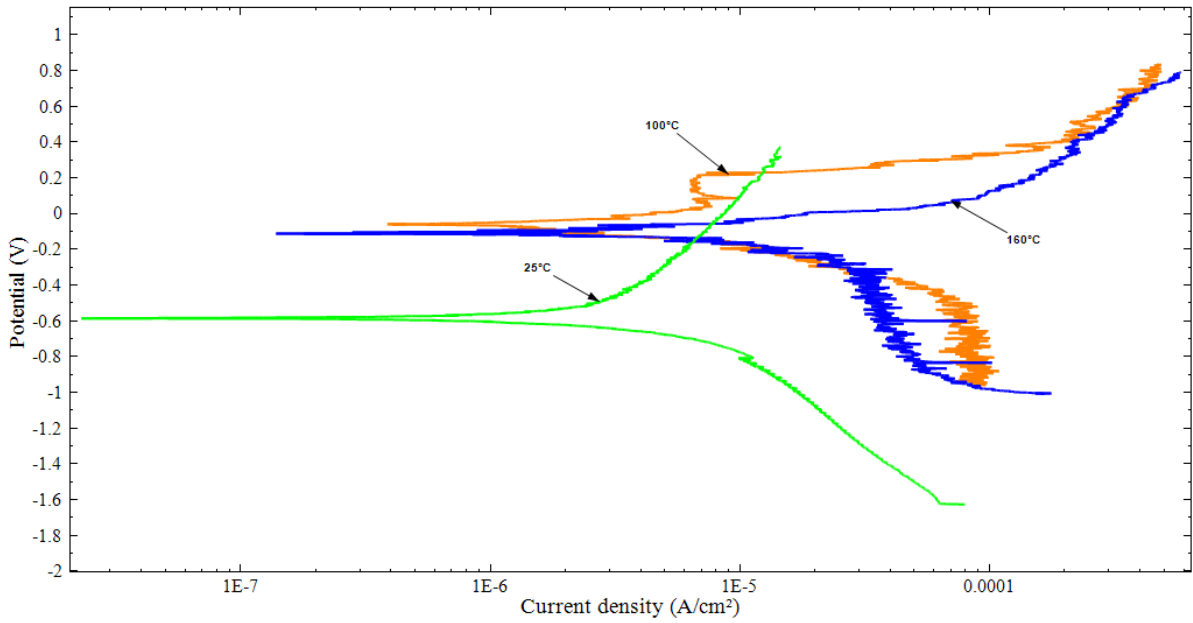
Figure 4.47: Potentiodynamic polarisation curve of vacuum remelted 304L SS with 0 wt% Ru in 50 ppm NaCl containing 10 ppm DO.
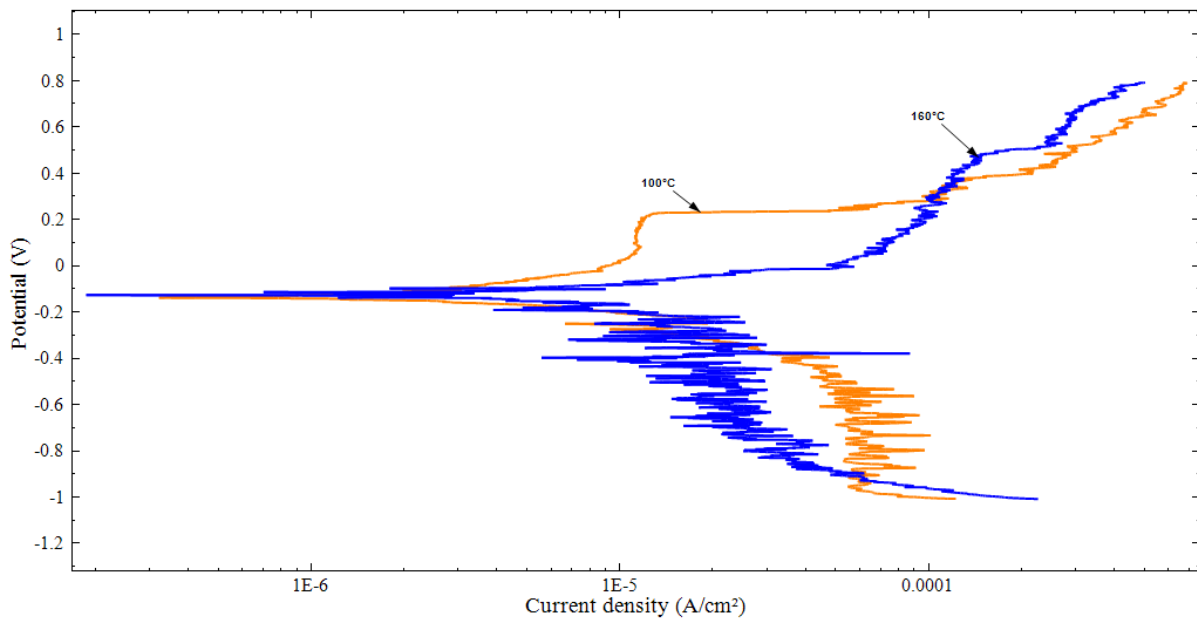
Figure 4.48: Potentiodynamic polarisation curve of vacuum remelted 304L SS with 1.07 wt% Ru in 50 ppm NaCl containing 10 ppm DO.
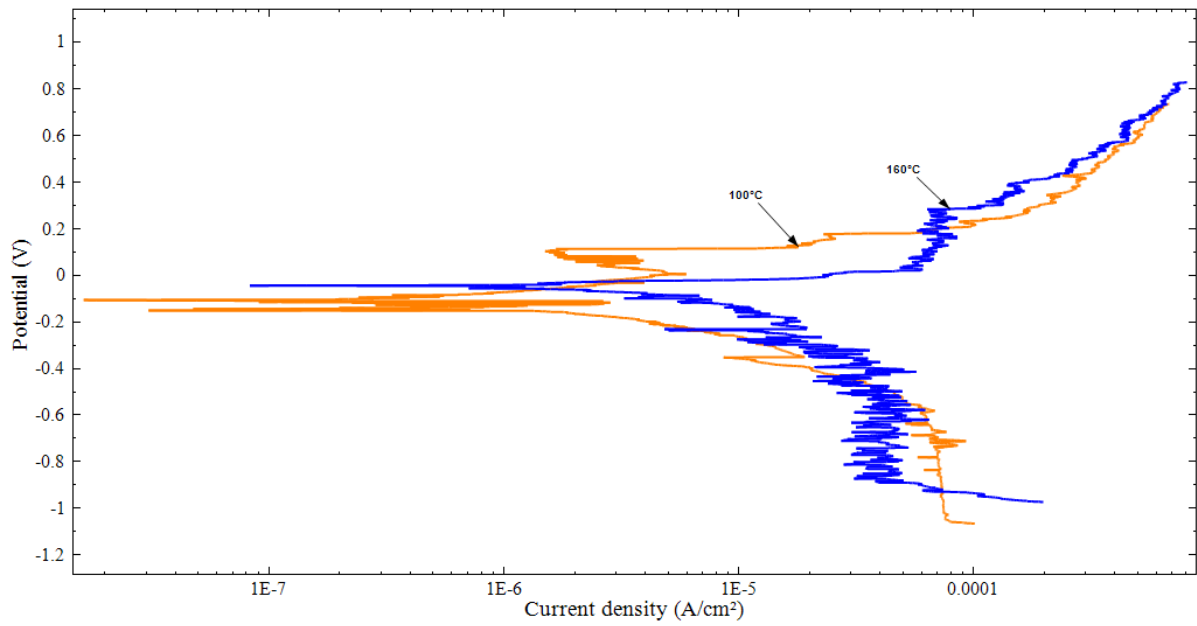
Figure 4.49: Potentiodynamic polarisation curve of vacuum remelted 304L SS with 2.05 wt% Ru in 50 ppm NaCl containing 10 ppm DO.
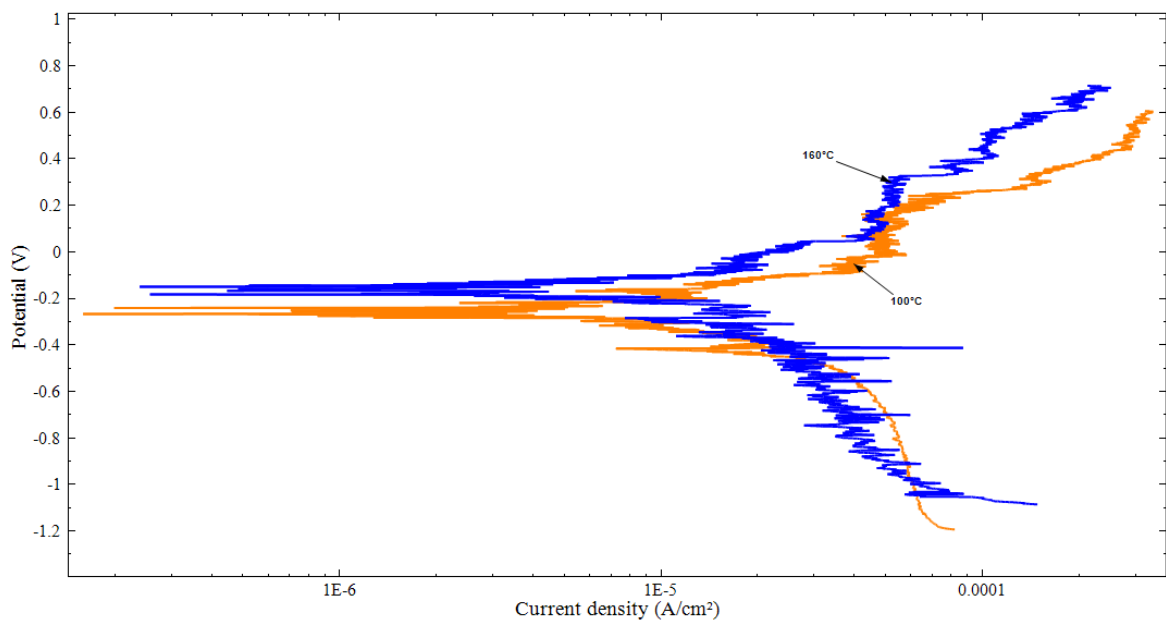
Figure 4.50: Potentiodynamic polarisation curve of vacuum remelted 304L SS with 6.07 wt% Ru in 50 ppm NaCl containing 10 ppm DO.
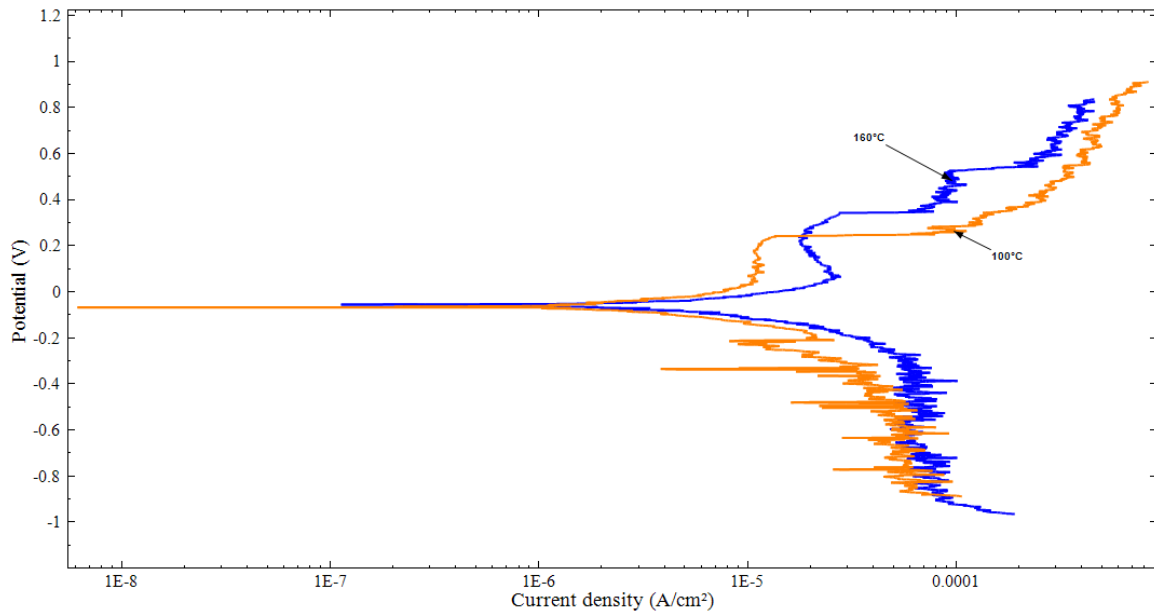
Figure 4.51: Potentiodynamic polarisation curve of vacuum remelted 304L SS with 12.34 wt% Ru in 50 ppm NaCl containing 10 ppm DO.

4.4.3 Post potentiodynamic exposure

In general, a passive film in austenitic stainless steels protects the metal surface from corrosion attack. Austenitic stainless steels will repassivate and maintain the passive film in chloride solutions at lower temperatures. However, in this study, the passivity of vacuum remelted 304L SS with Ru was compromised and after exposure pits were found on the surface of the samples. The pits were irregular and formed randomly on the surface. However, there was no evidence of pits after exposure at room temperature. The pits observed on the vacuum remelted samples are shown in Figure 4.52 to Figure 4.54**.**
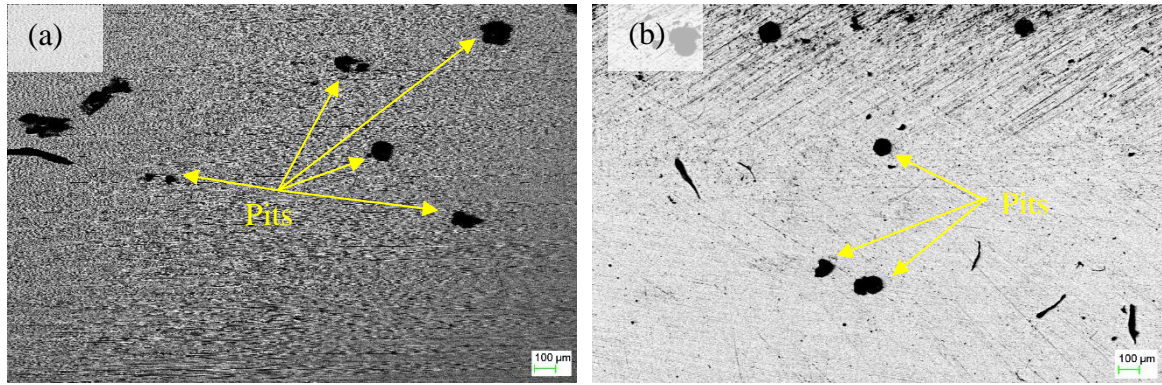
Figure 4.52: Pitting observed after electrochemical test exposure in 50 ppm NaCl with 10 ppm DO at 160°C (a) As-received 304L SS (b) 0 wt% Ru.
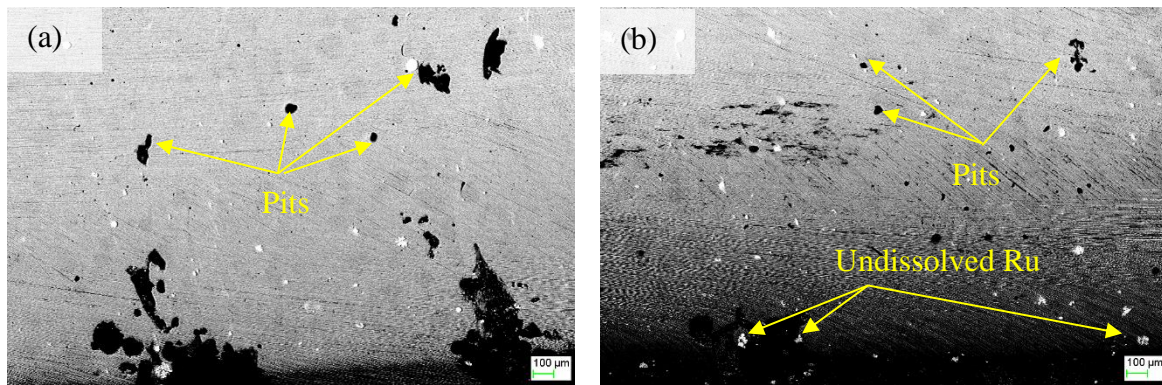
Figure 4.53: Pitting observed after electrochemical test exposure of VAR samples in 50 ppm NaCl with 10 ppm DO at 160°C (a) 0.98 wt% Ru (b) 1.96 wt% Ru.
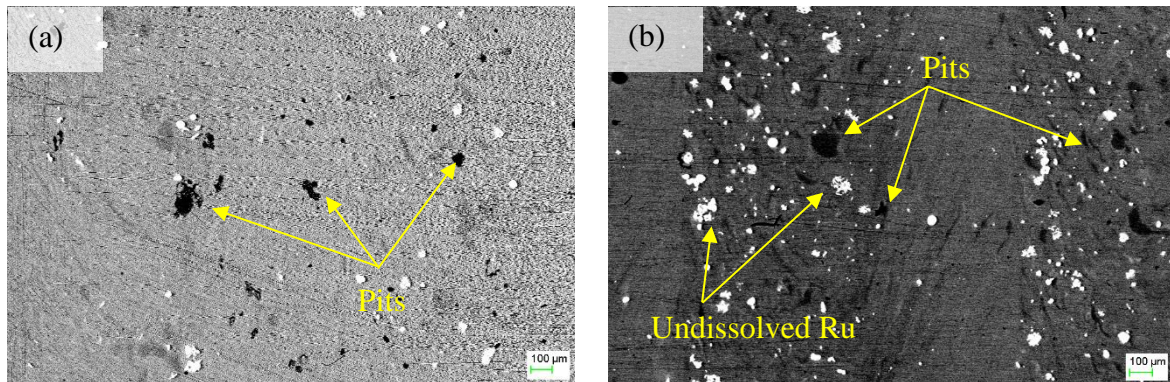
Figure 4.54: Pitting observed after electrochemical test exposure of VAR samples in 50 ppm NaCl with 10 ppm DO at 160°C (a) 4.74 wt% (b) 9.20 wt% Ru.

The pit density (the number of pits per surface area) and size of vacuum remelted samples exposed to 50 ppm NaCl solution and 10 ppm DO at 160°C was calculated and recorded in Table 4.4. The pit density decreased as the Ru content was increased. The alloys with lower

Ru contents 0.98 and 1.96 wt% Ru, had higher pit densities than the other alloys (4.74 and 9.2 wt% Ru).

Table 4.4: Corrosion pit measurements of VAR samples.

SAMPLES	Pit density [pit/mm^2]	Average pit Diameter [μm]
As-received 304LSS	44	301
304L SS + 0% Ru	21	917
304L SS + 1.07% Ru	38	142
304L SS + 2.07% Ru	14	145
304L SS + 6.05% Ru	25	139
304L SS + 12.34% Ru	13	89

There were few pits found on LSA samples after exposure in 50 ppm sodium chloride containing 10 DO at 160°C. This could be attributed to refined microstructure of the alloyed improving the strength of the passive film. This behaviour is elaborated by the polarisation curves discussed in section 5.4.

4.4 Repeatability of results

In this study, the tests (Hardness, SCC and electrochemical tests) were repeated to validate the results. There was no significant change in crack propagation rates; the only difference observed was that most of the cracks propagated in a transgranular manner. The repeatability of SSRT tests revealed similar failure time and the fracture morphology. The repeatability of electrochemical results was necessary to account for surface homogeneity and possible crevice corrosion at sample–sealant interface. The results obtained correlated with the first results obtained. A slight change was observed on electrochemical results for both the LSA and VAR samples. Sporadic polarisation curves were observed for these samples but the corrosion rates were within the margin ±2%.

4.5 Error estimates

It is a common practice to calibrate experimental equipment before starting any test. The factors which could have comprised the results were eliminated. For instance, hysteresis was reduced by loading and unloading the sample before taking measurements of the applied stress for SCC test. The marginal error was below 1%, which showed that the applied tensile stress of the sample on a three-point rig was valid. All other instruments such as the digital vernier calliper were re-set to zero before taking measurements. Although, some of the equipment such as the potentiostat was calibrated by the manufacturer, it was checked for functionality by using a dummy sample.

Uncertainty in experimental data can come from different sources. The primary goal was to minimise any possible sources of error for all experiments conducted in this study. The possible factors (e.g electrical conductivity in an autoclave) which could have influenced electrochemical results were minimised at all times. Prior to commencing the tests, the instruments were checked and tested for calibration, and standard routine procedure was performed. Although there were sporadic changes in electrochemical data at high temperatures it could be summarised that the data obtained in this study was within the expected error limits.

CHAPTER 5

DISCUSSION

5.1 Microstructural analysis

The microstructure of metallic materials usually depends on the chemical composition, heating rate, processing temperature and cooling rates. In this study, the microstructure of as-received 304L stainless steel as well as LSA and VAR samples was investigated.

The microstructure of as-received 304L stainless steel had equiaxed grains with double twin lines. This could be associated with the heat treatment and cooling rate during the casting process. However, Samantaray et al. (2013) observed similar structure when working on microstructural evolution of 304L SS at different cooling temperatures. It was further confirmed that the primary ferrite solidification mode causes a continuous decrease in the size of the grains (Chen et al., 2010; Atwood et al., 2004). The grain size number according to ASTM E112-12 was approximately 6.04 for as-received 304L stainless steel. A decrease in grain size improves SCC resistance of austenitic stainless steels (Barnwell et al., 1966). The possible effect of this alloy to SCC is the presence of carbides which causes sensitisation leading to intergranular cracking, but refined grains will reduce this effect. As shown in Figure 4.1, the sample was free from precipitates because of the minimised sensitisation time. Sensitisation occurs when the precipitation of carbides depletes the chromium at grain boundaries in austenite stainless steel alloys. Rashid et al. (2012) reported that the precipitation formation was influenced by the sensitisation time. The enrichment of precipitation increased when sensitisation time was increased for more than ten seconds. The elemental composition of the as-received 304L stainless steel shown in Table B-1 was in accordance with the specification (Outokumbu, 2015), but minor deviations (±2% marginal error) were observed on silicon, phosphorus and manganese.

As it was expected, the microstructure of Ru laser alloyed 304L stainless steel had three zones, namely; the alloyed layer, HAZ and base metal. The other feature observed was the overlap zone and the overlapping was 60%. The microstructure was coarser at the overlap zone when compared to the alloyed layer. This is because of very high cooling rates of the alloyed layer during LSA process. The microstructure of the alloyed layer had refined grains

of approximately 9.4 µm in diameter. Similar structure of elongated fine grains of the alloyed layer was observed in all samples as shown in Figure 5.1. However, the microstructure of the overlap zone had courser grains with ASTM grains size number of approximately 8.2.
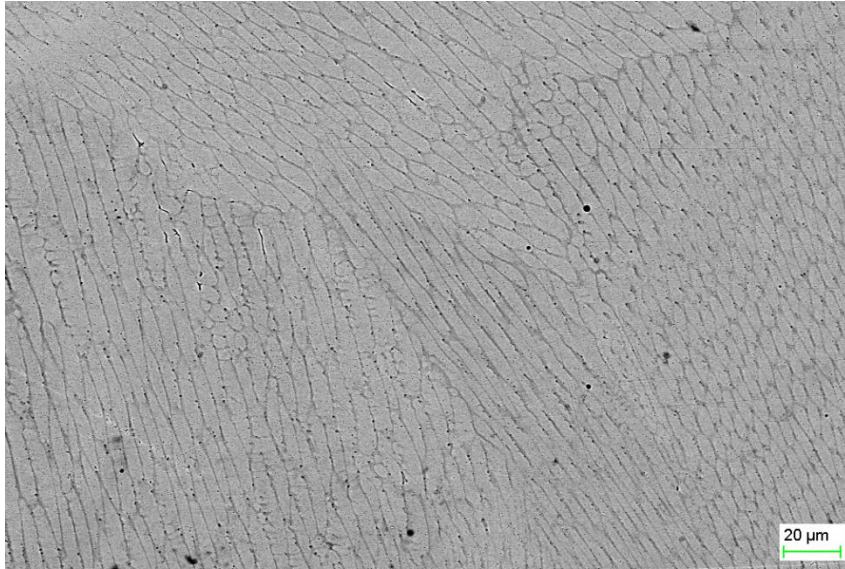
Figure 5.1: Cross-section microstructure of alloyed layer of LSA 304L SS with 0.98 wt% Ru.

The XRF analysis (Appendix B) showed chemical homogeneity of laser alloyed layers. The Ru content was homogeneously distributed over the alloyed layer despite small islands of undisssolved Ru on samples with 4.74 and 9.2 wt%. A metallurgical bond with no defects was observed at the laser clad and substrate interface. Columnar grains were observed on the alloyed layer. The thickness (approximately 950 µm) of the alloyed layer was the same for all LSA samples.

The microstructure of vacuum remelted samples had elongated grains. The elemental composition analysis shown in Table B-4 revealed slightly higher Ru content than what was expected in all samples. It was confirmed that annealing played a role on the microstructure of these alloys. However, the measured grain size number 6.4, of VAR samples was smaller than the one obtained for LSA samples (averaged G was 10.2) according to ASTM E112-12.

In this study, the refined grains of laser alloyed layer improved SCC resistance markedly. This correlated to literature where Barnwell et al. (1966) reported improvements in SCC

resistance of refined microstructure of austenitic stainless steel exposed to boiling magnesium chloride. Moreover, Ma et al. (2015) found that the microstructure and chemical composition influence SCC resistance of laser alloyed steels in sodium chloride containing sulphur dioxide. It was found that stress corrosion cracks initiate and propagate adjacent to the ferrite matrix and the samples were less resistant to SCC when compared to base metal.

5.2 Effect of Ru on SCC of laser alloyed samples

SCC cracks propagate differently based on the type of alloy and the environment. In the present study, the SCC crack initiation and propagation was evaluated for Ru enriched laser alloyed layers on 304L stainless steel in 50 ppm sodium chloride solution containing 10 ppm DO at 160°C.

The results presented in Section 4.3 showed that pits were the major contributing factor to initiate SCC cracks. Corrosion pits with hemispherical shape were formed on the surface of the alloyed layer. The formation of a pit could be related to chloride concentration and surface roughness. It was not possible to detect exactly the time at which the crack initiated from a pit, hence an assumption was made that a crack initiated immediately after experimental temperature (160˚C) was reached. This was based on Fontana (2005)'s relationship of temperature and time to crack of stainless steels. This assumption was essential for estimating the crack propagation rate of laser alloyed samples. A mixed mode (IGSCC and TGSCC) of cracking was observed on samples with 0.98 and 1.96 wt% Ru as shown in Figure 5.2. The cracks propagated from a region of high tensile stresses in a transgranular fashion and branched at grain boundaries (Figure 5.2). However, this was expected as literature (Kain et al., 2008; Nishimura, 2007; Vinoy et al., 1996) suggests that austenitic stainless steels are more likely to have mixed mode of cracking at high temperature above 150˚C.
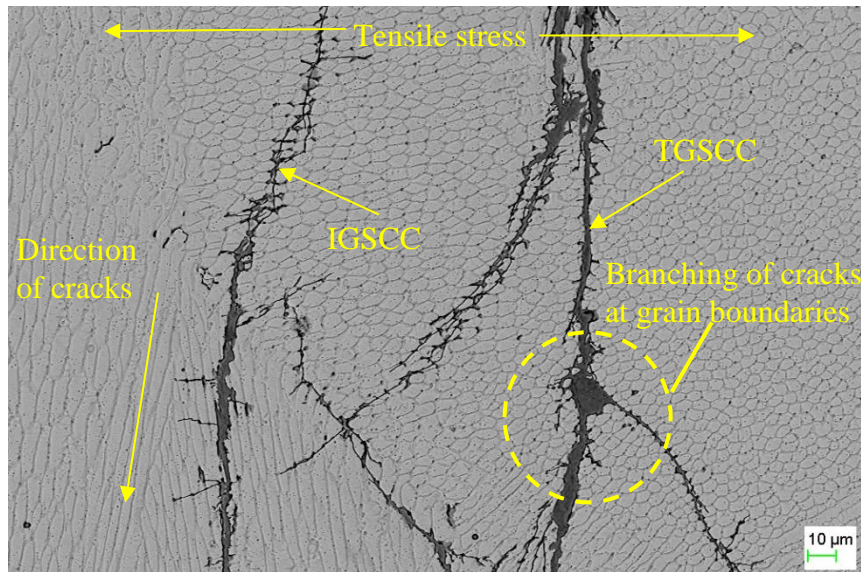
Figure 5.2: IGSCC and TGSCC of Ru (0.98 wt%) enriched laser alloyed layer on 304L SS after exposure to 50 ppm NaCl containing 10 ppm DO at 160°C for 172 hours.

The samples with 0 wt% Ru and as-received 304L SS showed SCC cracks initiating from pits and propagating only in a transgranular manner. This was in accord to the work reported by Yeh et al. (2013) on laser treated 304L stainless steel in pure water purged with oxygen at 280˚C. It should be noted in the present study that not all pits formed on the surface initiated cracking. The micro cracks initiated on the alloyed layer and coalesced leading to wider cracks of approximately 1-5 µm. It is suspected that a crack was arrested at the grain boundary and the dissolution took place. The widening of the crack tip promoted crack initiation as shown in Figure 5.3. The arrest and propagation of these cracks was witnessed as the grains became coarser. This type of cracking correlate very well to the proposed SCC mechanism (induce film rupture, absorption and localised dissolution) reported by previous researchers (Xie and Zhang, 2015; Lynch, 1989).
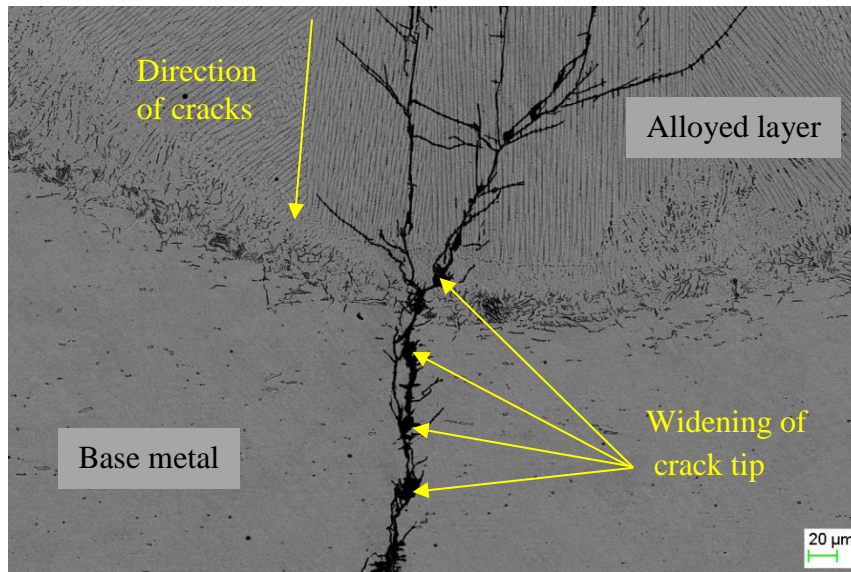
Figure 5.3: Coalescence of SCC cracks of laser surface alloyed 304L SS with 1.96 wt% Ru after exposure to 50 ppm NaCl and DO at 160°C for 172 hours.

The initiation of SCC crack can be associated with the electrochemical reaction on the surface of the metal and the presence of tensile stresses (Was and Andresen, 2007). Tensile stresses will destroy the protective layer allowing the dissolution at the crack tip and promoting faster crack propagation rate. The rate at which a crack grows is governed by the response of the protective film. If the rate at which the film is formed is lower than the crack growth rate, then the crack will propagate further. This confirms the analogy that high stresses will govern the mechanical process to initiate SCC cracks and low stresses will govern electrochemical process (Karpenko and Vaselenko, 1979). In the present study, a crack grew from a pit and branched across the boundary grains as shown in Figure 5.4. It was important to observe that some of the cracks were arrested at the grain boundaries surrounding the undissolved Ru island (Figure 5.4).
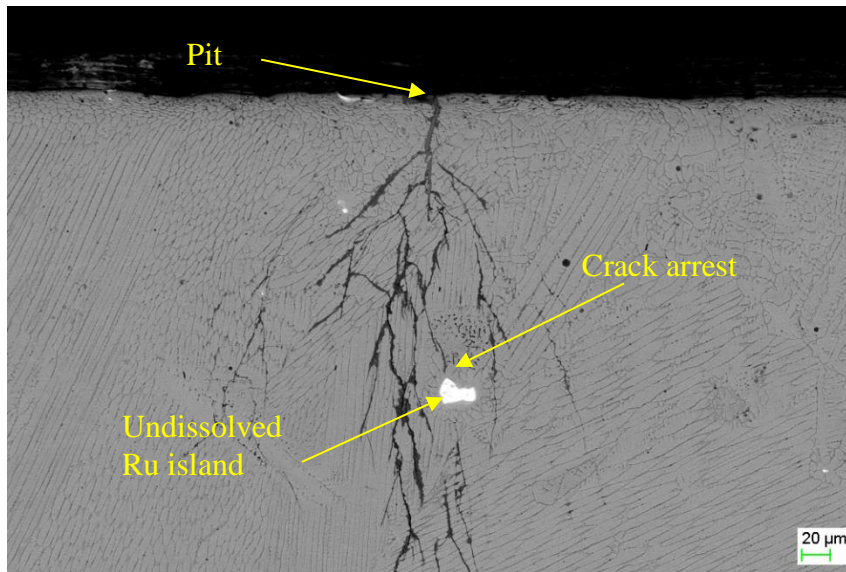
Figure 5.4: Crack arrest of 1.96 wt% Ru enriched laser alloyed layer on 304L SS after exposure to 50 ppm NaCl solution with 10 ppm DO at 160°C for 172 hours.

As reported in literature (Asabe et al., 2017; Barnwell et al., 1966) that a decrease in grain size improves SCC resistance, it was not surprising to observe a crack arrest by very fine grain structure as shown in Figure 5.5.
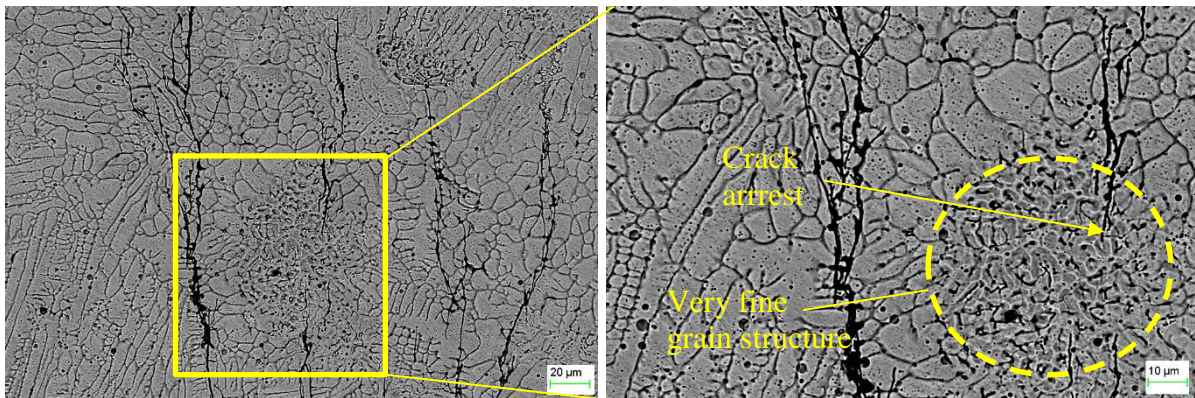
Figure 5.5: Crack arrest of very fine structure of 0.98 wt% Ru enriched laser alloyed layer on 304L SS after exposure to 50 ppm NaCl solution with 10 ppm DO at 160°C for 172 hours.

It was concluded by Holroyd and Scamans (2011) that the cracks are arrested if the grain size diameter is greater than the crack tip diameter for aluminium alloys exposed to moist air. This was in contrast to the work reported in this study because the stress corrosion cracks were arrested by very fine grains smaller than the crack tip diameter. Moreover, the cracks

arrested by the Ru island could be attributed to refined grains around this island. The samples with higher Ru content (4.74 and 9.2 wt%) were immune to SCC.

The stress corrosion cracks found on the laser alloyed samples could be classified into three groups: diagonal (45˚), perpendicular (90˚) and parallel (180˚) to applied tensile stress axis. Figure 5.6 shows a higher number of perpendicular cracks on as-received 304L stainless steel than laser alloyed sample with 0 wt% Ru. Most of SCC cracks were diagonal to tensile stresses for laser alloyed samples. This could be associated with residual stresses introduced during LSA process. Gamboa (2015) reported similar inclined cracks on steel gas pipeline to occur because of anisotropic residual stress.
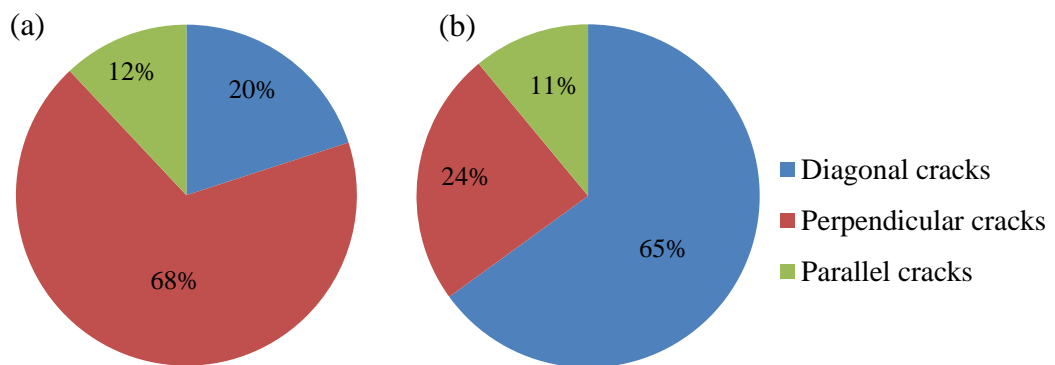
Figure 5.6: Classification of SCC cracks after exposure to 50 ppm NaCl with 10 ppm DO at 160˚C for 172 hours (a) as-received 304L SS (b) LSA 304L SS with 0 wt% Ru.

As the Ru content was increased, it was interesting to observe almost equal number of diagonal and parallel cracks as shown in Figure 5.7. It could be argued that perpendicular cracks effectively grow faster leading to catastrophic failure while diagonal or parallel cracks will take longer to fail.

94

(a)   (b)

30%   55%   43%   51%

15%   6%

■ Diagonal cracks
■ Perpendicular cracks
■ Parallel cracks
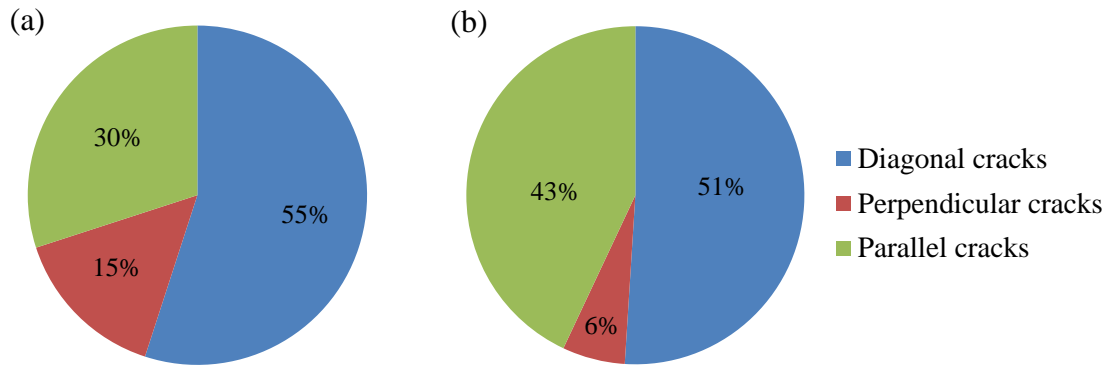
Figure 5.7: Classification of SCC cracks after exposure to 50 ppm NaCl with 10 ppm DO at 160˚C for 172 hours (a) LSA 304L SS with 0.98 wt% Ru (b) LSA 304L SS with 1.96 wt% Ru

The direction at which the cracks propagated have an effect on SCC failures hence laser surface alloying materials could be beneficial in eliminating or mitigating these failures. In this study, the additions of Ru improved the SCC resistance markedly. The crack density and crack growth rates were lower than those obtained for as-received 304L SS. It was interesting to observe a decrease in crack density as the Ru content increase. This was expected because of the refined microstructure on laser alloyed layer. The maximum and minimum crack density was 7 and 2 cracks/mm respectively. As shown in Figure 5.8, there was sudden decrease in crack growth rates as the Ru content was increased. The maximum crack growth rate was 7.3×10^{-6} mm/s and was found on samples with no Ru (i.e. 0 wt% Ru). The crack growth rate decreased to 3.2×10^{-6} mm/s for samples with 1.96 wt% Ru and there was no further cracking since the samples with 4.74 and 9.2 wt % Ru were immune to SCC.
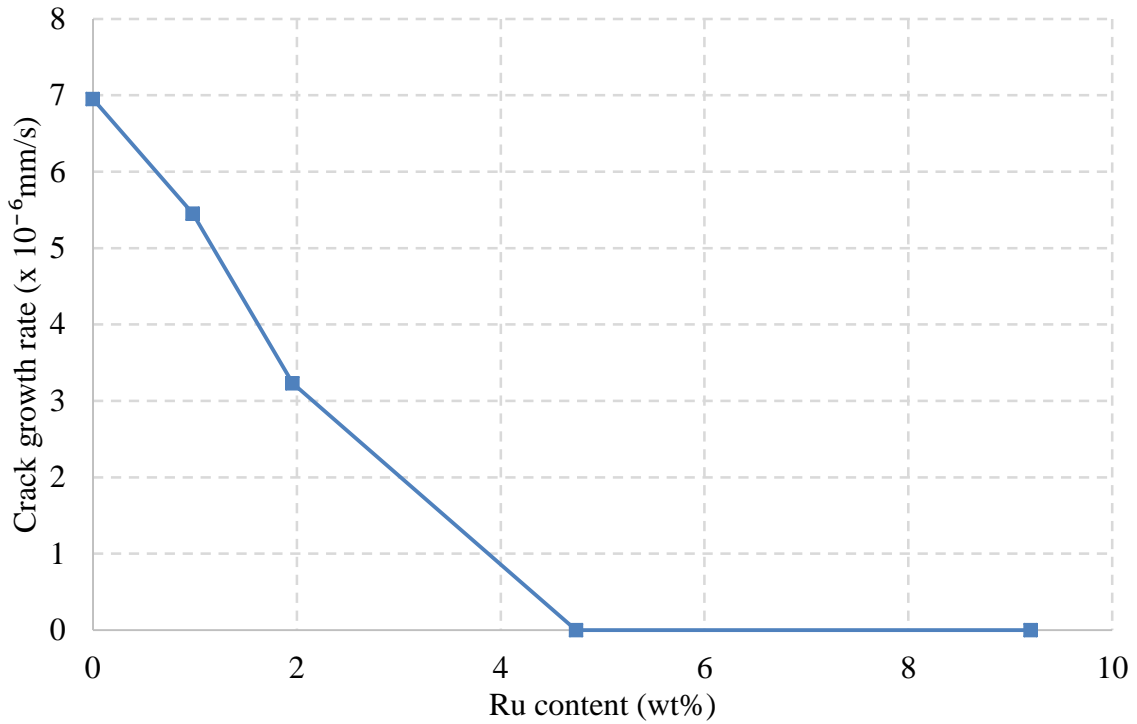
Figure 5.8: Effect of Ru content on crack growth rate after exposure to 50 ppm NaCl solution with 10 ppm DO at 160°C for 172 hours.

The rate at which cracks propagated on samples with 0 wt% Ru was closely similar to that of as-received 304L stainless steel (Table 4.1). However, these rates were lower when compared to those reported by Hsu et al. (2017) and Spencer et al. (2014) on 304L stainless steel exposed to NaCl solution at 80°C. Spencer et al. (2014) concluded that the crack propagation rates were influenced by the rate of diffusion of chloride ions at the crack tip. In this study, the cracks initiated from the alloyed layer and propagated half way through the transition layer into the base metal. It is believed that the crack propagated at the same rate through the alloyed zone and transition zone. Another interesting feature was observed at the overlap zone where there was no evidence of stress corrosion cracks in this zone. This indicated that SCC resistance of laser alloyed layer could be influenced by refined microstructure with grain size below 9.4 μm. However, Gosh and Kain (2010) found that the cracks were arrested by a ductile austenite phase matrix after exposure of 304L stainless steel samples in chloride environment.

SCC of welded sections can occur as a result of more than one crack propagation mechanism when exposed to a particular corrosive environment. The SCC susceptibility and morphology of cracking observed in this study can be associated with that reported by

previous authors (Zhang and Yang, 2014; Terachi et al., 2012; Shimomura and Nagumo, 2008). In the present study, the two SCC mechanisms were observed, the film rupture and localised dissolution. Initially a pit was formed on the surface and the presence of tensile stresses and chloride ions ruptured the oxide layer allowing the penetration of ions into fresh metal and leading to crack propagation. The cracks were discontinuous from the top of the clad through to the substrate. It was expected that stress corrosion cracks would initiate and propagate from a region of high tensile stress. Some of the SCC cracks initiated from the top surface of the clad and propagated through the alloyed layer where they appeared to be discontinuous when observed on the cross-section because of their branched nature. This type of cracking could be associated to three-dimensional crack propagation phenomenon studied by Zhu et al. (2013). The cracks that stopped propagating in the base metal can be attributed to the termination of the experiment.

5.3 SCC susceptibility of Ru vacuum remelted samples

The fractured surface of the vacuum remelted samples was investigated. The maximum stress threshold was 580 MPa and was observed on samples with 1.06 wt% Ru. These samples also took longer time to fracture and this proved that small additions of Ru improved SCC resistance. The samples with 2.07, 6.05 and 12.34 wt% Ru had lower time to failure. The failure time gradually decreased with increasing Ru level as shown in Figure 5.9. This was expected as the % elongation and % reduction in area followed similar trend line. It could be argued that optimum Ru additions (<1.07 wt %) is required to improve the SCC resistance of vacuum remelted samples in 50 ppm NaCl containing dissolved oxygen at 160°C.
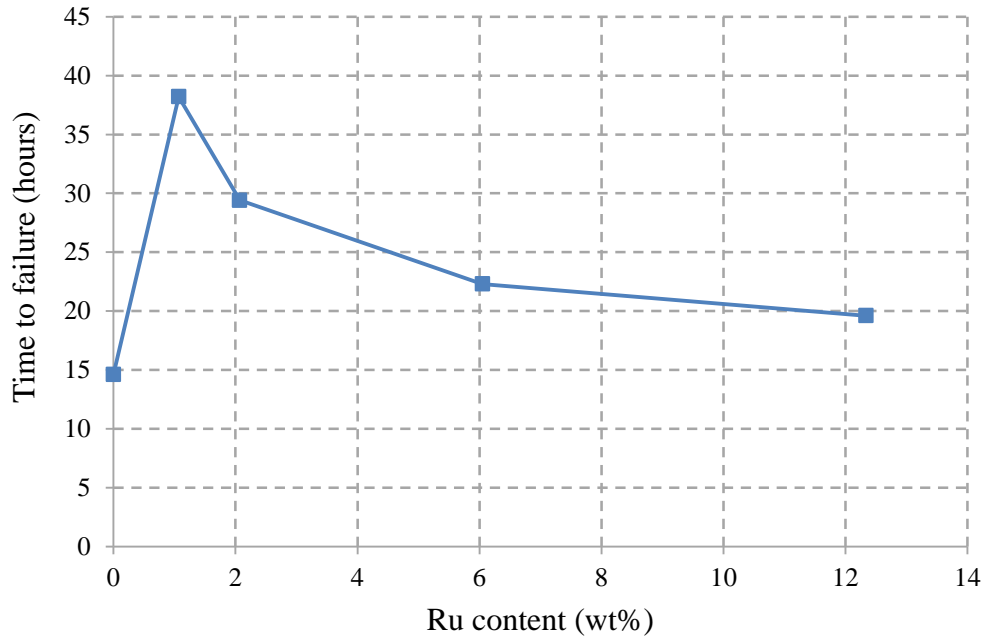
Figure 5.9: Effect of Ru on SCC time to failure in 50 ppm NaCl solution and 10 ppm DO at 160°C.

It was further evidenced by SEM micrographs (Figure 4.32 to Figure 4.37) that the higher Ru content lead to ductile failure mode. This was not expected and repetition of tests still showed a more ductile failure for these samples. There was no evidence of SCC cracks on the necking region of the samples with higher Ru content. Moreover, there was no evidence of hydrogen embrittlement cracking in all samples. This was consistent to the work reported by Hoke (1970) that vacuum remelted stainless steel was immune to hydrogen stress cracking. It should also be noted that laser clad samples were not tested using this technique because of the sample configuration which could not fit on the SSRT machine.

5.4 Corrosion behaviour at high temperatures

Electrochemical behaviour at high temperatures (i.e above 90°C) can be challenging because of the complications in the design of reference electrode. In this study, the reference electrode was designed in the laboratory as described in Section 3.4.3. The surface of laser alloyed samples (0, 0.98, 1.96, 4.74 and 9.2 wt % Ru) was exposed to an electrolyte and the polarisation data was recorded. The as-received 304L stainless steel was used as control alloy. As shown in Figure 5.10, the current density decreased as the Ru content was

increased up to 1.96 wt% for tests performed at room temperature, indicating the effectiveness of Ru to improve passivity which could also improve resistance to SCC.
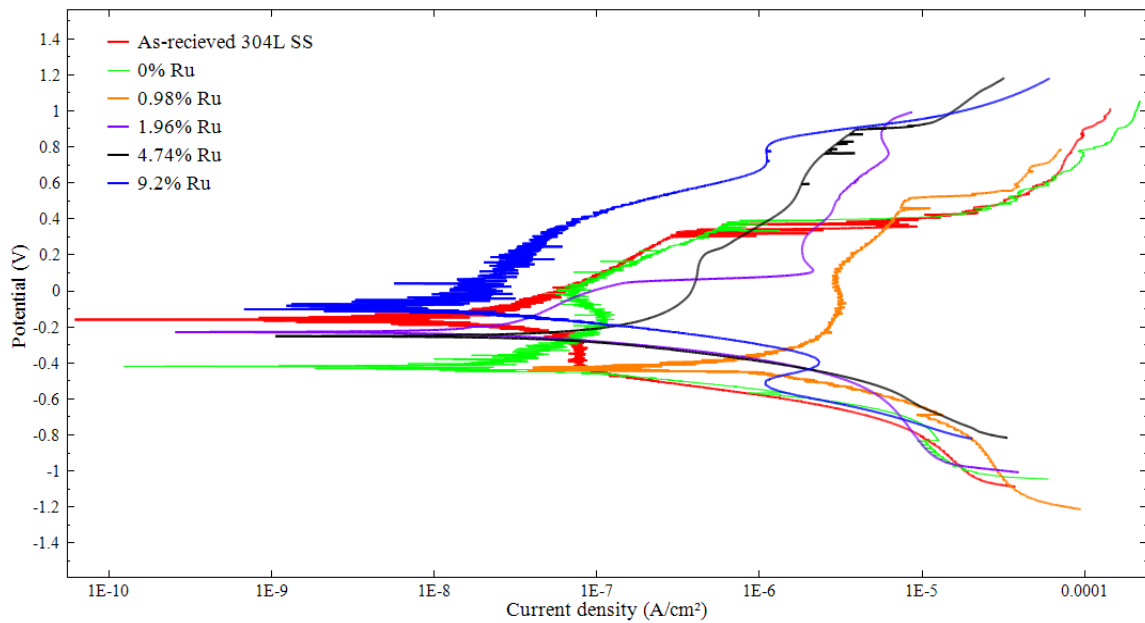
Figure 5.10: Potentiodynamic polarisation curve at samples at various Ru content in 50 ppm NaCl and 10 ppm DO at 25°C.

The potentiodynamic polarisation curve showed a sharp nose for samples with 1.96 wt% Ru. This could be attributed to the presence of chlorides promoting a more active region. However, both samples with 0.98 and 4.74 wt % Ru showed less of an active nose and a smooth transition to a pseudo-passive region. In comparison with the laser alloyed sample (0 wt% Ru) and the as-received 304L SS the i_{corr} decreased. The as-received sample did not show an active nose, but this was in clear contrast with the laser alloyed sample, which did have a significant active nose. The icorr of the laser alloyed sample was also slightly lower than the as-received sample, possibly indicating the improved corrosion resistance of the laser cladding. As indicated in Table 4.3, the i_{corr} of 0 wt% Ru samples and as-received 304L stainless steel was 10.2 and 18 µA/cm respectively. Therefore, heat treatment and microstructure has an influence in improving the corrosion resistance of 304L stainless steel. However, this could have been due to the addition of 2 wt% Ni as well in improving corrosion resistance. The results obtained in this study were consistent with those obtained by previous researchers (Van der Merwe and Tharandt, 2015; Olasande et al., 2012; Olubambi et al., 2009). The corrosion resistance improved since there was a gradual decrease in corrosion rates as the Ru level increased up to 1.96 wt % Ru. Thereafter there

was a sudden increase in corrosion rates as the Ru content was increased to 4.74 and 9.2 wt%.%. However, from the passivation current densities it is clear that the 9.2 wt% Ru sample was much lower than the other samples, and a significant drop occurred between the 9.2 wt% and 4.74 wt% samples. This decrease in passivation current densities would lead to the improved stress corrosion resistance found on these alloys.

The electrochemical behaviour of laser alloyed samples at elevated temperature (160°C) was significantly different from that observed at room temperature (25°C). At elevated temperatures, as shown in Figure 5.11, there was a distinct difference between the samples without Ru and those alloyed with Ru. The alloys without Ru did not have a passive region whereas the Ru alloyed samples did passivate. The passivity was clearly witnessed on samples with 0.98, 1.96, 4.74 and 9.2 wt% Ru. The sample with no Ru (i.e 0 wt% Ru and as-received 304L SS) did not show any evidence of passivity and the corrosion rates were high. The samples, 4.74 and 9.2 wt% Ru, showed clear passivation after an active nose region, and this definite passivation is probably why it was more resistant to stress corrosion than the other alloys.
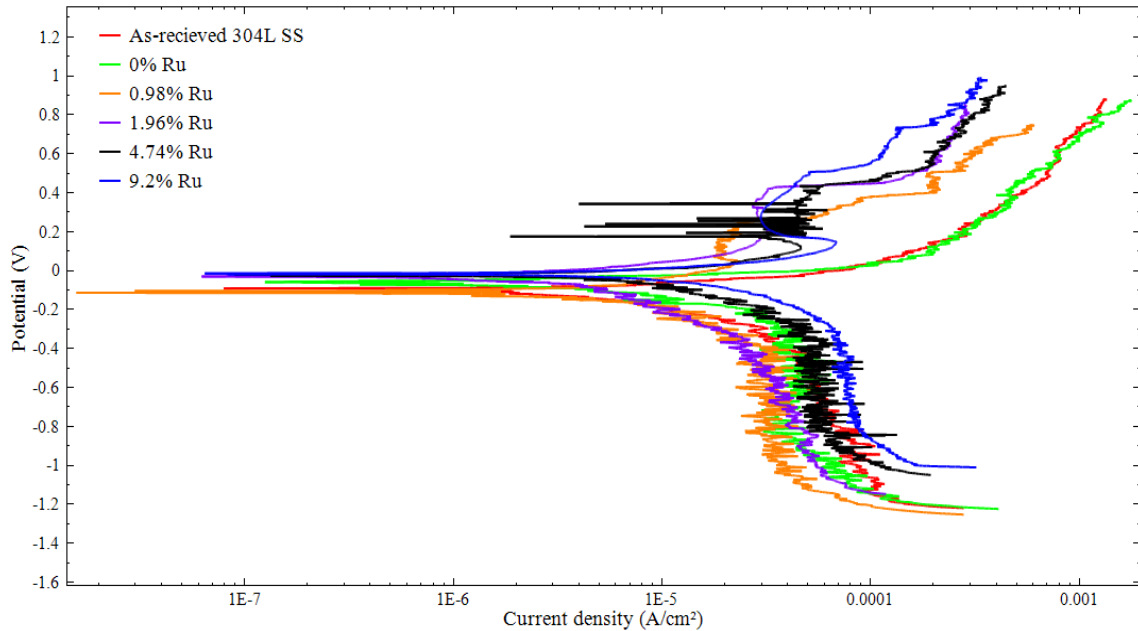
Figure 5.11: Potentiodynamic polarisation curve of laser alloyed samples at different Ru content in 50 ppm NaCl and 10 ppm DO at 160°C.

The passivity of austenitic stainless steel is mostly affected by the chromium content. In the present study, it was found that addition of Ru had a significant role in the passivity of the

laser alloyed 304L stainless steel at elevated temperatures. The samples with 0.98 wt% Ru showed double passivation in the passive and transpassive regions. The i_{crit} and E_{pass} for these samples was 23.4 μA/cm^2 and 50.1 mV respectively. At 1.96 wt% Ru the i_{crit} and E_{pass} was 31.9 μA/cm^2 and 198 mV respectively and there was no further repassivation in the transpassive zone for these samples. The E_{corr} of 1.96 wt % samples was -125 mV, which was slightly close to that obtained for samples with 0.98 wt % Ru (-105 mV). Similar electrochemical behaviour (passivity) was observed on samples with 4.74 and 9.2 wt% Ru at elevated temperature where i_{crit} was 46.4 μA/cm^2 and 67.9 μA/cm^2 respectively. The significant improvement in passive current density of the higher concentration Ru alloys shows the potential of these alloys to not only improve stress corrosion resistance, but also pitting resistance.

5.5 Cost analysis

It is important that every alloy developed is economically affordable and can meet the intended requirements. The cost analysis was performed for LSA samples and this was compared to the cost of commercial alloys (304L austenitic and 2507 duplex stainless steels).

The thickness of laser alloyed layer depends on the amount of powders used. In the present study, the average laser surface layer thickness was approximately 850 μm and the cost analysis performed was based on this thickness. To simplify the calculations, it was assumed that a laser clad was applied on a shaft of 100 mm diameter and 1500 mm long and the total cost was calculated using Equation 5.1 and recorded in Table 5.1. These calculations does not include LSA labour and equipment costs because this depends on the specific component design and configuration.

$$\text{Total cost} = \rho At (\omega_{Ru} \times C_{Ru} + \omega_{304} \times C_{304}) \tag{5.1}$$

$$= 7900 \times 0.47 \times 850 \times 10^{-6} (0.01 \times 2645 + 0.99 \times 332)$$

$$= \$1118.66$$

Where ρ is the density of 304 stainless steel in kg/m^3, A is the surface area in m^2, t is the required coating thickness in m, ω_{Ru} and ω_{304} is the weight percentage of Ru and 304

stainless steel powders respectively, C_{Ru} and C_{304} is the cost (\$/kg) of Ru and 304 powders respectively. The required total mass of powders to laser clad 850 µm thick layer was 3.16 kg. The price of Ru and Ni powders was 2645.00 USD/kg and 12.14 USD/kg respectively (infoMine, 2017), and the price of 304 stainless steel powder was 332 USD/kg (Sigma-Aldrich, 2017). It should be noted here that the cost of required Ni powder was very small relative to the Ru price, hence it was neglected in the calculations.

Table 5.1: Cost analysis of a 100mm diameter Ru laser alloyed 304L stainless steel shaft.

Samples	Required 304 stainless steel powder (kg)	Required Ru powder (kg)	Total cost (USD)	Total cost (ZAR)
304L+0% Ru	3.16	-	1 045.80	13 072.50
304L + 1% Ru	3.1284	0.0315	1 118.66	13 983.25
304L + 2% Ru	3.0870	0.0630	1 191.52	14 894.00
304L + 5% Ru	2.9925	0.1575	1 410.10	17 626.25
304L + 10% Ru	2.8350	0.3150	1 774.40	22 180.00
As-received 304L SS	-	-	1 484.43	18 555.37
2507 duplex stainless steel	-	-	5 750.50	71 881.25

Type 304L stainless steel shaft (cold rolled round bar) will cost \$1484.43 (Piyush Steel, 2017) which is slightly lower than laser treated shaft with 10 wt% Ru. The 304L stainless steel shaft cost more when compared to laser treated shaft with 0, 1, 2 and 5 wt% Ru. A similar shaft manufactured from highly corrosion resistant material such as 2507 duplex stainless steel will cost \$5750.50 (Piyush Steel, 2017). In essence, the coating of 304L stainless steel with Ru depends on the thickness of coating. An increase in thickness will increase the price. Even though the cost of Ru is higher, the benefits which come with the use of LSA are cost saving in the sense that maintenance costs could be reduced significantly.

Although the cost analysis of VAR samples was beyond the scope of this work. It could be argued that VAR technique will be costly to run because of the alloying process. The

difference here is that the thickness of the clad is not required. Both techniques can be used to improve SCC corrosion resistance but limitations are on the effectiveness of the technique. LSA is more effective and advantageous to use in a sense that a specific metallic component in a machine can be cladded without removing it from the system or dismantling the system. Whereas VAR will require the component to be removed and be placed in a furnace where it is remelted with the alloying powder. However this method can be advantageous over LSA if many parts in a system/machine are to be alloyed. All components/parts will be remelted and machined again and the drawback is that it will require more time than LSA technique.

High corrosion resistance alloys such as duplex stainless steels and hastelloys are usually considered to be used in harsh corrosive environments at elevated temperature. But the exorbitant cost of these alloys limit the use in many industries. Hence laser surface alloying existing components will be the method to use in order to improve SCC resistance of components than replacing them with new costly ones.

CHAPTER 6

CONCLUSIONS AND RECOMMENDATIONS

6.1 Conclusions

The Ru laser alloyed layers of 304L stainless steel were investigated for SCC. Optical and SEM were used to analyse samples prior and after exposure to a corrosive environment at 160°C. The experimental results revealed improvements to SCC resistance when Ru was added. The conclusions from the discussed sections on the microstructure, hardness, SCC and electrochemical behaviour of Ru alloyed 304L stainless steel were drawn as follows;

- The laser cladded samples consisted of three zones, namely the alloyed layer, HAZ and base metal. Prior to exposure, no defects were found on the alloyed layer, indicating a good adhesion and a sound metallurgical bond between the alloyed layer and the base metal. The grains of the alloyed layer were refined and averaging to a grain size number (G) of 10.5 according to ASTM E112-12. There was slight difference in grain size number when the Ru level was increased.

- The microstructure of VAR samples had elongated grains along the rolling direction. The average grain size number achieved was 6 according to ASTM E112-12. The samples were free from precipitates and the Ru content was homogeneously distributed.

- The microhardness increased significantly as the Ru content was increased. The highest hardness was 250 HV and this was for laser alloyed samples with 9.2 wt% Ru. The microhardness of vacuum remelted samples also increased with increasing Ru content and maximum hardness was 169 HV.

- Most cracks initiated from pits on the stressed samples in sodium chloride solution with dissolved oxygen. The presence of tensile stresses and chloride ions ruptured the oxide layer allowing the exposure of the fresh metal and leading to localised corrosion and eventually to crack propagation.

- Laser surface alloyed layers of Ru enriched 304L stainless steel showed improved SCC resistance when the Ru content was increased. The samples with 0, 0.98 and 1.96 wt % were susceptibility to SCC but these samples had lower crack propagation rates when compared to as-received 304L stainless steel. The samples with 4.74 and 9.2 wt% Ru were immune to SCC.

- The stress corrosion cracks were evidenced on the alloyed layer, HAZ and base metal. A mixed mode of crack propagation (IGSCC and TGSCC) was observed on laser alloyed samples with 0.98 and 1.96 wt% Ru. Some of the cracks branched at the grain boundaries and propagated along the grains. The cracks observed on samples with 1.96 wt% Ru widened at the crack tip and propagated again. The cracks coalesced in the alloyed layer and propagated through the transition zone. The proposed SCC mechanism for this type of cracking was film rupture and dissolution.

- It was evident that stress corrosion cracks become more diagonal to tensile stress direction when the Ru content was increased. However, the crack density decreased with increasing Ru level and this was associated with refined microstructure in the alloyed layer. The crack arrest was observed on the very fine grain structure in the alloyed layer of samples with 0.98 and 1.96 wt % Ru. These arrests were also evidenced at the refined microstructure surrounding the undissolved Ru island.

- The maximum stress threshold of VAR samples was 580 MPa and it was found on alloys with 1.07 wt% Ru content. There was an increase in elongation and reduction area when 1.07 wt% Ru was added, thereafter gradually decrease with further additions of Ru.

- The electrochemical results showed an improved corrosion resistance with additions of Ru. The corrosion rates decreased as the Ru content was increased only up to 1.96 wt% and thereafter there was a gradual increase in corrosion rates for samples with 4.74 and 9.2 wt%. The corrosion rates of laser treated samples were lower when compared to as-received 304L stainless steel.

- There was passivation on samples with 0.98, 1.96, 4.74 and 9.2 wt % Ru at elevated temperature (160°C) in sodium chloride containing dissolved oxygen, and no

evidence of passivity was witnessed on Ru free samples (i.e 0 wt% Ru and as-received 304L stainless steel).

6.2 Recommendations for Future work

- The three-dimensional morphology of stress corrosion cracks of laser alloyed samples should be investigated to further understand the nature of cracking and the influence of chloride ions and tensile stresses on crack propagation. In addition, the kinetics of pit initiation and propagation has to be investigated to understand its role in initiating a crack.

- Other techniques such as XRD should be employed to investigate the phase of laser alloyed and vacuum remelted sample and corrosion products after exposure of samples to a corrosive environment at elevated temperatures. EBSD could be used for further analysis of stress corrosion cracks.

- The laser cladded cylindrical samples should be investigated to understand the effect of Ru to failure time, % elongation and %reduction area.

REFERENCES

Ahmad, Z. 2006. *Principle of corrosion engineering and corrosion control*. Oxford: Elsevier.

AK Steel. 2015. Typical room temperature mechanical properties of stainless steel. [Online]. [Accessed 13 July 2015]. Available from: http://www.aksteel.com/.

ALD. 2016. Vacuum arc remelting processes and furnaces. [Online]. [Accessed 25 January 2016]. Available from: https://www.ald-web.de/en/.

Alyousif, O.M. and Nishimura, R. 2006. The effect of test temperature on SCC behavior of austenitic stainless steels in boiling saturated magnesium chloride solution. *Corrosion Science*. **48** (2006), pp.4283-4293.

Amende, W. and Nowak, G. 1990. Hard phase particles in laser processed cobalt rich claddings. *ECLAT*., pp.417-428.

Asabe, T., Rifai, M., Yuasa, M. and Miyamoto, H. 2017. Effect of grain size on the stress corrosion cracking of ultrafine grained Cu-10 wt% Zn alloy in ammonia. *International Journal of Corrosion*. **2017**.

Atwood, R.C., Lee, P.D., Minisandram, R.S. and Jones, R.M.F. 2004. Multiscale modelling of microstructure formation during vacuum arc remelting of titanium 6-4. *Journal of Materials Science*. **39**(24), pp.7193-7197.

Barnes, A., Senior, N. and Newman, R.C. 2008. Revisiting the film-induced cleavage model of SCC *In*: *Environment-Induced Cracking of Materials*., pp. 47-57.

Barnwell, V.L., Myers, J.R. and Saxer, R.K. 1966. Effect of grain size on stress corrosion of Type 302 austenitic stainless steel. *Corrosion*. **22**(9), pp.261-264.

Barsanti, L., Cabrini, M., Pastore, T. and Spinelli, C. 2008. Effect of microstructure on the hydrogen-embrittlement behaviour of HSLA steels under cathodic protection *In*:

Environment-Induced Cracking of Materials., pp. 279-289.

Basson, J. and Wicker, C. 2002. Environmentally induced transgranular stress-corrosion cracking of 304l stainless steel components at Koeberg. *In Contribution of materials investigation to the resolution of problems encountered in pressurized water reactors*.

Bax, B., Pauly, C., Leibenguth, P., Woll, K. and Mücklich, F. 2012. Synthesis of B2-RuAl coatings on mild steel by laser cladding. *Surface and Coatings Technology*. **206**(19-20), pp.3931-3937.

Beachem 1972. A new model for a hydrogen assisted cracking (Hydrogen Embrittlement). *Metallurgical Transactions*. **3**(1), pp.437-451.

Bergmann, H.. 1994. Industrial applications of surface treatments with high power lasers. *Materials science forum*. **163**, pp.377-404.

Bhattacharya, A. 2008. Stress Corrosion cracking of duplex stainless steels in caustic solutions. PhD thesis, Georgia Institute of Technology.

Bosch, R.W., Bogaerts, W.F. and Zheng, J.H. 2003. Simple and robust external reference electrodes for high-temperature electrochemical measurements. *Corrosion*. **59**(2), pp.162-171.

Bramfitt, B.L. and Benscoter, A.O. 2002. *Metallographer's guide: practice and procedures for irons and steels*. USA: ASM International.

Brinkman, C. and Gavin, H. 1979. *Properties of austenitic stainless steel and their welds*. ASTM.

Bruck, G.. 1988. Fundamentals and industrial applications of high power laser beam cladding, laser beam surface treating and coating. *SPIE*. **957**(14), p.28.

Bruemmer, S.M. and Thomas, L.E. 2008. Insights into stress corrosion cracking mechanisms from high-resolution measurements of crack-tip structures and compositions *In*:

Environment-Induced Cracking of Materials. Richland, pp. 95-106.

Brytan, Z., Bonek, M. and Dobrzański, L. 2010. Microstructure and properties of laser surface alloyed PM austenitic stainless steel. *Journal of Achievements in Materials and Manufacturing Engineering*. **40**(1), pp.70–78.

BSSA 2017. Stress relieving heat treatments for austenitic stainless steels. *British Stainless Steel Association*. [Online]. [Accessed 21 August 2017]. Available from: http://www.bssa.org.uk/.

Bueno, A.H.S., Castro, B.B. and Ponciano, J.A.C. 2008. Assessment of stress corrosion cracking and hydrogen embrittlement susceptibility of buried pipeline steels *In*: *Environment-Induced Cracking of Materials*, pp. 313-322.

Cabrini, M., Lorenzi, S., Pastore, T., Pellegrini, S., Burattini, M. and Miglio, R. 2017. Study of the corrosion resistance of austenitic stainless steels during conversion of waste to biofuel. *Materials*. **10**(3), p.325.

Calcagnotto, M., Ponge, D., Adachi, Y. and Raabe, D. 2009. Effect of grain refinement on strength and ductility in dual-phase steels. *Proceedings of the 2nd International Symposium on Steel Science*,pp.1-4.

Chapelle, P., Bellot, J.P., Duval, H., Jardy, A. and Ablitzer, D. 2001. Modelling of plasma generation and expansion in a vacuum arc: application to the vacuum arc remelting process. *Journal of Physics Applied Physics*. **35**(2), pp.137-150.

Chen, S.T., Tang, W.Y., Kuo, Y.F., Chen, S.Y., Tsau, C.H., Shun, T.T. and Yeh, J.W. 2010. Microstructure and properties of age-hardenable AlxCrFe1.5MnNi0.5 alloys. *Materials Science and Engineering*. **527**(21-22), pp.5818-5825.

Cobb, H. 2010. *The History of Stainless Steels*. ASM International.

Cohen, H. 2013. NDK explosion resulted from stress corrosion cracking of high pressure vessel. [Online]. [Accessed 25 April 2015]. Available from: http://www.csb.gov/csb-finds-

fatal-2009-ndk.

Copson, H.R. 1989. *Effect of composition on SCC of some alloys containing nickel. Physical metallurgy of stress corrosion fracture*. New York, USA.

Copson, H.R. 1956. Laboratory technigues for the investigation of stress corrosion cracking *In*: W. Robertson, ed. *Stress corrosion cracking and embritlement*. John Wiley and Sons, pp. 187–190.

Cotton, S. 1997. *Chemistry of Precious Metals* First. London, UK: Blackie Academic and Professional.

Cunat, P. 2004. *Alloying elements in stainless steel and other chromium-containing alloys*. Paris, France: Internationa Chronium Development Association.

Davies, J. 2000. *Corrosion: understanding the basics*. Ohio, USA: ASM International.

Degerbeck, J. and Wold, E. 2004. Some aspects of the influence of manganese in austenitic stainless steels. *Materials and corrosion*. **25**(3), pp.172-174.

Delaunois, F., Tshimombo, A., Stanciu, V. and Vitry, V. 2016. Monitoring of chloride stress corrosion cracking of austenitic stainless steel: Identification of the phases of the corrosion process and use of a modified accelerated test. *Corrosion Science*. **110**,pp.273–283.

Dieter, G. 1961. *Mechanical metallurgy*. New York, USA: McGraw-Hill.

Draper, C.W. and Poate, J.M. 1985. Laser surface alloying. *International Materials Reviews*. **30**(1), pp.85-108.

Edeleanu, C. 1953. Transgranular stress corrosion in chromium nickel stainless steel. *Journal of the Iron and Steel Institute*. **174**(1), pp.218-218.

Eiselstein, H. 1965. Metallurgy of a Cb hardened Ni-Cr-Fe alloy, Advances in the technology of stainless steel and related alloys. *ASTM*. **369**, pp.62-79.

Fontana, M.G. 2005. *Corrosion engineering*. New York, USA: Tata McGraw-Hill.

Gamboa, E. 2015. Inclined stress corrosion cracks in steel pipelines. *Corrosion Engineering, Science and Technology*. **50**(3), pp.191-195.

Gangloff, R. 2003. Hydrogen assisted cracking of high strength alloys.

Gati, K.H., Ja, H.I. and Alsammarraie, A.M.A. 2017. Effect of stress on SCC susceptibility of low carbon steel in 0.1M of sulphuric acid solution using tension test. *Corrosion engineering, Science and Technology*.,pp.1-4.

Ghosh, S. and Kain, V. 2010. Microstructural changes in AISI 304L stainless steel due to surface machining: Effect on its susceptibility to chloride stress corrosion cracking. *Journal of Nuclear Materials*. **403**(1–3), pp.62-67.

Gilchrist, R. 1943. The platinum metals. *Chemical Reviews*. **32**(3), pp.277-372.

Govender, K., Scenini, F., Lyon, S. and Sherry, A. 2012. Influence of Pd and Ru additions on stress corrosion cracking of austenitic stainless steels. *Corrosion Engineering, Science and Technology*. **47**(7), pp.507-515.

Gutman, E.M., Solovioff, G. and Eliezer, D. 1996. The mechanochemical behavior of type 316L stainless steel. *Corrosion Science*. **38**(7), pp.1141-1145.

Hills, R.F., Howlett, B.W. and Butcher, B.R. 1965. The effect of cooling rate and composition on the transformation of the gamma-phave in uranium ruthenium alloys (With an appendix on ruthenium as a grain refining element). *Journal of Nuclear Materials*. **16**, pp.109-128.

Hilti 2014. Corrosion Resistant Fastening. [Online]. [Accessed 23 March 2014]. Available from: http://www.hiltiegypt.com/fstore/holus/LinkFiles/hilti_corrosion_resistant_fastening_manual.pdf.

Holroyd, N.J.H. and Scamans, G.M. 2011. Crack propagation during sustained-load cracking

of Al-Zn-Mg-Cu aluminum alloys exposed to moist air or distilled water. *Metallurgical and Materials Transactions A: Physical Metallurgy and Materials Science*. **42**(13), pp.3979-3998.

Hsu, C.H., Chen, T.C., Huang, R.T. and Tsay, L.W. 2017. Stress corrosion cracking susceptibility of 304L Substrate and 308L weld metal exposed to a salt spray. *Materials*. **10**(2), pp.1-14.

Huang, L., Huaiqui, Z., Zhang, F. and Xiaowei, W. 2015. Effect of Temperature on the Stress Corrosion Cracking of 304L Austenitic stainless steels in alkaline solution. *Materials Science Forum*. **809**, pp.354-357.

Ion, J.C. 2005. *Laser Processing of engineering materials; principles, procedure and industrial applications*. Butter-Heinemann.

James, E. and McBreen, E. 1954. *Platinum group metals, minerals year book metals and minerals*.

Jianglong, L., Qiquan, L. and Zhirong, Z. 1993. Laser gas alloying of titanium alloy with nitrogen. *Surface and Coatings Technology*. **57**(2–3), pp.191-195.

John, C. 2014. The role of alloying elements on fabricability of austenitic stainless steel. [Online]. [Accessed 23 March 2014].Available from:
http://www.csidesigns.com/uploads/white-papers/fabtech.pdf.

Juang, H.K. and Altstetter, C. 2012. Effect of pH and chloride contents on stress corrosion cracking of austenitic stainless steels at room temperature. *Corrosion*. **46**(11), pp.881-887.

Kain, V., Samantaray, R., Acharya, S., De, P.K. and Raja, V.S. 2008. Influence of low-temperature sensitization on stress corrosion cracking of 304LN stainless steels *In*: *Environment-Induced Cracking of Materials*., pp. 163-172.

Kaneko, M. 2007. Stress corrosion cracking of stainless steels. *Welding International*. **21**(2),pp.95–99.

Kim, K.., Zhang, P.Q. and Lee, Y.. 1998. Electrochemical and stress corrosion properties of duplex stainless steels modified with tungsten addition. *Journal of Corrosion Science*. **54**(11), pp.910-921.

Kingston, T. 2013. The Flixborough explosion-United Kingdom.[Online]. [Accessed 23 August 2015]. [Available from: http://blog.nationalarchives.gov.uk/blog/flixborough-1-june-1974/.](http://blog.nationalarchives.gov.uk/blog/flixborough-1-june-1974/)

Klar, E. and Samal, P. 2007. Powder metallurgy stainless steels, processing microstructures and properties. *ASM International*. [Online]. [Accessed 12 January 2015]. Available from: https://books.google.co.za/books.

Kou, S., Poirer, D. and Flemings, M. 1977. Macrosegregation in electroslag remelted ingots. *Electric Furnace Procedings*. **35**, p.221.

Kowaka, M. and Yamanaka, K. 1981. Effect of Alloying Elements of Austenitic Stainless Steels on Chloride Stress Corrosion Cracking by Fracture Mechanics. In Metallic Corrosion. 8 th International Congress on Metallic Corrosion. 1,pp.512–517.

Kumar, D., Sridhar, K., Biswas, a. R., Goswami, G.L. and Deshmukh, M.B. 1993. Characterization of laser produced high molybdenum surface alloys on stainless steel substrates. *Journal of Laser Applications*. **5**(2-3),pp.23-32.

Kwok, C. and Wong, P. 2010. Laser surface alloying of various engineering alloys for sliding wear and corrosion resistance. *Journal of Laser Micro/Nanoengineering*. **5**(1), pp.90-93.

Lancaster, J.F. 1980. *Metallurgy of Welding* third. Sydney: George Allen and Unwin.

Landolt, D. 2007. *Corrosion and Surface Chemistry of Metals*. Lausanne, Switzerland: CRC Press.

Leet, H. and Uhkig, H. 1970. Effect of Nickel in Cr-Ni Stainless steel on the critical potential of stress corrosion cracking. *Electrochemical Society*. **117**(1),pp.18-22.

Lekala, M.B., Van Der Merwe, J.W. and Pityana, S.L. 2012. Laser surface alloying of 316l stainless steel with Ru and Ni mixtures. *International Journal of Corrosion*. **2012**, pp.1-5.

Lewis, C. 2015. Westinghouse and Eskom holdings judgement. [Online]. [Accessed 12 December 2015]. Available from: http://www.politicsweb.co.za/documents/westinghouse-vs-eskom--areva-sca-judgment.

Liang, D., Sowards, J.W., Frankel, G.S., Alexandrov, B.T. and Lippold, J.C. 2010. Corrosion resistance of welds in type 304L stainless steel made with a nickel-copper-ruthenium welding consumable. *Corrosion Science*. **52**(7), pp.2439-2451.

Lu, B.T., Luo, J.L. and Norton, P.R. 2010. Environmentally assisted cracking mechanism of pipeline steel in near-neutral pH groundwater. *Corrosion Science*. **52**(5), pp.1787-1795.

Lu, B.T., Luo, J.L., Norton, P.R. and Ma, H.Y. 2009. Effects of dissolved hydrogen and elastic and plastic deformation on active dissolution of pipeline steel in anaerobic groundwater of near-neutral pH. *Acta Materialia*. **57**(1), pp.41-49.

Lvov, S., Balashov, V. and Fedkin, M. 2005. *Electrochemical corrosion in high temperature sub- and supercritical water*. Penn State.

Lynch, S.P. 1988. Environmentally assisted cracking: Overview of evidence for an adsorption-induced localised-slip process. *Acta Metallurgica*. **36**(10), pp.2639-2661.

Lynch, S.P. 1989. Metallographic contributions to understanding mechanisms of environmentally assisted cracking. *Metallography*. **23**(2), pp.147-171.

Ma, G. and Ling, X. 2013. Effect of temperature and chloride content on the stress corrosion cracking susceptibility of 304 stainless steel welded joints treated by ultrasonic impact treatment. *Journal of Pressure Vessel Technology*. **135**(5), p.51501.

Ma, H.C., Liu, Z.Y., Du, C.W., Wang, H.R., Li, X.G., Zhang, D.W. and Cui, Z.Y. 2015. Stress corrosion cracking of E690 steel as a welded joint in a simulated marine atmosphere containing sulphur dioxide. *Corrosion Science*. **100**, pp.627-641.

Malkin, A.I., Polukarova, Z.M., Zanozin, V.M., Lebedev, B.D., Petrova, I. V and Shchukin, E.D. 2008. Liquid metal embrittlement of superplastic alloys *In*: *Environment-Induced Cracking of Materials*., pp. 497-504.

Mandel, C. 2015. Why Corrosion Might Take Down Energy East. [Accessed 21 August 2015]. Available from: http://www.nationalobserver.com/2015/09/04/news/why-corrosion-might-take-down-energy-east.

Van Der Merwe, J. and Tharandt, D. 2015. Corrosion resistance of laser-cladded 304L stainless steel enriched with ruthenium additions exposed to sulphuric acid and sodium chloride media. *Journal of the Southern African Institute of Mining and Metallurgy*. **115**(6), pp.499-505.

Metal AM. 2014. Advanced manufacturing.[Online]. [Accessed 12 April 2014]. Available from: http://www.metal-am.com/introduction-to-metal-additive-manufacturing-and-3d-printing/metal-additive-manufacturing-processes/.

Mintz, T. 2013. Coastal salt effects on the stress corrosion cracking of type 304 stainless steel. [Online]. [Accessed 30 November 2015]. Available from: http://www.nace.org/cstm/PaperTrail/Authors/Submission.aspx?id=2e9e8313-3bab-e111-ac69-0050569a007e.

Morris, J.W. 2001. *The influence of grain size on the mechanical properties of steel*. Berkeley, USA.

Mudali, K., Kaul, R., Ningshen, S., Ganesh, P., Nath, A.K., Khatak, H.S. and R., B. 2006. Influence of laser surface alloying with chromium and nickel on corrosion resistance of type 304l stainless steel. *Journal of Materials Science and Technology*. **22**(10), pp.1185-1192.

Mudali, U.K. and Pujar, M.G. 2002. Pitting Corrosion of Austenitic Stainless Steels and their Weldments *In*: *Corrosion of Austenitic Stainnless Steel, Mechanism, Migitation and Monitoring*. Pangbourne, England: Alpha Science International Ltd, pp. 74-80.

Nielsen, D. 2006. *Practical Handbook of Environmental Site Characterisation and Ground*

Water Monitoring. CRC Press.

Nishimura, R. 2007. Characterization and perspective of stress corrosion cracking of austenitic stainless steels (type 304 and type 316) in acid solutions using constant load method. *Corrosion Science*. **49**, pp.81-91.

Nishimura, R. and Maeda, Y. 2004. Stress corrosion cracking of type 304 austenitic stainless steel in sulphuric acid solution including sodium chloride and chromate.**46**, pp.343-360.

NPL. 2016. Guides to good practice in corrosion control: Stress corrosion cracking.[Online]. [Accessed 23 April 2016]. Available from: http://www.npl.co.uk/upload/pdf/stress.pdf.

Outokumbu 2015. High Performance Stainless Steel. .[Online]. [Accessed 23 April 2016]. Available from: https://www.outokumpu.com/en/Pages/default.aspx.

Pawlowski, L. 1999. Thick laser coating. *Journal of Thermal Spray Technology*. **8**(2).

Piyush Steel 2017. Price list.[Online]. [Accessed 20 October 2017]. Available from: http://www.piyushsteel.com/blog/price-list-of-stainless-steel-pipes-tubes/.

Potgieter, J.H. and Brookes, H.C. 1995. Corrosion behavior of a high-chromium duplex stainless steel with minor additions of ruthenium in sulfuric acid. Corrosion, **51**(4), pp.312-320.

Potgieter, J.H., Thomson, J., Adams, F. V and Afolabi, A.S. 2014. Effect of additions of Ru and Pd on the electrochemical behaviour of austenitic stainless steel in organic acids. *International Journal of Electrochemical Science*. **9**(11), pp.6451-6463.

Potgieter, J.H., Thomson, J., Adams, F.V. and Afolabi, A. 2014. Effect of additions of Ru and Pd on the electrochemical behavior of austenitic stainless steel in organic acids. *International Journal of Electrochemical Science*. **9**(1), pp.6451-6463.

Prosek, T., Le Gac, A., Thierry, D., Le Manchet, S., Lojewski, C., Fanica, A., Johansson, E.,

Canderyd, C., Dupoiron, F., Snauwaert, T., Maas, F. and Droesbeke, B. 2014. Low temperature stress corrosion cracking of austenitic and duplex stainless steels under chloride deposits. *Corrosion*. **70**(10), pp.1052-1063.

Puiggali, M., Zielinski, A., Olive, J.M., Renauld, E., Desjardins, D. and Cid, M. 1998. Effect of microstructure on stress corrosion cracking of an Al-Zn-Mg-Cu alloy. *Corrosion Science*. **40**(4–5), pp.805-819.

Raman, R. and Siew, W. 2014. Stress corrosion cracking of an austenitic stainless steel in nitrite-containing chloride solutions. *Materials*. **7**(12), pp.7799-7808.

Rashid, M.W.A., Gakim, M., Rosli, Z.M. and Azam, M.A. 2012. Formation of Cr23C6 during the sensitization of AISI 304 stainless steel and its effect to pitting corrosion. *International Journal of Electrochemical Science*. **7**(10), pp.9465-9477.

Safiuddin, M. and Ahammad, A. 2016. Environmentally induced stress corrosion cracking.

Saluja, R. and Moeed, K.M. 2012. The emphasis of phase transformations and alloying constituents on hot cracking susceptibility of type 304L and 316L stainless steel welds. *International Journal of Engineering Science and Technology*. **4**(5), pp.2206-2216.

Samantaray, D., Kumar, V., Bhaduri, K. and Dutta, P. 2013. Microstructural evolution and mechanical properties of type 304 l stainless steel processed in semi-solid state. *International Journal of Metallurgical Engineering*. (2), pp.149-153.

Scenini, F., Govender, K., Lyon, S. and Sherry, A. 2012. Stress corrosion cracking of Ru doped 304 stainless steel in high temperature water. *Corrosion Engineering, Science and Technology*, **47**(7). pp. 498-506.

Schweitzer, P.A. 2013. *Fundamentals of Corrosion-Mechanisms, Causes, and Preventative Methods*. Boca Raton, USA: CRC Presss-Taylor and Francis Group.

Scully, J.C. 1975. Stress corrosion crack propagation: A constant charge criterion. *Corrosion Science*. **15**(4), pp.207-224.

Seddon, E. 1984. *The chemistry of ruthenium*. Netherlands: Elsevier.

Sedriks, J.A. 1979. *Corrosion of stainless steel*. John Wiley and Sons.

Shimomura, Y. and Nagumo, M. 2008. Ductile crack initiation and growth promoted by hydrogen in steel. *Environment-Induced Cracking of Materials*., pp.285-294.

Shing, T.L., Luyckx, S., Northrop, I.T. and Wolff, I. 2001. The effect of ruthenium additions on the hardness, toughness and grain size of WC-Co. *International Journal of Refractory Metals and Hard Materials*. **19**(1), pp.41-44.

Speidel, M.O. 1981. Stress corrosion cracking of stainless steels in NaCl solutions. *Metallurgical Transactions A*. **12**(5), pp.779-789.

Spencer, D.T., Edwards, M.R., Wenman, M.R., Tsitsios, C., Scatigno, G.G. and Chard-Tuckey, P.R. 2014. The initiation and propagation of chloride-induced transgranular stress-corrosion cracking (TGSCC) of 304L austenitic stainless steel under atmospheric conditions. *Corrosion Science*. **88**, pp.76-88.

Steen, W. 2003. *Laser Material Processing* .Third, ed.). Springer.

Sun, G.F., Zhang, Y.K., Zhang, M.K., Zhou, R., Wang, K., Liu, C.S. and Luo, K.Y. 2014. Microstructure and corrosion characteristics of 304 stainless steel laser-alloyed with Cr-CrB2. *Applied Surface Science*. **295**,pp.94–107.

Tabolt, D. and Tabolt, J. 1998. *Corrosion Science and Technology.* Second ed. New York, USA: CRC Press.

Terachi, T., Yamada, T., Miyamoto, T. and Arioka, K. 2012. SCC growth behaviors of austenitic stainless steels in simulated PWR primary water. *Journal of Nuclear Materials*. **426**(1–3), pp.59-70.

Thawari, G., Sundarararjan, G. and Joshi, S. V 2003. Laser surface alloying of medium

carbon steel with SiC. **423**, pp.41-53.

Tian, Y., Chen, C., Wang, D. and Lei, T. 2005. Surface modification of pure Ti by laser alloying with B and Ni mixed powders. *Advanced Engineering Materials*. **7**(7), pp.629-632.

Tjong, S.C., Lin, W.B., Ku, J.S. and Ho, N. 1996. Fe–Cr–Ni–Mo–Ru alloys produced by laser surface alloying. *Surface Engineering*. **12**(3), pp.246-250.

Torchio, S. and Venezian, V.G. 1980. Stress corrosion cracking of type AISI 304 stainless steel at room temperature; influence of chloride content and acidity. **20**(4), pp 555-561.

Toribio, J. and Kharin, V. 1997. The Effect Of History On Hydrogen Assisted Cracking: 1. Coupling Of Hydrogenation And Crack Growth. *International Journal of Fracture*. **88**(3), pp.233–245.

Truhan, J.J. and Hehemann, R.F. 1977. Surface aspects of pitting and stress corrosion cracking. NASA CR-135212 Report, Case Western Reserve University, Cleaveland, Ohio.

Truman, J.E. 1981. Stress-corrosion cracking of martensitic and ferritic stainless steels. *International Metals Reviews*. **26**(1),pp.301–349.

Truman, J.E. 1977. The influence of chloride content, pH and temperature of test solution on the occurrence of stress corrosion cracking with austenitic stainless steel. *Corrosion Science*. **17**(9), pp.737-746.

Tsai, W.T. and Chou, S.L. 2000. Environmentally assisted cracking behavior of duplex stainless steel in concentrated sodium chloride solution. *Corrosion Science*. **42**(10), pp.1741-1762.

Turnbull, A. and Zhou, S. 2008. Impact of temperature excursion on stress corrosion cracking of stainless steels in chloride solution. *Corrosion Science*. **50**(4), pp.913-917.

Tverberg, J.. 2003. Stainless Steel Selection Guide, Flow control magazine. *A stainless Steel Primer*. [Online]. [Accessed 13 May 2015]. Available from: http://www.metline-

pipefittings.in/wp-content/uploads/download/Stainless Steel-Nickel Alloys Selection Guide.pdf.

Ubah, C. and Asselin, E. 2009. High pressure and temperature electrochemical cell design for corrosion research. *ECS Transactions*. **19**(29), pp.3-20.

Vinoy, T.V., Shaikh, H., Khatak, H.S., Sivaibharasi, N. and Gnanamoorthy, J.B. 1996. Stress corrosion crack growth studies on AISI type 316 stainless steel in boiling acidified sodium chloride solution. *Journal of Nuclear Materials*. **238**(2–3), pp.278-284.

Wang, L.W., Du, C.W., Liu, Z.Y., Wang, X.H. and Li, X.G. 2013. Influence of carbon on stress corrosion cracking of high strength pipeline steel. *Corrosion Science*. **76**, pp.486-493.

Was, G.S. and Andresen, P.L. 2007. Stress Corrosion Cracking Behavior of Alloys in Aggressive Nuclear Reactor Core Environments. *Corrosion*. **63**(1), pp.19-45.

Westwood, A.R.. 1970. Adsorption sensitive fracture processes. N. Arup, R. . Parkins, and Nato, eds. *Advanced Study Institutes Series E-Applied Science 30*.

Wildgoose, G.G., Giovanelli, D., Lawrence, N.S. and Compton, R.G. 2004. High-temperature electrochemistry: A review. *Electroanalysis*. **16**(6), pp.421-433.

Williamson, R.L., Zanner, F.J. and Hareland, W.. 1988. Monochromatic imaging studies of low arc burning on molten Inconel 718 alloy electrodes during vacuum arc remelting. *Proceedings of the 9th International Conference of Special Melting, American Vacuum Society*.

Woodtli, J. and Kieselbach, R. 2000. Damage due to hydrogen embrittlement and stress corrosion cracking. *Engineering Failure Analysis*. **7**(6), pp.427-450.

Xie, Y. and Zhang, J. 2015. Chloride-induced stress corrosion cracking of used nuclear fuel welded stainless steel canisters: A review. *Journal of Nuclear Materials*. **466**, pp.85-93.

Yang, W. 2003. *Laser cladding surface treatment for enhancement of mechanical*

properties. PhD thesis. Peninsula Technikon.

Yao, J., Wang, L., Zhang, Q., Kong, F., Lou, C. and Chen, Z. 2008. Surface laser alloying of 17-4PH stainless steel steam turbine blades. *Optics and Laser Technology*. **40**(6), pp.838-843.

Yeh, T.K., Huang, G.R., Wang, M.Y. and Tsai, C.H. 2013. Stress corrosion cracking in dissimilar metal welds with 304L stainless steel and Alloy 82 in high temperature water. *Progress in Nuclear Energy*. **63**, pp.7-11.

Young, M.C., Huang, J.Y. and Kuo, R.C. 2009. Corrosion fatigue behavior of cold-worked 304L stainless steel in a simulated BWR coolant environment. *Materials Transactions*. **50**(3),pp.657–663.

Zanner, F.J., Williamson, R.L., Harrison, R.P., Flanders, H.D., Thompson, R.D. and Szeto, W.C. 1989. Vacuum Arc Remelting of Alloy 718. *Superalloy 718 Metallugy and Applications,* pp. 13-17.

Zhang, L. and Wang, J. 2014. Effect of dissolved oxygen content on stress corrosion cracking of a cold worked 316L stainless steel in simulated pressurized water reactor primary water environment. *Journal of Nuclear Materials*. **446**(1–3), pp.15-26.

Zhang, M., Sun, G. and S, Y.Z.C. 2014. Laser surface alloying of Cr-CrB2 onto a SUS 304 stainless steel substrate.**27**, pp.231-246.

Zhong, Y., Zhou, C., Songying, C. and Wang, R. 2017. Effects of temperature and pressure on stress corrosion cracking behavior of 310S stainless steel in chloride solution. *Chinese Journal of Mechanical Engineering*. **30**(1), pp.200-206.

Zhu, L.K., Yan, Y., Qiao, L.J. and Volinsky, A.A., 2013. Stainless steel pitting and early-stage stress corrosion cracking under ultra-low elastic load. *Corrosion Science*.**77**, pp.360-368.

Stress corrosion cracking of laser alloyed 304L stainless steel with Ru in hot chloride solution

N.N. Tshilwane[a, b, *], J.W. van der Merwe[a, b]

[a] *School of Chemical and Metallurgical Engineering, Faculty of Engineering and Built Environment, University of the Witwatersrand, Johannesburg, South Africa*
[b] *DST-NRF Centre of Excellence in Strong Materials, University of the Witwatersrand, Johannesburg, South Africa*

ARTICLE INFO

ABSTRACT

The exceptional ductility and good uniform corrosion resistance of austenitic stainless steels especially the commonly used 304L stainless steel is lost with its severe embrittling in aqueous conditions in the presence of chlorides at elevated temperatures. With the addition of ruthenium (Ru) the corrosion resistance of 304L stainless steel is enhanced, as well as the resistance to stress corrosion cracking. However, the cost of Ru is high and this limits the possibilities. Therefore, to lower the cost of Ru, a layer of approximately $950 \pm 90\,\mu m$ was laser cladded on the surface of 304L stainless steel. The purpose of this investigation is to evaluate the effectiveness of Ru additions to surface layer through laser cladding to mitigate cracking. Ru was applied to the surface of 304L stainless steel with a Nd:YAG laser as a metal powder with Ru concentrations of 1, 2, 5 and 10 wt%. With these methods, the cost of Ru is kept low while it can still cause inhibition of cracking. Three-point bend stressed samples were exposed to distilled water with 100 ppm sodium chloride at 200 °C with an initial dissolved oxygen concentration of 8 ppm at 25 °C. As expected the as-received 304L stainless steel was susceptible to stress corrosion cracking. With the addition of Ru to 304L stainless steel, the resistance to cracking improved markedly, the minimum and maximum crack propagation rate attained was 0.013 and 0.023 μm/s respectively. The crack propagation rate decreased as the Ru content was increased, and cracking was inhibited at 5 and 10 wt% Ru.

1. Introduction

In many industries, austenitic stainless steels are widely used because of excellent corrosion resistance and acceptable mechanical properties suitable for vessels and pipelines at relatively low cost. These steels receive their resistance to chemical attack by forming a passive film on the surface which prevents corrosion. Despite the passive film, austenitic stainless steel can fail due to the stress corrosion cracking (SCC) when exposed to extreme corrosive environment under tensile stress at elevated temperatures. This phenomenon is well described in literature [1–4] and is a concern in power plants and chemical industries. SCC occurs in different environments for different alloys, type 304L stainless steel will experience SCC in chloride containing solutions especially above a certain temperature threshold. When exposed to high temperature water with the presence of chlorides, 304L austenitic stainless steel has shown definite susceptibility to transgranular SCC [5,6]. The presence of dissolved oxygen and chloride ions concentration are the major factors promoting SCC at elevated temperatures.

The problems associated with SCC have been reported [7–9] and alloy developments to mitigate cracking is on-going research. For example, Andresen and Morra [1] showed that nickel base alloys were less susceptible to SCC in

high temperature water. Kumar et al. [10] reported the improved corrosion resistance of stainless steel laser alloyed with Mo powders. Moreover, Liang et al. [11] and Govender et al. [12] reported improvements in stress corrosion resistance of 304L stainless steel alloyed with Ru. Besides these promising improvements in corrosion resistance, Ru has the advantage of being the least expensive of the platinum group metals. It is often used in electronics industry, and the use of this element as an alloying element has been the attraction of a number of corrosion scientists over many years [11,13–15]. Apart from bulk alloying, laser surface alloying (LSA) is often used to improve mechanical properties such as wear and hardness. LSA is preferred over other techniques because of different microstructure introduced during self-quenching and solidification as the surface is melted [16]. Although this technique can improve the surface properties of the material, it is also important that the LSA parameters are carefully selected in order to reduce surface roughness which act as stress raisers or irregularities leading to the initiation of SCC cracks.

Despite a vast amount of work performed on SCC, there was no work conducted on LSA of 304L stainless steel with Ru. This study serves to evaluate the effect of Ru additions to thin surface layer through LSA to mitigate SCC. The present paper describes the initiation and propagation of SCC cracks after the samples were exposed to aqueous sodium chloride containing dissolved oxygen.

* Corresponding author at: School of Chemical and Metallurgical Engineering, Faculty of Engineering and Built Environment, University of the Witwatersrand, Johannesburg, South Africa.
Email addresses: nick.tshilwane@gmail.com (N.N. Tshilwane); josias.vandermerwe@wits.ac.za (J.W. van der Merwe).

2. Experimental procedure

2.1. Materials and sample preparation

Two types of samples were investigated: as received 304L stainless steel, as well as Ru laser surface alloyed samples. Rectangular coupons of approximately 80x40x5 mm were cut from 304L stainless steel plate and the surface was laser alloyed with 304 stainless steel powder containing 2wt% Ni and varying Ru at 0, 1, 2, 5 and 10wt%. The surface was cleaned and rinsed with acetone prior to cladding. A 4.4kW Rofin Sinar diode-pumped Nd: YAG laser mounted on KIKA articulated robot arm was used to melt the Ru powders as they were deposited on the surface. The optimum laser power and scan speed were set to 1.75kW and 1.75m/min respectively. Consecutive runs were performed with slight overlay to ensure complete coverage of the sample surface. The overlapping was achieved at 60% based on the equation reported by Makuch et al. [17]. Overlapping was kept below the critical value (70%) to minimise porosity defects and surface roughness [18,19]. Thereafter, the chemical composition of the samples was determined by using oxford Energy Dispersive X-Ray Spectroscopy (EDS) detector on a Zeiss Sigma field emission scanning electron microscopy (SEM). Three areas were selected on the surface of the alloyed layer and the values were averaged and tabulated as shown in Table 1.

There was no Ru additions on samples with 0wt% Ru, the surface layer was made from powders of 304 stainless steel and 2wt% Ni. The samples with Ru showed homogeneous distribution of Ru through the alloyed layer, but it was not as consistent as expected, the Ru was lower than expected for all samples except for samples with 2wt% Ru where the Ru content was 2.6wt%. Although EDS accuracy was not enough to determine Ru content of the alloyed layer, it was assumed here that the tabulated results (Table 1) gave a good indication of the Ru level.

2.2. Microstructure and hardness

The microstructural analysis was performed for laser alloyed samples and as-received 304L stainless steel. The samples were sectioned (15×5×5mm) and hot mount with Polyfast resin. The cross-sectional surface was ground to 1000 grit silicon carbide paper finish and polished. Two etchants, Marble's reagent and 10% oxalic acid were used to reveal the microstructure of the laser alloyed samples. Thereafter, SEM was used to examine the microstructure. The Vickers microhardness was performed on the cross-section of ground and polished LSA samples using Future Tech FM-700 microhardness tester. The applied force and dwell time was 500 gf and 10s respectively. The hardness measurements were recorded at 100μm interval cores indentation.

2.3. SCC test

A constant deformation, three-point bend test was used to evaluate SCC resistance of the LSA and as-received 304L stainless steel samples. The samples were designed for testing at stress levels below the elastic limit of the as-received 304L stainless steel.

2.3.1. Tensile stress

SCC test samples were cut from the LSA coupon by using an abrasive cutter to a size of 40×5×5mm. The laser cladded surface was ground to 800 grit finish with silicon carbide paper and rinsed with ethanol. Kyowa strain gages were mounted on the ground LSA surface and were left in air to dry and cure at room temperature for 24h. Thereafter, the samples were stressed to 350MPa on a three-point bent rig as shown in Fig. 1. Labview Signal Express integrated with NI data acquisition device and strain gauges were used to measure the applied tensile stresses after a stress calibration was performed using dead weights. It is important to note that tensile properties of the material were determined with a 50kN Thinus Olsen tensile tester especially with the aim to determine the yield point for stress calibration of the stress corrosion test.

The rig, bolt and nut were fabricated from the same material (304L stainless steel) as the sample in order to reduce the galvanic corrosion. The stressed samples on the rig were placed in an autoclave and care (insulate inner wall of the autoclave with Teflon) was taken, both with the rig itself and autoclave, to avoid galvanic action between dissimilar materials.

2.3.2. Test environment

Distilled water with 100ppm sodium chloride was used as the test solution after it was purged with oxygen to achieve an approximate 8ppm dissolved oxygen (DO) concentration at room temperature. The DO concentration was measured using a T-Heng M1500K portable dissolved oxygen meter. The stressed samples on a three-point bent rig were exposed to this solution in an autoclave for 172h at 200°C, but the DO was controlled at room temperature to ensure a standard solution for comparison. The test solution was replaced for every new test run.

2.4. Post exposure analysis

The samples were removed from the autoclave and examined for pitting and SCC cracks under a Nikon stereo microscope. Thereafter, the samples were metallographically prepared to evaluate the SCC crack morphology. The length of the cracks was measured on SEM and it was assumed that crack initiation started from the initial exposure, although not completely accurate but an assumption to make. In SEM, backscattered electron detector (BSD) was used for imaging.

The repeatability of samples was performed to validate the results. The repeatability was conducted on six samples (laser cladded samples with 0, 1, 2, 5, 10wt% and as-received 304L stainless steel). The deviation of results was minimal as shown in the Results section (Fig. 8).

3. Results

3.1. Microstructural analysis

A comparison of the alloyed layer and as-received 304L stainless steel showed a difference in the microstructure. The grains were more refined on the alloyed layer that the base material (Fig. 2).

The laser alloyed coupons consisted of three main zones, namely the alloyed layer (AL), transition zone (TZ) and base metal (BM) as shown in Fig. 3. Fine microstructure was observed on the alloyed layer. This could be attributed to high thermal stresses and rapid cooling introduced during LSA process.

Table 1
Chemical composition (wt%) of tested alloys as determined by EDS.

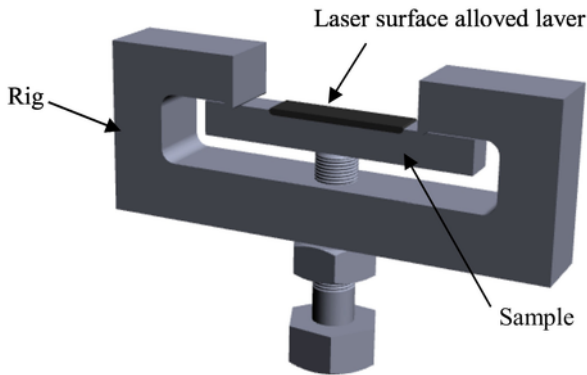| Alloy	Mn	Si	Cr	Ni	Ru	Fe
As-received 304L	2.0±0.1	0.75±0.1	19±0.2	8±0.2	–	Balance
304L + 0% Ru	1.5±0.3	0.5±0.2	18.9±0.2	8.2±0.1	–	Balance
304L + 1% Ru	1.5±0.2	0.7±0.1	18.7±0.1	10.7±0.2	**0.5**	Balance
304L + 2% Ru	1.3±0.2	0.7±0.3	17.9±0.2	13.8±0.1	2.6±0.3	Balance
304L + 5% Ru	–	0.4±0.3	21.9±0.1	12.9±0.2	3.8±0.2	Balance
304L + 10% Ru	–	0.4±0.2	21.4±0.1	11.8±0.2	7.9±0.2	Balance

Fig. 1. Ru laser surface alloyed 304L stainless steel sample and stressed to 350 MPa on a three-point bend test rig.

Small islands of refined microstructure were observed towards the top surface of the alloyed layer as depicted in Fig. 3. These islands were randomly formed on the surface and were observed on samples with lower Ru content (0, 1 and 2 wt%) whereas at high Ru content (5 and 10 wt%) they were not present. The measured thickness of the alloyed layer was approximately $950 \pm 90\,\mu m$ for all samples. The microstructure of the alloyed layer was in accordance to that described by Liang et al. [11], the grain structure consists of elongated cellular dendrites. Brytan et al. [20] observed a similar microstructure for laser alloyed austenitic stainless steels.

3.2. Hardness measurements

The averaged Vickers hardness value of the alloyed layer on the cross-section increased significantly. The minimum hardness value was obtained at 160 HV for the samples with 0 wt% Ru and the maximum at 248 HV for sample with 10 wt% Ru (Fig. 4). The hardness value of as-received 304L stainless steel was 152 HV.

Laser surface alloying coupons increased the hardness by 40%. The measured hardness at the transition zone was lower than that of the alloyed layer.

The higher value of hardness of the alloyed can be attributed to the refined microstructure [21].

3.3. SCC of laser alloyed samples

After exposing samples to a corrosive environment as outlined in Section 2.3.2, they were then evaluated for crack initiation and propagation. The cracks initiated from the top surface and propagated down to the mid-section of the sample in a transgranular manner (Fig. 5). Most of SCC cracks on the alloyed layer propagated transgranularly at an acute angle to the tensile stresses as shown in Fig. 5(b). Based on finite element analysis of the sample on a three-point bend rig, tensile stresses were found at the top and compressive stresses at the bottom, and at the neutral axis there were minimal or no stresses. Hence, it was not surprising to have no cracks at the centre and towards the bottom for some of the samples.

There was no unique pattern at which the cracks propagated. The observations undertaken revealed coalescence of cracks on the alloyed layer. Fig. 6 illustrates how the SCC cracks randomly initiated from the alloyed surface and coalesced towards the transition zone. It was also evident that Ru played a role as an alloying element, the number of cracks reduced with increasing Ru content. This can be witnessed by fine and shallow cracks formed on the alloyed layer when compared to as-received 304L stainless steel.

The refined microstructure reduced the presence of corrosion pits which promotes SCC crack nucleation. The samples with higher Ru content were immune to SCC as shown in Fig. 7. There were few islands of undissolved Ru observed on the alloyed layer of these samples.

The length of the crack plays a significant role in qualifying the susceptibility of alloys for SCC. Elsariti and Haftirman [22] reported the dependence of crack length on chloride concentration as it increased significantly with increased chloride concentration for austenitic alloys. Another study by Spencer et al. [6] related the crack growth rate with the strain leading to SCC. In the present study the crack growth rate was determined in relation to the Ru content on the alloyed layer. As expected, the maximum crack propagation rate decreased as the Ru content was increased as shown in Fig. 8.

The crack propagation rate of the laser surface alloyed samples was lower than the as-received 304L stainless steel. The samples with higher Ru content

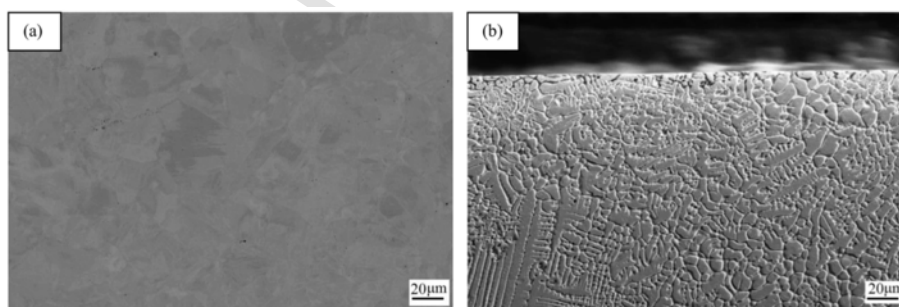**Fig. 2.** SEM micrographs of tested samples (a) microstructure of as-received 304L stainless steel electrolytic etched with 10% oxalic acid at 6 V for 60s (b) microstructure of laser alloyed 304L stainless steel with 1% Ru and etched with marble reagent and 10% oxalic acid.
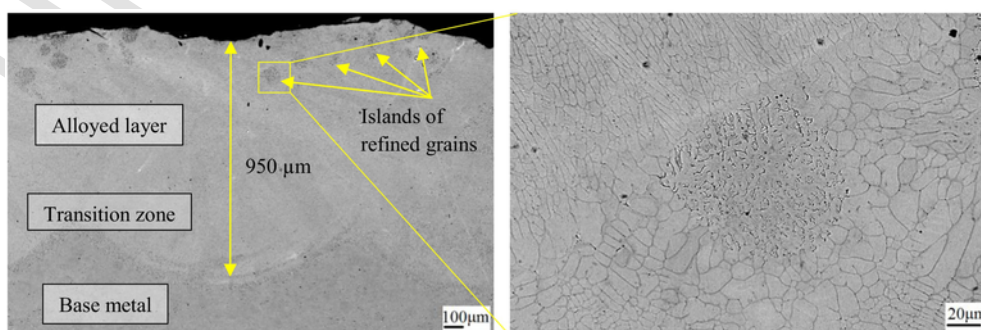

Fig. 3. Microstructure of laser alloyed 304L stainless steel with 1% Ru and etched with Marble reagent and 10% oxalic acid.
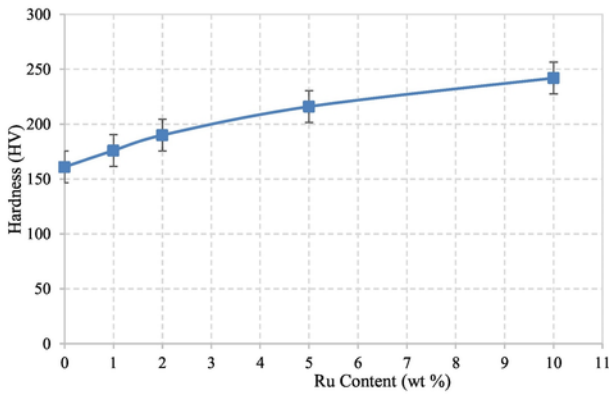
Fig. 4. Microhardness of laser alloyed zone of stainless steel at different Ru content.

(5 and 10 wt%) were immune to SCC. As indicated in Fig. 8, the samples which were immune to SCC had a propagation rate of zero. It should be noted here that the zero propagation rate means the samples were not susceptible to SCC.

4. Discussion

There are many parameters which can be altered to improve SCC resistance of alloys in corrosive environments. The present paper focused on evaluating the SCC susceptibility of LSA samples alloyed with Ru.

4.1. Influence of microstructure on SCC

The thermal gradients introduced during LSA process contributed to the refined microstructure which in turn proved to have an influence on the resistance of SCC. There were fewer cracks on the alloyed layer than on as-received 304L stainless steel. This can be attributed to the refined microstructure of the alloyed layer where the fewer corrosion pits were found. As shown in Fig. 9, the crack propagated and widen at the grain boundary and forming a pit. The phenomena of pits acting as stress raisers is well explained by Esih et al.
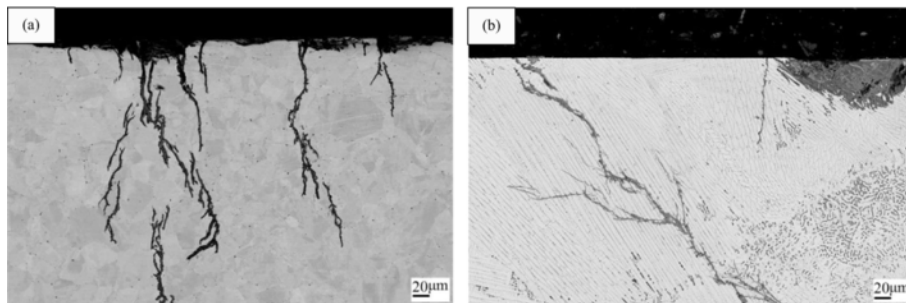
Fig. 5. Transgranular SCC of alloys exposed to 100 ppm NaCl and 8 ppm DO at 200 °C for 172 h (a) As-received 304L stainless steel (b) Laser alloyed 304L stainless steel with 0 wt% Ru.
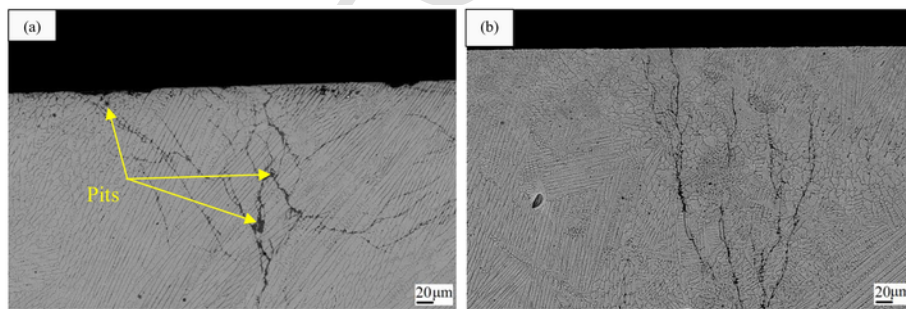
Fig. 6. The cross-section of laser alloyed 304L stainless steel showing transgranular SCC after exposure in 100 ppm NaCl and 8 ppm DO at 200 °C for 172 h (a) 1 wt% Ru (b) 2 wt% Ru.
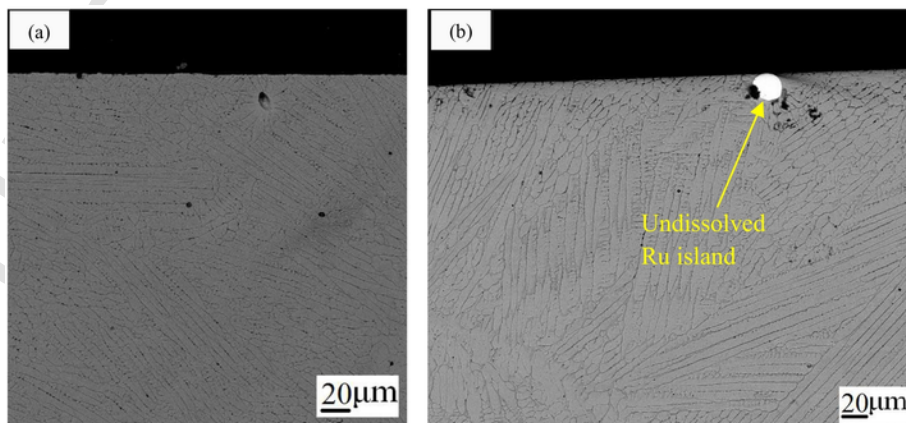
Fig. 7. SEM micrograph of laser alloyed samples after exposure in 100 ppm sodium chloride with 8 ppm DO at 200 °C for 172 h (a) 5 wt% Ru (b) 10 wt%.

Fig. 8. Maximum crack propagation rate of alloys after exposed in 100 ppm sodium chloride and 8 ppm DO at 200 °C for 172 h.

Fig. 9. Transgranular SCC of 304L stainless steel laser alloyed layer with 1% Ru after exposure in 100 ppm NaCl and 8 ppm DO at 200 °C for 172 h.

[23], where thermal oxides were found to facilitate corrosion pits but did not influence their nucleation. Here the pits could have been initiated from the chloride ions, and some of pits did not contribute to the initiation of the SCC crack.

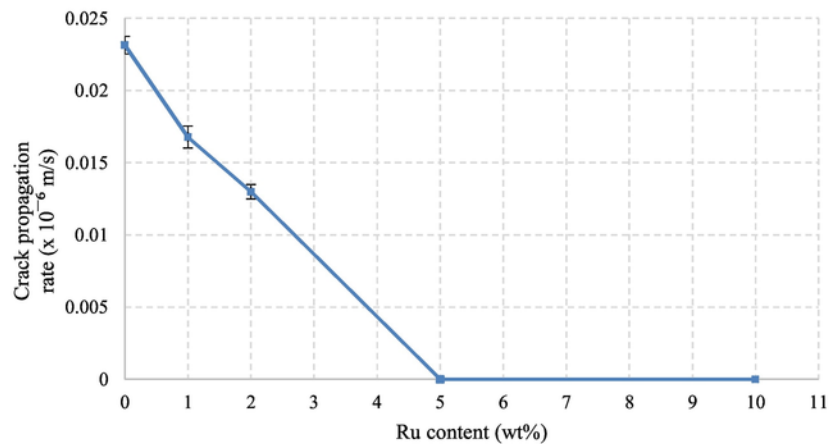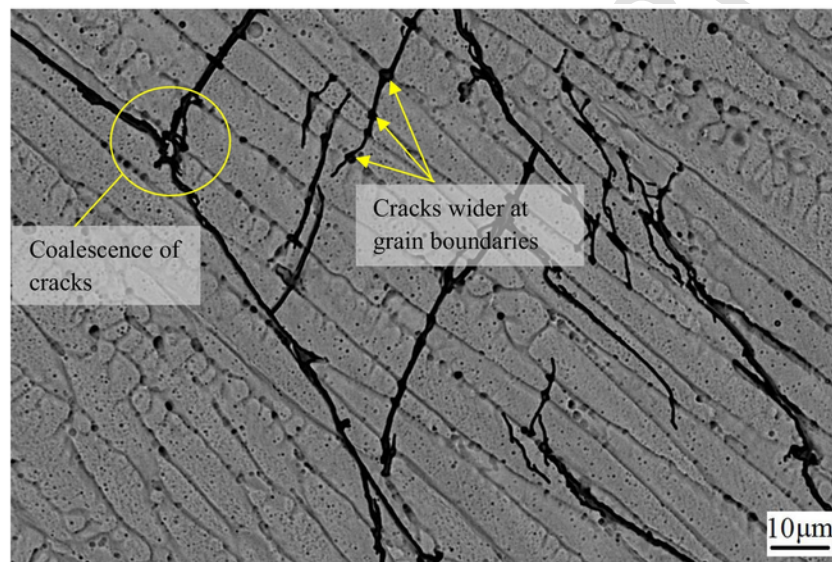The density of SCC cracks was higher on the elongated grains structure than on the refined structure of the alloyed layer. At the heat affected zone, few SCC cracks were arrested while others propagated into the base material. The samples with higher Ru content (5 and 10 wt%) had more refined microstructure and they were immune to SCC.

4.2. Effect of Ru on SCC

Alloying metals with Ru has shown excellent corrosion resistance in various media [12,14,15,24]. Here a laser surface alloyed 304L stainless steel with Ru improved the resistance to SCC. The effect of Ru additions on the alloyed layer was observed for all alloys and the SCC susceptibility was evaluated. It was found that the density of cracks reduced as the Ru content increased. The cracks became finer and were shallow when compared to the as-received 304L stainless steel. The propagation of cracks through the alloyed clad did not follow the same pattern as that of the as-received 304L stainless steel. The cracks stopped and started irregularly on the alloyed layer. This could be attributed to the presence of Ru and the dissolution at the crack tip. The propagation rate reduced as the Ru content was increased. The lowest propagation rate was deter-

mined as 0.013 μm/s (2 wt% Ru) and it was approximately one third of the as-received 304L stainless steel (0.039 μm/s). This was in accordance with the work reported by Scenini et al., the samples with 1 wt% Ru were less susceptible to SCC as compared to as-received 304 stainless steel.

Different mechanisms for SCC have been reported in literature [25–27]. However, here it was found that the SCC was based on the film rupture mechanism explained by Jones (1992) [28]. The chloride species will migrate to the surface of the alloy where absorption and diffusion takes place on the surface. The chemical reaction with the presence of the tensile stresses will break the oxide film and allowing the solution to penetrate into the surface and leading to crack propagation.

5. Conclusions

The present study showed a significant improvement in SCC resistance of Ru laser surface alloyed 304L stainless steel in aqueous sodium chloride containing DO. The conclusions drawn from the findings were:

■ Corrosion pits acted as crack initiation sites and the cracks propagated transgranularly for samples with lower Ru content (0, 1 and 2 wt%) while those with higher Ru content (5 and 10 wt%) were immune to SCC. The crack propagation rate decreased significantly as the Ru content was increased.

- The refined microstructure of the alloyed layer played a major role in the crack propagation and arrest. The SCC cracks propagated diagonal to tensile stress direction.
- The microhardness of laser alloyed samples increased remarkably, the highest hardness value was 248 HV which was 40% more when compared to as-received 304L stainless steel.

Acknowledgement

References

[1] P.L. Andresen, M.M. Morra, Stress corrosion cracking of stainless steels and nickel alloys in high-temperature water, Corrosion 64 (2008) 15–29.

[2] L.K. Zhu, Y. Yan, L.J. Qiao, A.A. Volinsky, Stainless steel pitting and early-stage stress corrosion cracking under ultra-low elastic load, Corros. Sci. 77 (2013) 360–368.

[3] Y. Xie, J. Zhang, Chloride-induced stress corrosion cracking of used nuclear fuel welded stainless steel canisters: a review, J. Nucl. Mater. 466 (2015) 85–93.

[4] R. Nishimura, Characterization and perspective of stress corrosion cracking of austenitic stainless steels (type 304 and type 316) in acid solutions using constant load method, Corros. Sci. 49 (2007) 81–91.

[5] S. Ghosh, V. Kain, Microstructural changes in AISI 304L stainless steel due to surface machining: effect on its susceptibility to chloride stress corrosion cracking, J. Nucl. Mater. 403 (2010) 62–67.

[6] D.T. Spencer, M.R. Edwards, M.R. Wenman, C. Tsitsios, G.G. Scatigno, P.R. Chard-Tuckey, The initiation and propagation of chloride-induced transgranular stress-corrosion cracking (TGSCC) of 304L austenitic stainless steel under atmospheric conditions, Corros. Sci. 88 (2014) 76–88.

[7] M.C. Young, J.Y. Huang, R.C. Kuo, Corrosion fatigue behavior of cold-worked 304L stainless steel in a simulated BWR coolant environment, Mater. Trans. 50 (2009) 657–663.

[8] M. Clark, O. Yong, A.M. Brennenstuhl, M. Lau, Environment-induced transgranular stress corrosion cracking of 304L stainless steel instrument line tubes, In: Environment-induced Cracking of Materials, 2008, pp. 421–430.

[9] M.F. Hurley, C.R. Olson, L.J. Ward, B.J. Jaques, K.A. Johnson, J.K. Gunnerson, D.P. Butt, Transgranular stress corrosion cracking of 304L stainless steel pipe clamps in direct use geothermal water heating applications, Eng. Fail. Anal. 33 (2013) 336–346.

[10] D. Kumar, K. Sridhar, A.R. Biswas, G.L. Goswami, M.B. Deshmukh, Characterization of laser produced high molybdenum surface alloys on stainless steel substrates, J. Laser Appl. 5 (1993) 23–32.

[11] D. Liang, J.W. Sowards, G.S. Frankel, B.T. Alexandrov, J.C. Lippold, Corrosion resistance of welds in type 304L stainless steel made with a nickel–copper–ruthenium welding consumable, Corros. Sci. 52 (2010) 2439–2451.

[12] K. Govender, F. Scenini, S. Lyon, A. Sherry, Influence of Pd and Ru additions on stress corrosion cracking of austenitic stainless steels, Corros. Eng. Sci. Technol. 47 (2012) 507–515.

[13] J. Van Der Merwe, D. Tharandt, Corrosion resistance of laser-cladded 304L stainless steel enriched with ruthenium additions exposed to sulphuric acid and sodium chloride media, J. South. Afr. Inst. Min. Metall. 115 (2015) 499–505.

[14] J.H. Potgieter, J. Thomson, F.V. Adams, A.S. Afolabi, Effect of additions of Ru and Pd on the electrochemical behaviour of austenitic stainless steel in organic acids, Int. J. Electrochem. Sci. 9 (2014) 6451–6463.

[15] F. Scenini, K. Govender, S. Lyon, A. Sherry, Stress Corrosion Cracking of Ru Doped 304 Stainless Steel in High Temperature Water, 47, 2012.

[16] C.W. Draper, J.M. Poate, Laser surface alloying, Int. Mater. Rev. 30 (1985) 85–108.

[17] N. Makuch, M. Kulka, P. Dziarski, D. Przestacki, Laser surface alloying of commercially pure titanium with boron and carbon, Opt. Lasers Eng. 57 (2014) 64–81.

[18] Y. Li, J. Ma, Study on overlapping in the laser cladding process, Surf. Coat. Technol. 90 (1997) 1–5.

[19] C. Hu, T.N. Baker, Overlapping laser tracks to produce a continuous nitrided layer in Ti–6Al–4V alloy, J. Mater. Sci. 32 (1997) 2821–2826.

[20] Z. Brytan, M. Bonek, L.A. Dobrzański, Microstructure and properties of laser surface alloyed PM austenitic stainless steel, Journal of Achievements in Materials and Manufacturing Engineering 40 (2010) 70–78.

[21] S.C. Tjong, W.B. Lin, J.S. Ku, N. Ho, Fe–Cr–Ni–Mo–Ru alloys produced by laser surface alloying, Surf. Eng. 12 (1996) 246–250.

[22] S.M. Elsariti, Haftirman, Behaviour of stress corrosion cracking of austenitic stainless steels in sodium chloride solutions, Procedia Engineering 53 (2013) 650–654.

[23] I. Esih, V. Alar, I. Juraga, Influence of thermal oxides on pitting corrosion of stainless steel in chloride solutions, Corros. Eng. Sci. Technol. 40 (2005) 110–120.

[24] , Corros. Sci. ()

[25] H.L. Logan, Film-rupture mechanism of stress corrosion, J. Res. Natl. Bur. Stand. 48 (1952) 99.

[26] Y.J. Kim, Analysis of oxide film formed on type 304 stainless steel in 288 °C water containing oxygen, hydrogen, and hydrogen peroxide, Corrosion 55 (1999) 81–88.

[27] R.C. Newman, C. Healey, Stability, validity, and sensitivity to input parameters of the slip-dissolution model for stress-corrosion cracking, Corros. Sci. 49 (2007) 4040–4050.

[28] R.H. Jones, Stress Corrosion Cracking, Materials Performance and Evaluation, 1992.

Appendix B: Elemental composition

The elemental chemical composition was performed using both the XRF and EDS techniques. The analysed samples were as-received 304L SS, as-received 2205 duplex stainless steel, LSA and VAR samples. The data was recorded in Table B-1 to Table B-4. The chemical composition of as-received alloys (304L and 2205) was correlated to the supplier's specifications (Outokumbu, 2015).

Table B-1: Chemical composition of as-received 304L SS determined by using XRF.

ELEMENT	COMPOSITION IN MASS %
Carbon	0.021
Manganese	1.49
Sulphur	0.011
Phosphorus	0.033
Silicon	0.93
Chromium	18.4
Molybdenum	0.11
Nickel	8.02
Copper	0.09
Aluminium	0.29
Vanadium	0.07
Niobium	≤0.005
Titanium	≤0.005
Cobalt	0.023
Iron	Balance

Table B-2: Chemical composition of as-received 2205 duplex SS determined by using XRF.

ELEMENT	COMPOSITION IN MASS %
Carbon	0.046
Manganese	1.39
Sulphur	≤0.005
Phosphorus	0.084
Silicon	0.47
Chromium	22.5
Molybdenum	2.28
Nickel	5.54
Copper	0.19
Aluminium	≤0.005
Vanadium	≤0.005
Niobiuom	≤0.005
Titanium	≤0.005
Cobalt	0.04
Iron	Balance

Table B-3: Chemical composition of laser surface alloyed 304L SS with Ru determined by using XRF.

ELEMENT	COMPOSITION IN MASS %				
	304L + 0%Ru	304L + 1%Ru	304L + 2%Ru	304L + 5%Ru	304L + 10%Ru
Carbon	0	0.000	0.000	0.071	0.108
Manganese	1.64	1.475	1.450	1.444	1.386
Sulphur	0	0.000	0.000	0.005	0.005
Phosphorus	0.007	0.009	0.008	0.008	0.011
Silicon	1.24	0.832	0.745	0.751	0.891
Chromium	18.5	18.117	17.542	16.245	14.31
Molybdenum	0.08	0.079	0.078	0.086	0.090
Nickel	12.2	11.781	12.152	12.54	12.78
Copper	0.05	0.050	0.049	0.048	0.054
Aluminium	0.28	0.007	0.005	0.152	0.198
Vanadium	≤0.005	0.005	0.005	0.005	0.005
Niobium	≤0.005	0.005	0.005	0.005	0.005
Titanium	≤0.005	0.005	0.005	0.005	0.005
Cobalt	0.028	0.013	0.049	0.074	0.080
Ruthenium	0	0.980	1.960	4.740	9.210
Iron	65.96	66.63	65.94	63.81	61.07

Elemental composition of vacuum remelted samples

The elemental composition of vacuum arc remelted (VAR) samples was determined using SEM machine incorporated with EDS. Three regions were selected on the surface of the sample and analysed as shown in Figure B-1. The mass of each element was averaged and recorded in Table B-4.
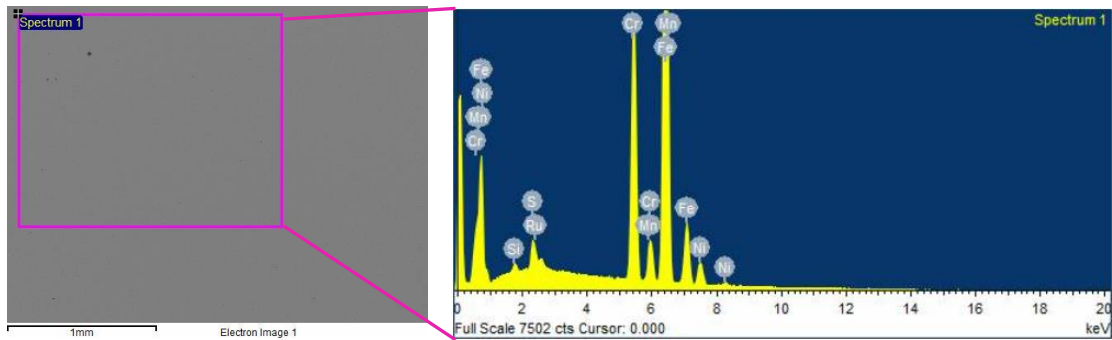

Figure B-1: EDS spectrum showing a region of analysis of VAR 304L SS with 1.07 wt% Ru.

Table B-4: EDS chemical composition of vacuum remelted 304L stainless steel with Ru.

ELEMENT	COMPOSITION IN MASS %				
	304L + 0% Ru	304L + 1% Ru	304L + 2% Ru	304L + 5% Ru	304L + 10% Ru
Manganese	1.59 ± 0.1	1.22 ± 0.2	1.81 ± 0.2	1.63 ± 0.1	1.41 ± 0.2
Silicon	0.45 ± 0.2	0.93 ± 0.3	0.84 ± 0.2	0.72 ± 0.2	0.80 ± 0.1
Chromium	19.47 ± 0.4	20.14 ± 0.1	18.78 ± 0.1	17.81 ± 0.2	16.81 ± 0.1
Nickel	10.76 ± 0.1	11.08 ± 0.1	10.72 ± 0.3	10.19 ± 0.1	10.22 ± 0.2
Iron	66.81 ± 0.3	65.64 ± 0.1	65.8 ± 0.2	63.61 ± 0.1	58.51 ± 0.3
Ruthenium	-	1.07 ± 0.2	2.05 ± 0.1	6.07 ± 0.2	12.34 ± 0.1

The Ru content was slightly higher than what was expected. Other elements remained almost constant as the Ru content was increased. There was no further Ni added on these samples.

Grain size analysis

The size of grains was determined according to ASTM E112-12 by using an optical microscope. Three regions were selected on the cross-section of the alloyed layer and the grain size number was measured using the intercept method. These grain size numbers were then averaged and tabulated in Table B-5.

Table B-5: Grain size analysis of laser alloyed 304L stainless steel with Ru.

Ru addition (wt%)	Grain size number			Mean grain Size number	Mean intercept Length (μm)
	Region 1	Region 2	Region 3		
0	10.9	10.2	9.4	10.2	8.2
0.98	11.2	10.2	10.7	10.6	7.3
1.96	10.6	11.2	10.7	10.8	7.1
4.74	10.9	10.7	11.4	11.0	6.6
9.2	9.5	8.7	9.3	9.2	12.1

The intercept method was also oused gto determine the grain size number as shown in Table B-6. The grain size increased and decreased for samples with higher Ru content (12.34 wt% Ru).

Table B-6: Grain size analysis of vacuum remelted 304L stainless steel with Ru.

Ru addition (wt%)	Grain size number			Mean grain Size number	Mean intercept Length (μm)
	Region 1	Region 2	Region 3		
0	5.6	5.7	5.21	5.5	49.2
1.07	5.8	5.7	5.5	5.7	44.7
2.05	5.9	5.8	5.9	5.9	43.3
6.07	5.8	5.9	6.3	6.0	41.9
12.34	2.8	2.4	4.1	3.3	94.2

Appendix C: Calibration of applied tensile stress

Kyona strain gauges were used to measure the strain of the samples when subjected to the loading. The strain measurement was then calibrated to determine the applied stress. It was important to mount the stain gauges on clean surface. The samples were ground to a final 1200 grit paper and the strain gauges were mounted as follows;

- Mark on the surface exactly the intended position to mount strain gauge; it should be noted that plastic gloves must be used at all times.
- Apply cement on the surface of the sample and gradually position the strain gauge to the sample where it will adhere to the surface of the sample.
- Apply light pressure by using a thumb on the mounted strain gauge for 60 seconds and leave the samples to dry in air for 12 hours as shown in Figure C-1.

The wire, paper and cement form a major part in defining the properties and sensitivity for strain gauge application therefore selecting the right one is important. The stability of strain gauges is improved by heat treatment during manufacturing. It was important that the sample surface was not touched with fingers or brought in contact with the skin at all times.
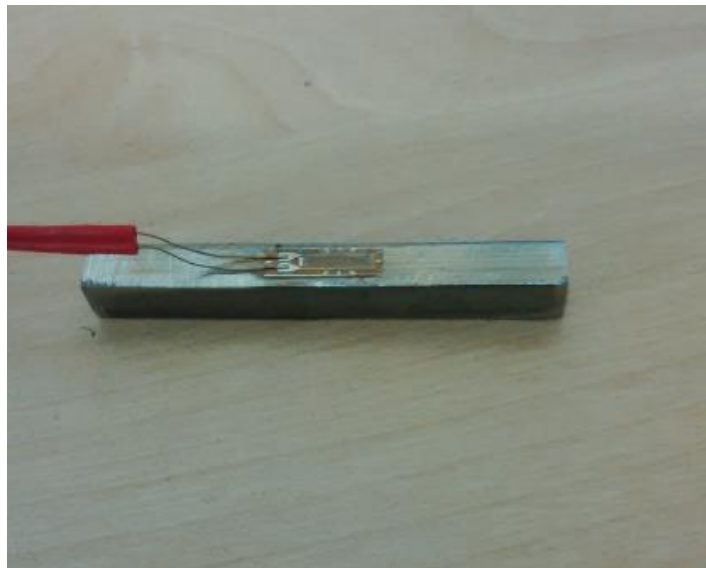

Figure C-1: Type 304L stainless steel sample mounted with a strain gauge.

The applied loading on the specimen was calibrated prior to stressing the sample on a three-point rig. The load was applied in steps using dead weights as shown in Figure C-2.
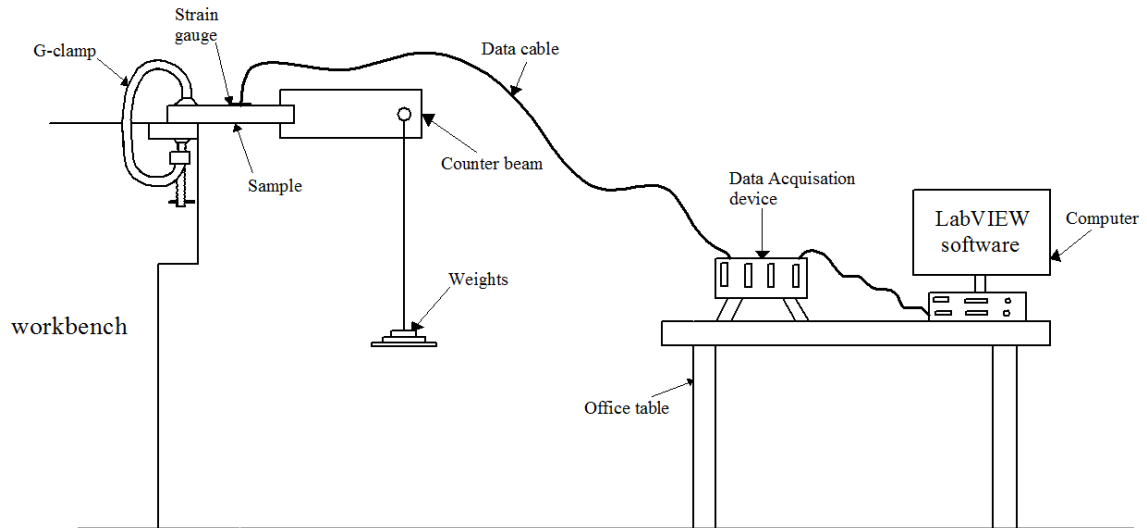
Figure C-2: Experimental set-up for calibrating the samples.

The data was recorded for the applied load and the corresponding strain displayed on LabVIEW software was recorded as shown in Table C-1. The loading and unloading of dead weights was repeated three times and the corresponding strain was recorded. The maximum bending stress corresponding to the applied dead load was also calculated and recorded. The LSA samples used in this study were calibrated the same way as-received 304L stainless steel

Table C-1: Calibration data of as-received 304L stainless steel.

Total Dead weight (kg)	Applied Dead weight (N)	Total Moment (Nm)	Averaged Strain	Applied Stress (MPa)
0	0	0	0.0058	0
2.5	25	6.21491	0.0071	249.0
3.6	36	9.425379	0.0086	377.7
4.6	46	12.13977	0.0098	486.4
5.1	51	13.63579	0.0142	546.4

The total bending stress was calculated by adding both moments. The bending moment 1 was calculated as;

$$M_1 = Fd_1$$
$$= m_1 g d_1$$
$$= \frac{2}{3} m_1 g D_1$$

Where m_1 and D_1 was the first load [kg] and moment arm [m] respectively, g gravitational constant in m/s^2. The second moment applied to the sample was due to the dead weighs and was obtained as;

$$M_2 = Fd_2$$
$$= m_2 g(l + D_1)$$

Where m_2 was the mass [kg] of dead weights (including the mass of a hook with a base plate) and d_2 was the second moment arm [m] measured. The total moment [Nm] was thereafter used to calculate the bending stress as follows;

$$M_{total} = M_1 + M_2$$

$$\sigma_b = \frac{M_{total} \times y}{I}$$

Where I is the moment of inertia [m^4] and y is the neutral axis [m]. Using the stress (calculated) versus strain (measured using strain gauge and NI LabVIEW software) graph, the strain was scaled to stress. To validate the results, dead weights was applied again to confirm if the calculated stresses corresponded to the calibrated values. The values were relatively the same with a marginal error of less than 1%. The above mentioned calculations were based on assumptions that the sample material was homogeneous and isotropic and the samples were free from expansion and contraction and Young's modulus was constant in compression and tension.

Appendix D: Engineering drawings

An autoclave used for electrochemical tests was designed as per the drawing shown in Figure D-1 to Figure D-5. It should be noted that the drawing are only for the purpose of the work conducted here and permission will be required for any further application.
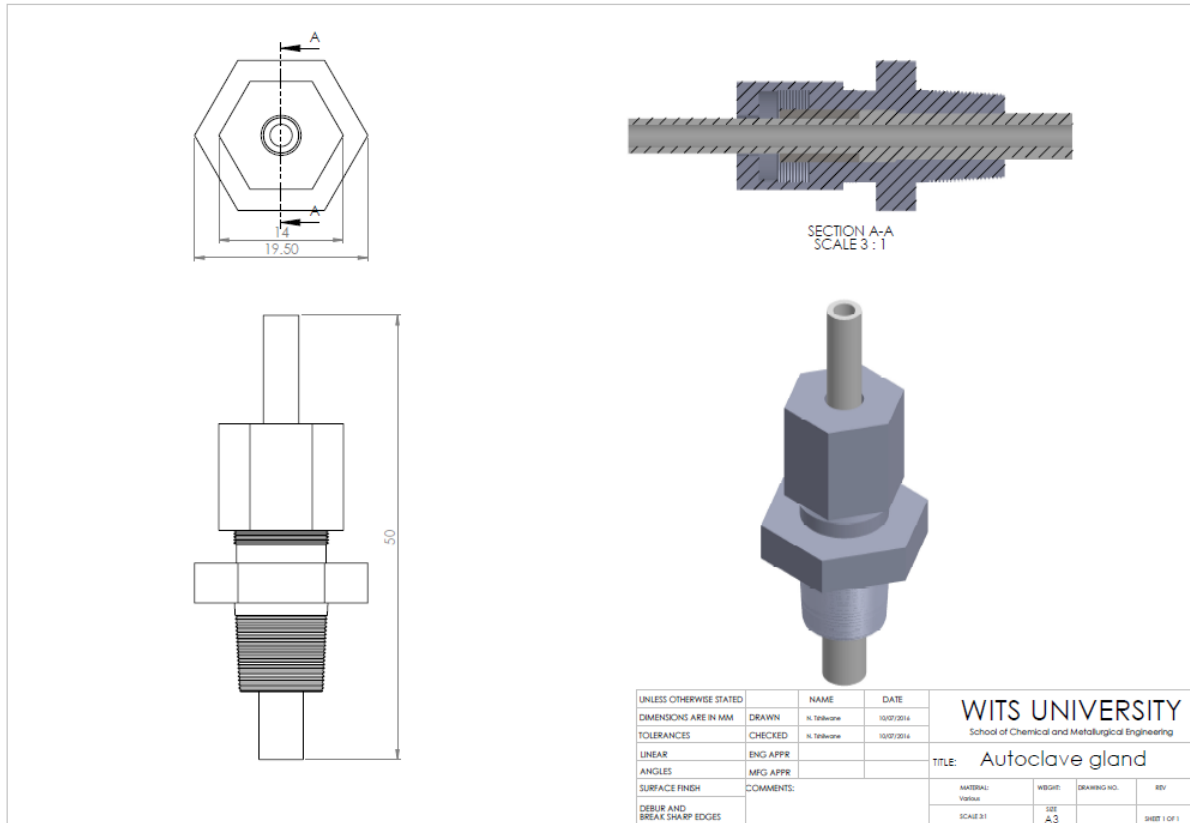

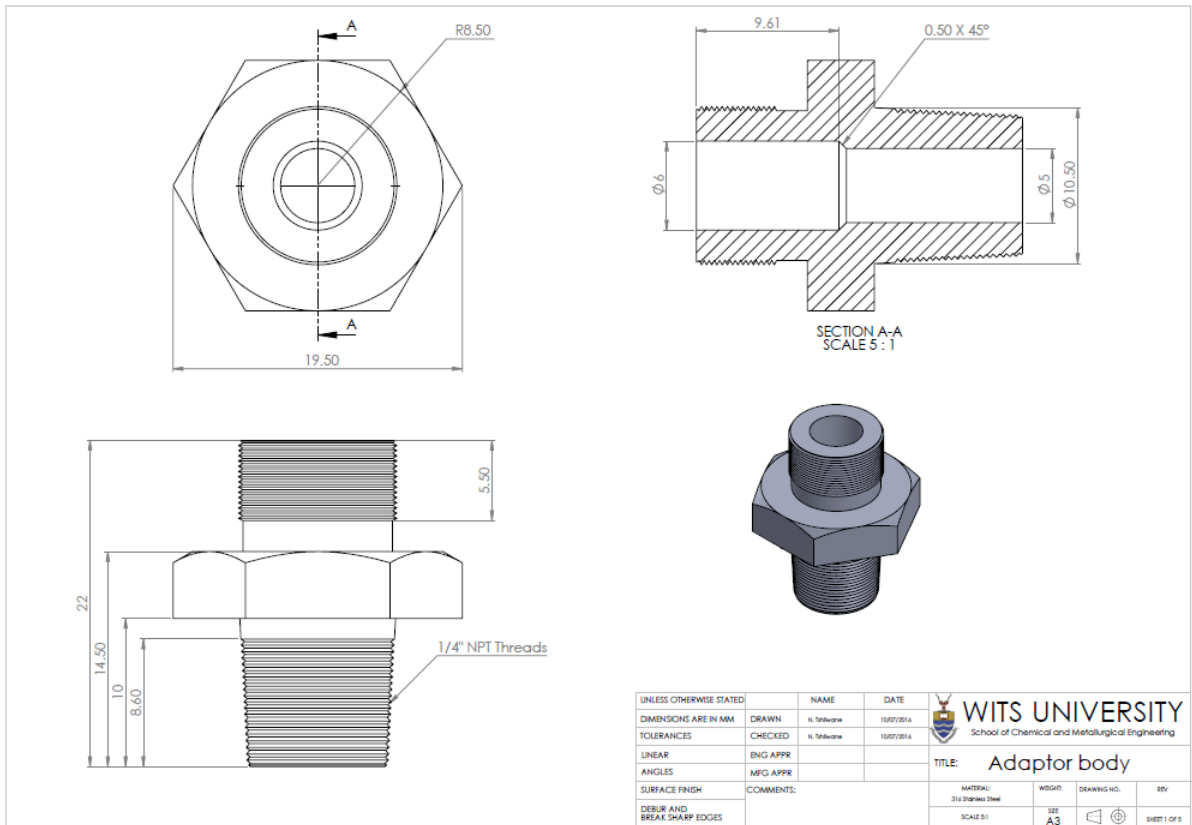Figure D-1: Autoclave gland fabricated from 316 stainless steel and Teflon.

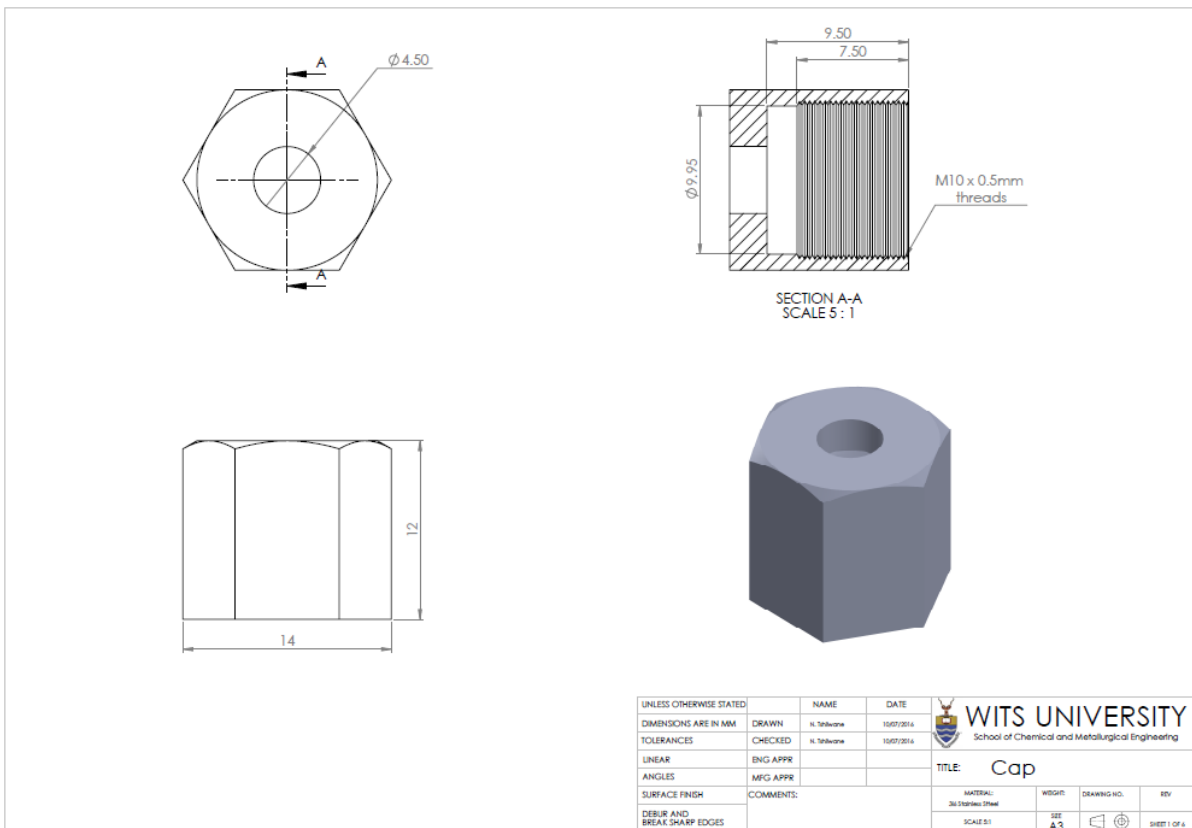Figure D-2: 316 stainless steel adaptor fitting.

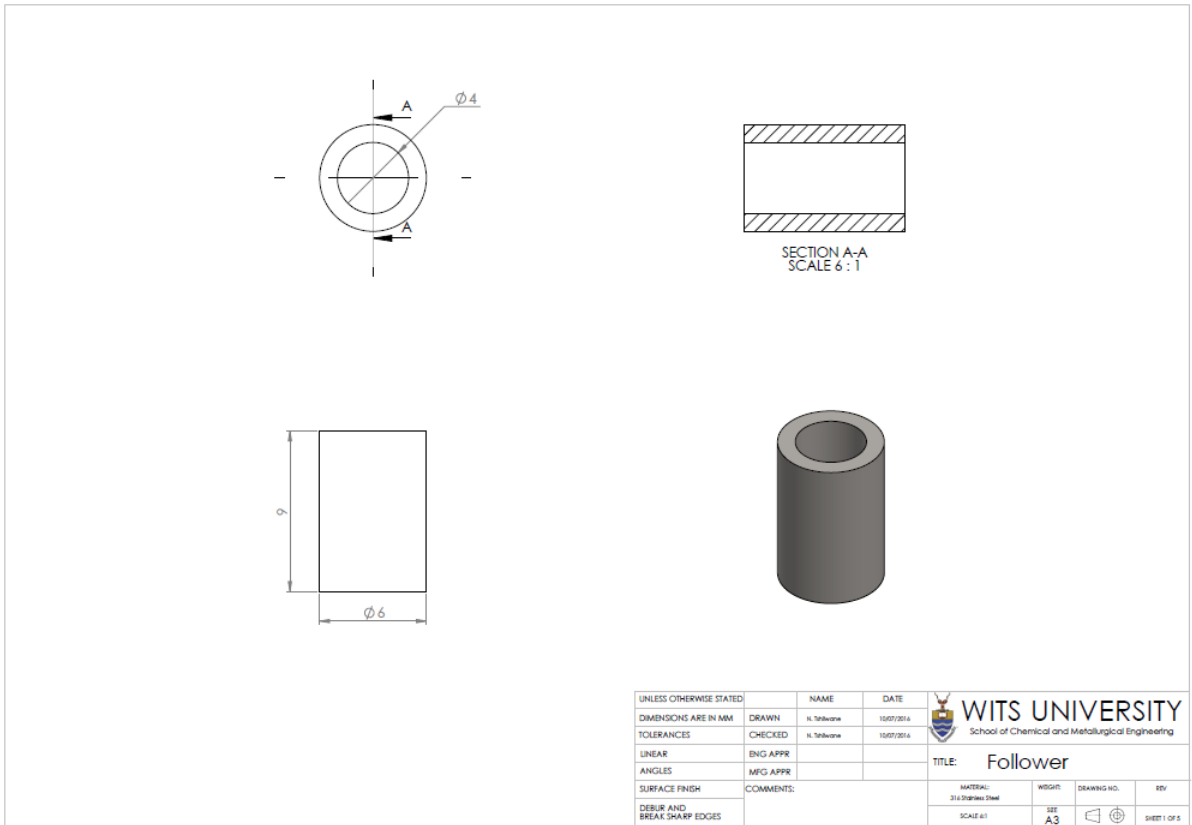Figure D-3: 316 stainless steel cap for adopter body
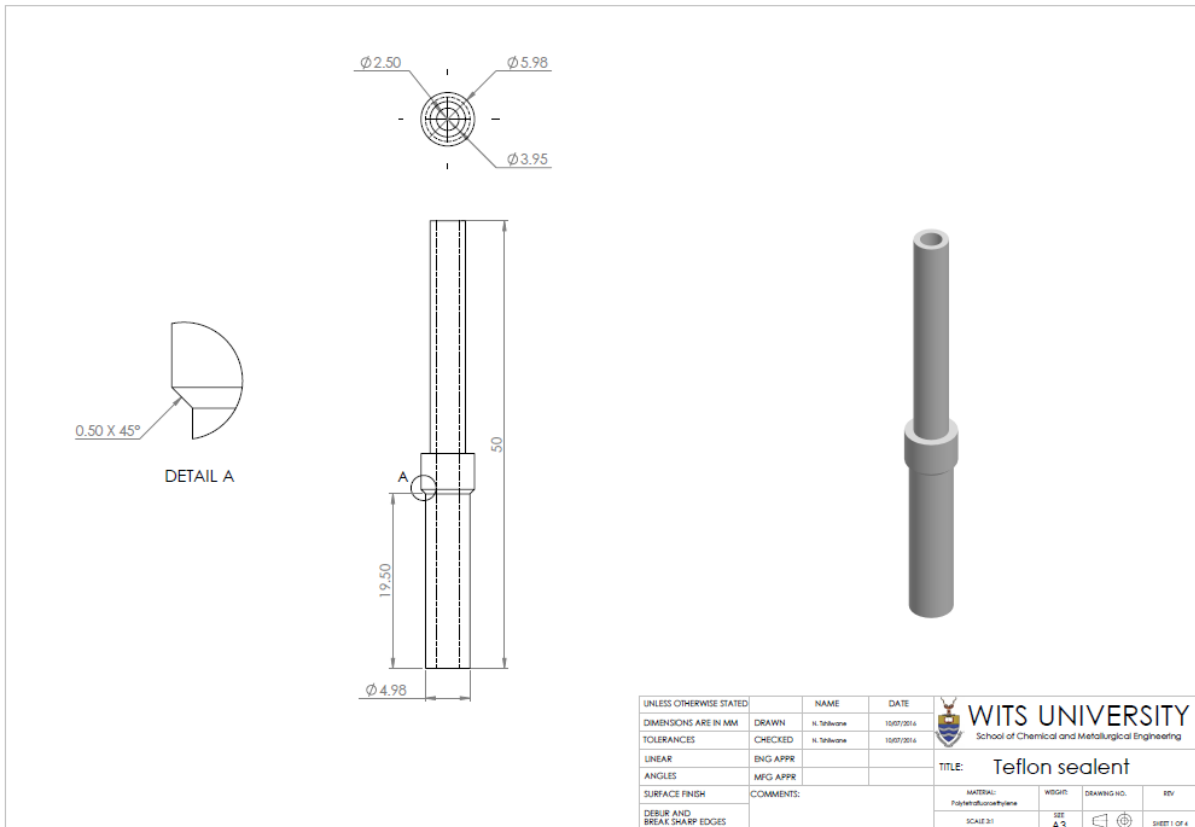
Figure D-4: Teflon follower to fit in the autoclave gland.

Figure D-5: Teflon sealant for autoclave gland.